

POLITECNICO DI TORINO

Corso di Laurea in Ingegneria Energetica e Nucleare

Tesi di Laurea Magistrale

**Neutronic and thermal-hydraulic  
simulations for Molten Salt Fast Reactor  
safety assessment**



**Relatori**

Prof. Sandra Dulla

Prof. Piero Ravetto

Prof. Antonio Cammi

Dott. Stefano Lorenzi

Francesco Di Lecce

Luglio 2018



# Contents

<b>Acknowledgements</b>	V
<b>Abstract</b>	VII
<b>Nomenclature</b>	IX
<b>List of Figures</b>	XIII
<b>List of Tables</b>	XV
<b>1 Introduction</b>	1
1.1 Outline and subject of the thesis . . . . .	1
1.2 Molten Salt Fast Reactors . . . . .	3
1.2.1 Reference MSFR description . . . . .	3
1.2.2 Emergency core Draining System . . . . .	5
1.3 Molten salt properties . . . . .	5
1.4 OpenFoam CFD software . . . . .	8
<b>2 Simplified 0-D semi-analytical model for molten salt fuel draining</b>	11
2.1 Introduction . . . . .	11
2.2 System geometry . . . . .	12
2.3 The mathematical model . . . . .	13
2.3.1 Thermal-hydraulics sub-model . . . . .	14
2.3.2 Neutronics sub-model . . . . .	18
2.3.3 Heat source from fissions and decay heat . . . . .	26
2.3.4 Molten salt level sub-model . . . . .	27
2.3.5 Analytical expression for geometry-related reactivity . . . . .	31
2.3.6 Initial conditions . . . . .	32
2.4 Semi-analytical model simulations . . . . .	33
2.4.1 Simulink environment . . . . .	33
2.4.2 Model scheme . . . . .	34
2.5 Results and plots . . . . .	34
2.5.1 Simulation results . . . . .	35
2.5.2 Local uncertainty analysis . . . . .	38
2.6 Concluding remarks . . . . .	41

<b>3</b>	<b>Preliminary 2-D CFD-based multiphysics model for molten salt fuel draining</b>	<b>43</b>
3.1	Introduction . . . . .	43
3.2	Problem setup and assumptions . . . . .	44
3.2.1	Computational domain and mesh grid . . . . .	45
3.3	OpenFOAM multiphysics modelling . . . . .	47
3.3.1	Fluid-dynamics and energy equations . . . . .	47
3.3.2	Neutronics equations . . . . .	48
3.3.3	Iteration scheme and equation differentiating patterns . . . . .	50
3.4	Initial and boundary conditions . . . . .	51
3.4.1	Boundary conditions . . . . .	51
3.4.2	Initial conditions . . . . .	52
3.5	The adiabatic method . . . . .	54
3.5.1	The iteration procedure . . . . .	54
3.5.2	myPowerMethodFoam2 . . . . .	57
3.6	Results . . . . .	58
3.6.1	Volume and mass balances' verification . . . . .	58
3.6.2	The drainage dynamics . . . . .	59
3.6.3	Fluid pressure and mechanical energy . . . . .	61
3.6.4	System reactivity . . . . .	63
3.6.5	Neutron flux . . . . .	64
3.6.6	Precursors of neutrons and decay heat . . . . .	65
3.6.7	Molten salt temperature . . . . .	67
3.7	Concluding remarks . . . . .	69
<b>4</b>	<b>Heat Transfer Coefficient for internally heated fluids</b>	<b>71</b>
4.1	The need of a new correlation . . . . .	71
4.2	Analytical analysis by Fiorina et al. . . . .	72
4.3	Numerical CFD-based analysis . . . . .	75
4.3.1	The CFD model and domain . . . . .	75
4.4	Comparison between analytical and CFD-based corrective factors . . . . .	77
4.5	CFD-based improved correlation . . . . .	80
4.6	Inward and outward external heat fluxes . . . . .	82
4.7	Application to the draining shaft . . . . .	84
4.8	Concluding remarks . . . . .	85
<b>5</b>	<b>Conclusion</b>	<b>87</b>
	<b>Bibliography</b>	<b>91</b>

## Acknowledgements

*The thesis has been realised in the framework of the inter-university degree programme in Nuclear Engineering, POLY<sup>2</sup>NUC. It consists in a collaboration between Politecnico di Torino (PoliTo) and Politecnico di Milano (PoliMi), which aims at creating synergies between the research activities of the two polytechnic schools. During the master degree, the first year has been spent at PoliTo and two succeeding years at PoliMi, with the last entirely devoted to thesis activity.*





## Abstract

*Molten Salt Fast Reactor (MSFR) is an innovative and challenging reactor concept in the frame of Generation IV International Forum. The unique and distinctive feature of molten salt reactors is the liquid state of their fuels, which leads to important benefits in terms of fully-passive safety, intrinsic stability and fuel sustainability. At the same time, these features call for new safety systems that should be studied, as the Emergency core Draining System. Molten salt fuel draining, along with other MSFR key safety features, is a research activity in the frame of SAMOFAR (Safety Assessment of the Molten Salt Fast Reactor) European project, being part of Horizon 2020 Euratom programme.*

*This thesis objective is to provide an accurate description of core dynamics during a molten salt fuel draining. In case of emergency, the salt could be drained out from the core, actively or passively triggered by melting of salt plugs, and stored into a draining tank underneath the core. During the draining transient, the fuel should evacuate the thermal power due to decay heat to avoid mechanical damages to core internal surfaces and to EDS structure. In addition, the subcriticality of the fuel salt should be granted during all the draining transients. The aim of this thesis is the development of modelling tools for investigating and assessing the temperature and reactivity variation during draining transients in MSFR.*

*A simplified multiphysics analysis of the molten salt fuel draining is firstly proposed, consisting in a zero-dimensional semi-analytical model, able to capture the coupling among salt fluid-dynamics, system energy and neutronics. Temperature and system reactivity time evolutions are described and the general dynamics of the draining phenomenon is figured out. A particular emphasis is given to develop reactivity coefficients related to temperature (to model Doppler broadening effects) and to volume change (the multiplying domain reduces due to salt draining meaning an increase in neutron leakages).*

*From the 0-D model results, it is deduced that the problem is intrinsically related to spatial features of the system, i.e. the location of the draining shaft that affects the outflow salt enthalpy. Therefore a multi-dimensional model is required to fully characterized the salt draining. The second part of the thesis focuses hence on developing a preliminary two-dimensional axial-symmetric CFD-based numerical model. Salt fluid-dynamics are modelled with RANS equations along with realizable  $k-\epsilon$  turbulence model, while energy balance is described with a local temperature partial differential equation. As far as neutronics is concerned, monoenergetic neutron diffusion and precursors' balances are included in the model. Finally, the computational model executable is implemented in the open-source C++ OpenFOAM software.*

*CFD simulation results show that the highest temperature local hot spot never overcomes the critical value to bring damages to internal wall structures and, furthermore, confirm the intrinsically stability of molten salt reactors, since the supercritical phase ends within 1 second from the transient onset and consequently subcritical conditions are established.*

*Ultimately, during the drainage, thermal damages could occur because of fuel salt flowing along the draining shaft. Fluids flowing in channels and featuring an internal production of heat have significantly different heat transfer mechanisms with respect to conventional thermal-hydraulic streams. Therefore the third part of the thesis provides a CFD-based model in order to obtain a correlation for the Heat Transfer Coefficient to predict the real wall-bulk temperature difference and indeed the thermal load on tube surfaces (Fiorina et al., 2013). CFD-based correlation is finally used to study the thermal-hydraulics of the draining shaft in the frame of a fuel draining scenario, demonstrating no worrying thermal loads on shaft walls.*



# Nomenclature

Greek symbols			
$\alpha_T^*$	Temperature reactivity feedback coefficient related to variation of $k_\infty$ (1/K)	$\lambda_{mix}$	Time constant of salt mixing (s)
$\alpha_T^{**}$	Temperature reactivity feedback coefficient due to $M^2$ (1/K)	$\lambda_{p,i}$	Decay constant of i-th neutron precursor group (1/s)
$\alpha_h$	Reactivity coefficient due to geometry change (1/m)	$\nu\Sigma_f$	Fission cross section times neutron yield (1/m)
$\alpha_{\Sigma_a}$	Doppler coefficient for $\Sigma_a$ (1/m)	$\nu$	Kinematic viscosity ( $m^2/s$ )
$\alpha_{\Sigma_f}$	Doppler coefficient for $\Sigma_f$ (1/m)	$\nu_T$	Turbulent kinematic viscosity ( $m^2/s$ )
$\alpha_{D_n}$	Doppler coefficient for $D_n$ (m)	$\Phi_0$	Normalization coefficient for flux ( $1/m^2/s$ )
$\alpha_{E_f\Sigma_f}$	Doppler coefficient for $E_f\Sigma_f$ (J/m)	$\Phi$	Neutron flux ( $1/m^2/s$ )
$\bar{\tau}$	Deviatoric stress two-order tensor (Pa)	$\Pi_1$	Term 1, energy equation (Km/s)
$\beta$	Total effective delayed neutron fraction (1)	$\Pi_2$	Term 2, energy equation (Km/s)
$\beta_i$	Effective delayed neutron fraction of i-th group (1)	$\Pi_3$	Term 3, energy equation (Km/s)
$\delta$	Mass density (kg/m <sup>3</sup> )	$\rho$	System reactivity (1)
$\eta$	Normalized neutron population (1)	$\rho_h$	Reactivity variations due to geometry (1)
$\gamma_{air}$	Air volume fraction (1)	$\rho_T$	Reactivity variations due to temperature (1)
$\gamma_{salt}$	Salt volume fraction (1)	$\sigma$	Corrective factor 2 (1)
$\Lambda$	Effective neutron generation lifetime (s)	$\Sigma_a$	Absorption cross section (1/m)
$\lambda_d$	Total decay constant of decay heat precursors (1/s)	$\theta$	Viscous dissipation parameter (1)
$\lambda_p$	Total decay constant of neutron precursors (1/s)	$\varphi$	Corrective factor 3 (1)
$\lambda_{d,j}$	Decay constant of j-th decay heat precursor group (1/s)	$\xi$	Normalized precursor concentration (1)
		$\zeta$	Corrective factor 1 (1)
		$E_f\Sigma_f$	Energy per fission times $\Sigma_f$ (J/m)

### Latin symbols

$(C)_0$	Normalization coefficient for neutron precursor ( $1/\text{m}^3$ )	$C_p$	Fanning friction factor for the shaft wall (1)
$(q_d)_0$	Normalization coefficient for decay heat ( $\text{J}/\text{m}^3$ )	$c_p$	Specific heat at constant pressure ( $\text{J}/\text{kg}/\text{K}$ )
$\bar{F}_T$	interface surface tension ( $\text{N}/\text{m}^3$ )	$C_t$	Fanning friction factor for the tank wall (1)
$\bar{r}$	Position coordinates (m)	$c_v$	Specific heat at constant volume ( $\text{J}/\text{kg}/\text{K}$ )
$\bar{U}$	Velocity vector (m/s)	$d$	Shaft diameter (m)
$\dot{m}$	Mass flow rate (kg/s)	$D_n$	Diffusion coefficient (m)
$\dot{m}_B$	Outflow mass flow rate (kg/s)	$D_{eff}$	Effective (laminar plus turbulent) diffusion coefficient ( $\text{m}^2/\text{s}$ )
$\dot{m}_{in}$	Inlet mass flow rate (kg/s)	$E$	Dimensional parameter for neutron precursor initial condition ( $1/\text{m}^3$ )
$\dot{m}_{out}$	Outlet mass flow rate (kg/s)	$e$	Specific total energy ( $\text{J}/\text{kg}$ )
$\dot{Q}_f$	Source of thermal power (W)	$E_{sys}$	Total system energy content (J)
$\dot{q}_f$	Volumetric source of thermal power ( $\text{W}/\text{m}^3$ )	$f$	Total fraction of decay heat precursors (1/s)
$\dot{q}_{fis}$	Total fission volumetric power ( $\text{W}/\text{m}^3$ )	$f_j$	Fraction of j-th decay heat precursors (1/s)
$\dot{V}_{in}$	Inlet volumetric flow rate ( $\text{m}^3/\text{s}$ )	$g$	Gravitational acceleration ( $\text{m}/\text{s}^2$ )
$\dot{V}_{out}$	Outlet volumetric flow rate ( $\text{m}^3/\text{s}$ )	$H$	Tank height (m)
$\tilde{C}_i$	Total number of precursors of the i-th group (1)	$h$	Monitor length (m)
$\tilde{C}_{i,out}$	Outflow-transported precursor contribution for i-th group (1/s)	$h_{jw}$	Only heat flux HTC ( $\text{W}/\text{m}^2/\text{K}$ )
$\tilde{k}$	Thermal conductivity ( $\text{W}/\text{m}/\text{K}$ )	$H_{loss}$	Total head loss (m)
$\tilde{k}_{eff}$	Effective (laminar plus turbulent) thermal conductivity ( $\text{W}/\text{m}/\text{K}$ )	$h_Q$	Only internal source HTC ( $\text{W}/\text{m}^2/\text{K}$ )
$\tilde{u}$	Specific internal energy ( $\text{J}/\text{kg}$ )	$h_{ref}$	Reference monitor length (m)
$A$	Dimensional parameter for decay heat initial condition ( $\text{J}/\text{m}^3$ )	$h_{tot}$	Total HTC ( $\text{W}/\text{m}^2/\text{K}$ )
$B^2$	Geometrical buckling of the system ( $\text{m}^{-2}$ )	$i_B$	Outflow enthalpy ( $\text{J}/\text{kg}$ )
$C$	Precursor concentration ( $1/\text{m}^3$ )	$j_w$	Wall heat flux ( $\text{W}/\text{m}^2$ )
$C_0$	Precursor concentration at equilibrium ( $1/\text{m}^3$ )	$K$	Kinetic energy ( $\text{m}^2/\text{s}^2$ )
$C_i$	Precursor concentration of i-th group ( $1/\text{m}^3$ )	$k$	Effective multiplication factor (1)
		$k_\infty$	Infinite multiplication factor (1)
		$K_c$	Tank-pipe contraction local friction factor (1)

$L$	Cylinder length (m)	$r$	Cylindrical coordinate 1 (m)
$l$	Neutron lifetime (s)	$Re$	Reynolds number (1)
$m$	Mass (kg)	$Sc$	Schmidt number (1)
$M^2$	Migration area (m <sup>2</sup> )	$Sc_T$	Turbulent Schmidt number (1)
$N$	Total number of neutrons (1)	$T$	Temperature (K)
$n$	Neutron concentration (1/m <sup>3</sup> )	$t$	Time (s)
$n_0$	Neutron concentration at equilibrium (1/m <sup>3</sup> )	$t^*$	Draining time (s)
$Nu_{j_w}$	Only heat flux Nusselt number (1)	$T_b$	Bulk temperature (K)
$Nu_Q$	Only internal source Nusselt number (1)	$T_w$	Wall temperature (K)
$Nu_{tot}$	Total Nusselt number (1)	$T_{ref}$	Reference temperature (K)
$p$	Fluid pressure (Pa)	$U$	Velocity magnitude (m/s)
$P_{decay}$	Decay heat (W/m <sup>3</sup> )	$u$	Velocity x-component (m/s)
$P_{prompt}$	Instantaneous deposition of power (W/m <sup>3</sup> )	$U^*$	Nominal core average velocity (m/s)
$Pr$	Prandtl number (1)	$U_r$	Velocity r-component (m/s)
$Pr_T$	Turbulent Prandtl number (1)	$U_z$	Velocity r-component (m/s)
$Q$	Volumetric heat source (W/m <sup>3</sup> )	$v$	Neutron speed (m/s)
$Q_T$	Temperature source rate (K/s)	$v_A$	Salt free surface velocity (m/s)
$q_d$	decay energy stored in precursors (J/m <sup>3</sup> )	$v_B$	Outflow velocity (m/s)
$R$	Cylinder radius (m)	$V_{fs}$	Fuel salt volume inventory (m <sup>3</sup> )
		$z$	Cylindrical coordinate 2 (m)



# List of Figures

1.1	Thesis outline. . . . .	3
1.2	Scheme of the reference MSFR (Merle et al., 2015). . . . .	4
1.3	Section of the MSFR and the Emergency Draining System (Merle et al., 2015). . . . .	5
2.1	Tank geometry configuration for 0-D model. . . . .	13
2.2	Graphic scheme depicting the multiphysics of the molten salt fuel draining. . . . .	14
2.3	Time-varying control volume. . . . .	15
2.4	Difference between mean and outflow molten salt temperatures. . . . .	18
2.5	Neutron and precursor balances. . . . .	19
2.6	Reactivity coefficient $\alpha_h(h, T)$ as a function of the monitor length $h$ for a fixed temperature of 900 K. . . . .	23
2.7	Temperature feedback coefficients as functions of temperature. . . . .	25
2.8	Integral variation of reactivity due to geometry change $\rho_h(h, T)$ as a function of the monitor length $h$ for a fixed temperature of 900 K. . . . .	26
2.9	Morrison’s correlation for Fanning friction factor as a function of Reynolds number for smooth pipes. . . . .	29
2.10	Molten salt level evolution in time. It goes from the the initial value $H=2.255$ m (full tank) to zero (empty tank). . . . .	31
2.11	System reactivity as function of time due to geometry change (molten salt draining) for a fixed value of temperature. . . . .	32
2.12	Simulink scheme of the fuel salt draining model. . . . .	35
2.13	System reactivity as function of time. . . . .	36
2.14	Simulation results of the 0-D semi-analytical model with input parameters of table 2.2. . . . .	37
2.15	Terms of the RHS of energy equation as function of time. . . . .	38
2.16	Comparison between the two boundary conditions considered for the energy equation. . . . .	39
2.17	Transients of temperature and other variables of interest, where the nominal problem solution (red line) is compared with variation of parameters of $\pm 10$ % (dash-dot lines). . . . .	40
2.18	Refer to figure 2.17 for the caption. . . . .	41
3.1	Model geometry, computational domain and a detail on the mesh grid . . . . .	46
3.2	Iteration scheme adopted to solve the coupled equations for the fluid-dynamics and the neutronics. . . . .	50
3.3	Boundaries of the CFD domain. . . . .	51
3.4	Coordinates $r$ and $z$ which define the reference system for initial conditions of neutron flux and precursors. . . . .	53
3.5	Adiabatic method iteration scheme. . . . .	56
3.6	Joint between <i>myPowerMethodFoam2</i> and <i>myCompInterFoam11</i> solver applications. . . . .	57
3.7	Volume and mass balance verifications. . . . .	59

3.8	Molten salt level time evolution. In blue the CFD-computed salt level, while red and green lines represent 0-D model outcomes with respectively $\theta=0.710$ and $\theta=0.785$ .	60
3.9	Salt volume fraction distributions in the domain. . . . .	61
3.10	Pressure and mechanical energy axial profiles at $t=30$ s. . . . .	62
3.11	System reactivity time evolution. . . . .	63
3.12	Neutron flux axial and radial profiles. . . . .	65
3.13	Neutron flux spatial distributions for some time snapshots. . . . .	66
3.14	Neutron flux time evolution for the early 0.14 s. Blue and red lines are respectively the results of the CFD simulation and the 0-D semi-analytic model. . . . .	66
3.15	Average precursor concentrations of decay heat and neutrons are respectively depicted in left and right figures. . . . .	67
3.16	Decay heat and neutron precursor distributions. . . . .	68
3.17	Temperature spatial distributions for $t$ equal to 0, 20 and 40 s. . . . .	68
3.18	Mean temperature of molten salt versus time. Blue and red lines are respectively the CFD and the 0-D model results. . . . .	69
4.1	The goal: computing the HTC for a fluid subjected to both external heat flux and internal heat generation flowing in circular ducts. . . . .	72
4.2	Superposition of effects. . . . .	73
4.3	Boundaries and mesh grid. . . . .	76
4.4	Comparison with Dittus-Boelter's and Gnielinski's correlations. . . . .	78
4.5	Temperature radial profiles for the situations of only heat flux and of both heat flux and internal generation. . . . .	79
4.6	Comparison between Fiorina's and CFD-based results. . . . .	80
4.7	Corrective factor $\varphi$ as function of $Re$ and $Pr$ . . . . .	81
4.8	Dependencies of the corrective factor $\zeta$ , equation (4.6), on the Reynolds number, on Prandtl number and on the adimensional ratio $QD/j_w$ . . . . .	82
4.9	Radial temperature profiles for an outward heat flux plus internal heat generation at the outlet section. . . . .	83
4.10	Increment of the wall-bulk temperature difference, $(T_w - T_b)_Q$ . . . . .	85

# List of Tables

1.1	Reference Molten Salt Fast Reactor parameters (Handbook of GIV reactors). . . . .	4
1.2	LiF-ThF <sub>4</sub> fuel salt reference thermo-physical properties. . . . .	6
1.3	Neutron cross section parameters. . . . .	7
1.4	Delayed neutron precursors constants and fractions. . . . .	7
1.5	Decay heat precursor constants and fractions. . . . .	8
2.1	Model domain dimensions (Wang et al., 2016). . . . .	13
2.2	List of initial conditions. . . . .	33
2.3	Time scales of the different physical phenomena involved in the fuel salt draining. . . . .	34
2.4	Maximum relative variation of the temperature transient for a parameter shift of $\pm 10\%$ from its nominal value. . . . .	42
3.1	Air thermo-physical properties. They refer to air at 700 °C and 1bar. . . . .	45
3.2	Boundary conditions for the CFD simulations. . . . .	52
3.3	Comparison of total head losses due to friction and local dissipations between CFD simulation result and 0-D model with two values of parameter $\theta$ . . . . .	60
4.1	Thermo-physical properties of the Lithium-Thorium Fluoride binary salt. . . . .	76
4.2	Boundary conditions imposed. . . . .	77
4.3	Thermal conditions setup. Two situations are studied, represented by two couples of external heat flux $j_w$ and internal heat generation $Q$ . . . . .	78
4.4	CFD-based corrective factors ( $\varphi_{CFD}$ ) for the laminar flow regime. . . . .	80
4.5	Setup quantities for simulations referring to figures 4.9. . . . .	84



# Chapter 1

## Introduction

Molten Salt Fast Reactor (MSFR) is the reference liquid-fuelled reactor concept in the frame of Generation IV International Forum (GIV) [1].

The feasibility of circulating molten salt as both coolant and nuclear fuel was tested for the first time at Oak Ridge National Laboratory (ORNL) during the '50s and '60s [2]. The research efforts end up with the construction of the Molten Salt Reactor Experiment pilot plant, which consisted in a thermal-spectrum reactor operating for 4 years until 1969. The second concept of molten salt reactor, the Molten Salt Breeder Reactor, was never completed due to different difficulties and weaknesses.

The interest in molten salt fuels declined after the experiments at ORNL, but it grew up again from 2005 on in many countries [3], in particular in Italy at Politecnico di Torino [4] and later at Politecnico di Milano [5].

Two main fast spectrum liquid-fuelled reactor concepts are under investigation nowadays: the European Molten Salt Fast Reactor and the Russian MOLten Salt Actinide Recycler and Transmuter (MOSART). In this thesis, the first one is considered as reference, which is also studied in the frame of the EVOL (Evaluation and Viability of Liquid fuel) Euratom project and SAMOFAR (Safety Assessment of the Molten Salt Fast Reactor) European H2020 project [6, 7].

### 1.1 Outline and subject of the thesis

SAMOFAR main objective is to demonstrate the feasibility of the MSFR through experimental and computational researches and techniques. The main characterizing feature of molten salt reactors is that the circulating liquid acts both as nuclear fuel and coolant. This implies new benefits, technological strategies and physical phenomena characterizing MSFR concept with respect to traditional solid-fuelled reactors and that have to be analysed and investigated.

Among the key safety features faced in the frame of SAMOFAR, the thesis focuses on the core dynamics analysis and safety assessment during the molten salt fuel draining.

Liquid fuels entail new technological strategies concerning fully-passive safety. In case of accident, the fuel can be drained out, driven by gravitational force, from the core and stored in a draining tank placed underneath it, where proper subcritical and cooling conditions are ensured. The salt drainage involves a multiphysics problem: fuel level drops while it continues to produce thermal power (fission events and decay heat), resulting in a temperature growth. Therefore, the main concern is to assess the possibility of damages to structural materials due to power production and consequently temperature increase.

Furthermore, the initial state of the core, in the worst-case scenario, could be, from the neutronics view point, supercritical as in classic RIA-based accidents. Hence the fuel salt represents a multiplying domain that changes volume in time and its system reactivity is thus a function of both temperature (due to strong temperature feedback) and geometry (due to increase of neutron leakages).

In this thesis, a simplified zero-dimensional (0-D) semi-analytical model is firstly developed and proposed. The multiphysics coupling among fluid-dynamics, energy balance and neutronics is captured in order to analyse and comprehend the general dynamics of the phenomenon and, thanks to its flexibility and low computational resource utilization, to assess draining problem features. Particular emphasis is given on developing analytical expressions to model the reactivity coefficients related to temperature feedback and to multiplying volume variation.

Consequently, from 0-D result analysis, it is deduced that the draining phenomenon is intrinsically related to spatial features of variables. The reader could, for example, consider the position of the draining shaft in the core lower surface: it determines the outflow salt enthalpy and indeed the system energy content during the transient. It is required, hence, a multi-dimensional model to fully characterized the core dynamics of molten salt fuel draining.

Therefore, a preliminary two-dimensional (2-D) axial-symmetric computational fluid-dynamics (CFD) model is developed. Fluid-dynamics of molten salt is modelled with Reynolds-Avareged Navier-Stokes (RANS) equations, where turbulence effects are captured with realizable k- $\epsilon$  model, along with the temperature transport equation. Neutronics are described with monoenergetic diffusion equation for neutrons and transport equation for precursors. The adiabatic method is adopted to monitor the system reactivity within the multiplying domain.

The model and associated executable are constructed and implemented on the open-source C++ OpenFOAM software [8].

Ultimately, the EDS analysis leads to investigate the heat transfer mechanisms that are established within the draining shaft. During the transient, in fact, the fuel salt flows within the bottom shaft and it is featured by an internal generation of heat. The dynamics of internally heated fluids presents different heat transfer behavior with respect to conventional fluid problems. As a matter of fact, wall-bulk temperature difference could significantly change if the fluid features an internal power source and have to be studied in order to suitably design tube thicknesses and materials and avoid thermal damages. This problem is a concern in the frame of MSFR safety assessment regarding not only the draining shaft, but also any out-of-core component (pipes, heat-exchanger tubes and so on).

Thus in the last part of the thesis, the heat transfer mechanisms of internally heated fluids flowing in circular ducts are analysed and a correlation for the Heat Transfer Coefficient (HTC) for such thermal-hydraulic problems is developed. Actually, the activity devised in the frame of the thesis represents a CFD-based benchmark of an analytical study developed at Politecnico di Milano by Fiorina et al. [9].

The thesis outline is sketched in figure 1.1.

Concluding, the thesis is organized as follows. The first chapter deals with the 0-D approach to the molten salt draining problem, while in the second chapter the multiphysics CFD simulation is developed and assessed. Last chapter is devoted to the development of an improved CFD-based correlation for the HTC of internally heated liquids flowing in circular ducts.

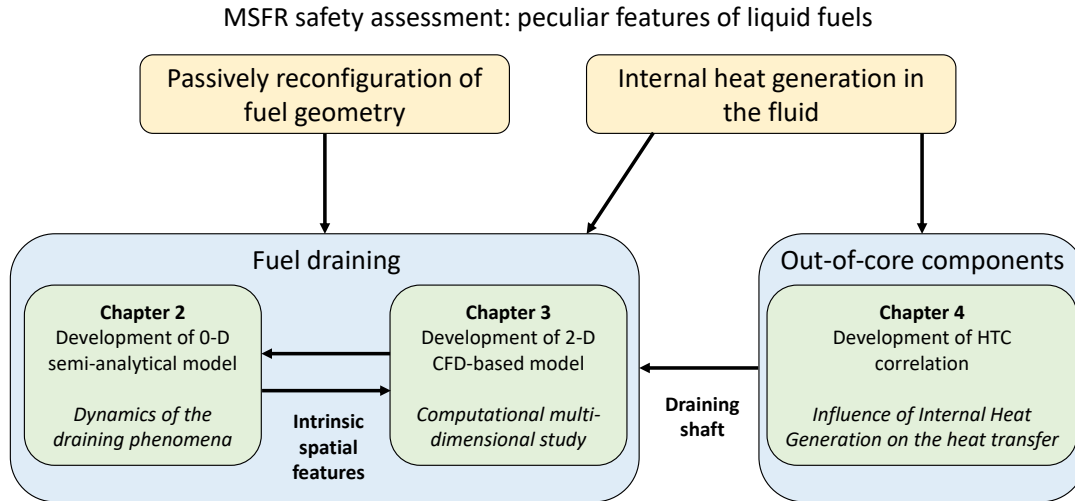


Figure 1.1: Thesis outline.

## 1.2 Molten Salt Fast Reactors

The Molten Salt Fast Reactor (MSFR) is one among the six conceptual reactors selected in the frame of GIV International Forum. Generation IV reactors must satisfy some design constraints regarding fuel sustainability, nonproliferation, safety and waste management. These constraints would be accomplished through closed and completely integrated fuel cycle, developing a breeder system to produce on-site new fissile material, strongly negative temperature feedback coefficient, fully-passive safety systems and actinide handling system.

The main feature of molten salt reactors is the liquid state of the fuel. This innovative feature brings important benefits to liquid-fueled reactor concepts. Firstly, liquid fuels allow for a composition versatility both in terms of fissile-fertile percentage in the liquid mixture and in terms of heavy nuclei used. In other words, the same reactor could be fed during its life by both the Uranium and Thorium chains and further there is the possibility to burn transuranic elements. Concerning fuel cycle front end, liquid fuels do not need any fabrication and production processes typical of solid fuels, thus eliminating the associated costs.

From neutronics point of view, molten salt reactors present an homogeneous core and a strong temperature feedback due to Doppler broadening effects.

Another characteristic is the absence of a separated coolant. The fuels itself is the coolant. This feature brings unique consequences with respect solid-fueled reactors. There is no longer a time delayed heat transfer between heat production within the fuel and heat extraction at the heat-exchangers. The fuel temperature is indeed directly affected by heat extraction perturbations. This lays new reactor control mechanisms: just controlling the heat extraction, the fuel temperature can be adjusted and, thanks to strong reactivity feedback, the system thermal power is indeed controlled.

### 1.2.1 Reference MSFR description

The reference MSFR is a 3 GWth conceptual liquid-fueled reactor. A scheme of the reference MSFR is represented in figure 1.2. In its nominal operating conditions, the fuel enters from the

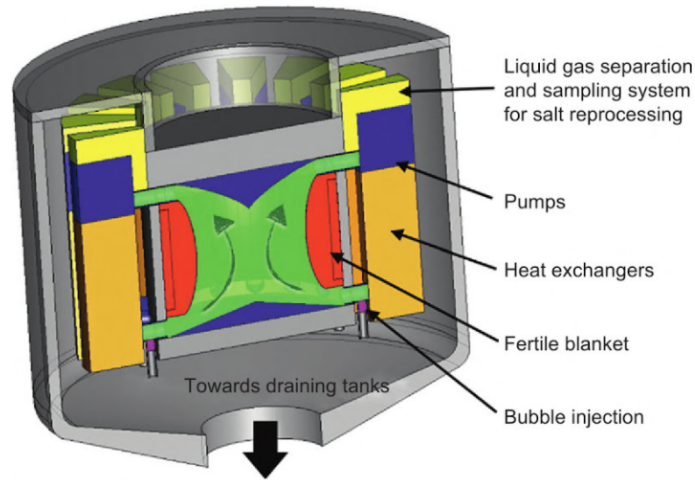


Figure 1.2: Scheme of the reference MSFR (Merle et al., 2015).

Table 1.1: Reference Molten Salt Fast Reactor parameters (Handbook of GIV reactors).

Thermal power	3 GW
Fuel molten salt composition	LiF (77.5 mol%)-ThF <sub>4</sub>
Fuel salt melting point	565 °C
Mean fuel salt temperature	700 °C
Inlet fuel temperature	650 °C
Outlet fuel temperature	750 °C
Mean core radius	1.1275 m
Mean core height	2.255 m
Total fuel salt volume	18 m <sup>3</sup>
Volume flow rate	4.5 m <sup>3</sup> /s

bottom at a temperature of 650 °C and flows upwards reaching its maximum temperature of 750 °C. The mean fuel temperature within the core is about 700 °C. The fuel circuit is closed with one of the sixteen external loops, consisting in a heat-exchanger and a pump. This cycle lasts about 4 s to complete.

Fluid-dynamics studies confer to the core a torus shape to follow properly the velocity streamlines and avoid dangerous hot spots and recirculation within the fuel. The total fuel inventory amounts to about 18 m<sup>3</sup>, contained half in the core and half into pipes and heat exchangers. An expansion tank is located to accommodate salt density variations. The core is radially surrounded by a breeding blanket, for the transmutation of fertile material and the upper and lower ends are bounded by Hastelloy-N neutron reflectors. A bubbling system is foreseen in order to remove fission products and other metals without stopping the reactor operations.

Table 1.1 groups the nominal parameters of the reference MSFR [1].

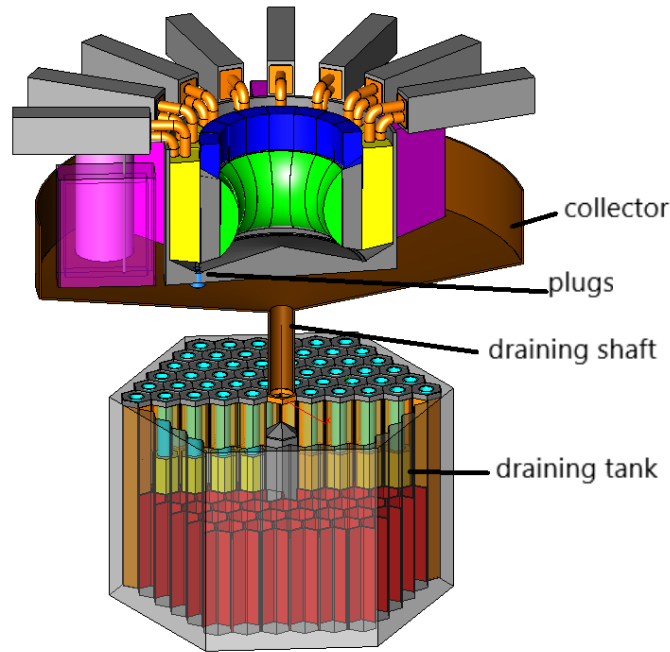


Figure 1.3: Section of the MSFR and the Emergency Draining System (Merle et al., 2015).

### 1.2.2 Emergency core Draining System

Molten salt reactor classes allow for new fully-passive safety systems, i.e. not triggered or fed by any electrical or mechanical devices or operators. They are completely driven by gravitational force. This is the case of the Emergency core Draining System (EDS), depicted in figure 1.3. During an accidental situation in the core due to an unknown insertion of reactivity in the system, the power grows up immediately and so does the fuel temperature. If it reaches an established critical set point, a salt plug (there could be more than one plug) located at the core bottom melts and the liquid fuel starts being drained through a draining shaft into a tank underneath the core, where subcritical conditions are ensured. A phase-change material cools down the drained fuel and in the meanwhile keeps it in a liquid state.

The EDS could be triggered actively by operator or passively by salt plugs that melt when the temperature reaches a critical value. The critical temperature set point is far below the boiling point of the fuel salt, which is about 1755 °C [10].

The main concern of the EDS is that the core reactor internal surfaces, probably made of Nickel-based alloy, could be endangered by salt temperature rise during the draining due to continuous power production. The temperature threshold, over which Ni-based alloys could be endangered, is in the 1250 °C-1350 °C range [11].

## 1.3 Molten salt properties

In this study it is considered as liquid fuel the molten binary fluoride salt with 78 mol% of LiF and the remaining 22 mol% of ThF<sub>4</sub>, that is the reference molten salt in the Handbook of GIV nuclear reactors [1]. However, in a generic binary fluoride salt, that 22 mol% could be replaced by any mixture of heavy nuclei fluorides, whilst respecting the condition of fast neutron spectrum

Table 1.2: LiF-ThF<sub>4</sub> fuel salt reference thermo-physical properties.

		Expression (T in K)	Value at 700 °C	Validity range (°C)
Mass density (kg/m <sup>3</sup> )	$\delta$	4094 - 0.882 (T-1008)	4125	617-847
Kinematic viscosity (m <sup>2</sup> /s)	$\nu$	$5.54 \times 10^{-8} \exp(3689/T)$	$2.46 \times 10^{-6}$	625-847
Thermal conductivity (W/m/K)	$\tilde{k}$	$0.928 + 8.397 \times 10^{-5} T$	1.0097	625-847
Specific heat (J/kg/K)	$c_p$	-1111+2.78 T	1594	595-634

throughout the reactor operations. Versatility in fuel composition is in fact one of the improvements led by molten salt reactors.

The melting point of LiF-ThF<sub>4</sub> is 565 °C; indeed the fuel salt must be maintained at a temperature larger than its melting point (plus eventually a safety margin) in every reactor situations, even in the stand-by conditions.

Fluoride molten salts have thermo-physical properties highly dependent on temperature, in particular their viscosity. Simulations upon the MSFR European concept use the properties listed in table 1.2. It is a common practice for computational activities in the current literature to use, as first approximation, temperature-independent salt properties and to assume constant values computed at 700 °C. In this way, computational efforts due to high temperature-related non-linearity could be reduced in numerical simulations of salt reactors.

As far as nuclear properties are concerned, neutron cross sections are in principle strongly dependent on temperature. The temperature dependence is due to both the Doppler broadening effect and the salt thermal expansion (salt density or void effects). Both contributions to the total temperature feedback are largely negative (temperature feedback coefficient of about -5 pcm/°C) and are extremely important for the molten salt reactor functioning and safety.

Regarding the Doppler effect modelling, nuclear cross sections are expressed by logarithmic functional forms of the temperature, as stated in the book by Waltar [12]. The cross section formulae are as follows:

$$\begin{aligned}
 \Sigma_a(T) &= (\Sigma_a)_0 + \alpha_{\Sigma_a} \ln \left( \frac{T}{T_{ref}} \right), \\
 \nu \Sigma_f(T) &= (\nu \Sigma_f)_0 + \alpha_{\nu \Sigma_f} \ln \left( \frac{T}{T_{ref}} \right), \\
 D_n(T) &= (D_n)_0 + \alpha_{D_n} \ln \left( \frac{T}{T_{ref}} \right), \\
 E_f \Sigma_f(T) &= (E_f \Sigma_f)_0 + \alpha_{E_f \Sigma_f} \ln \left( \frac{T}{T_{ref}} \right),
 \end{aligned} \tag{1.1}$$

where, respectively from the top, there are listed the absorption cross section (1/m), the fission cross section times the average number of neutrons produced per fission (1/m), the neutron diffusion coefficient (m), the energy production per fission event times the fission cross section (J/m). The constant parameters appearing in the above equations are taken from the PhD dissertation by Aufiero and are reported in table 1.3 [13].

Monoenergetic neutron approximation is adopted in this study. In the neutron transport equation, and also in the diffusion equation, the inverse neutron speed appears, which multiplies the time derivative of the neutron flux. An inverse neutron speed of  $6.55767 \times 10^{-7}$  s/m is adopted, which corresponds to a neutron energy of 23.2 keV. The cross section quantities listed in table 1.3 refer to the aforementioned neutron energy.

Table 1.3: Neutron cross section parameters.

Inverse velocity (s/m)	$1/v$	$6.55767 \times 10^{-7}$
Reference temperature (K)	$T_{ref}$	900
Reference diffusion coefficient (m)	$(D_n)_0$	$1.172 \times 10^{-2}$
Doppler coefficient for $D_n$ (1/m)	$\alpha_{D_n}$	$-5.979 \times 10^{-5}$
Reference absorption cross section (1/m)	$(\Sigma_a)_0$	$6.893 \times 10^{-1}$
Doppler coefficient for $\Sigma_a$ (1/m)	$\alpha_{\Sigma_a}$	$7.842 \times 10^{-3}$
Reference fission cross section times neutron yield (1/m)	$(\nu\Sigma_f)_0$	$7.430 \times 10^{-1}$
Doppler coefficient for $\Sigma_f$ (1/m)	$\alpha_{\Sigma_f}$	$-1.700 \times 10^{-2}$
Energy per fission times $\Sigma_f$ (J/m)	$(E_f\Sigma_f)_0$	$9.573 \times 10^{-12}$
Doppler coefficient for $E_f\Sigma_f$ (J/m)	$\alpha_{E_f\Sigma_f}$	$-2.060 \times 10^{-13}$

Table 1.4: Delayed neutron precursors constants and fractions.

Group	Decay constant (s <sup>-1</sup> )	Fraction
1	0.0125	$2.28 \times 10^{-4}$
2	0.0283	$5.00 \times 10^{-4}$
3	0.0425	$4.16 \times 10^{-4}$
4	0.1330	$6.67 \times 10^{-4}$
5	0.2920	$1.06 \times 10^{-3}$
6	0.6660	$1.85 \times 10^{-4}$
7	1.630	$2.34 \times 10^{-4}$
8	3.550	$5.30 \times 10^{-4}$
total	0.0611	0.0033

An other important phenomenon involved in neutronics is represented by the production of fission products which emit, through their decays, delayed neutrons. Delayed neutron production is modelled by eight neutron precursor groups. The decay constants and fractions are reported in table 1.4 [14]. The equivalent one group approximation of neutron precursors are characterized by a decay constant  $\lambda_p$  of 0.0611 s and a total fraction  $\beta$  of 0.0033, computed as follows:

$$\beta = \sum_i^8 \beta_i, \tag{1.2}$$

$$\lambda_p = \left( \frac{1}{\beta} \sum_i^8 \frac{\beta_i}{\lambda_{p,i}} \right)^{-1},$$

where the  $\beta_i$  and the  $\lambda_{p,i}$  are the fractions and decay constants of the i-th neutron precursor group. As far as the decay heat is concerned, it is modelled with three families of decay heat precursors. The decay constants and fractions are shown in table 1.5 [14]. Also for the decay heat it is assumed a single group of precursors computed as

$$f = \sum_j^3 f_j, \tag{1.3}$$

$$\lambda_d = \frac{1}{f} \sum_j^3 \lambda_{d,j} f_j,$$

Table 1.5: Decay heat precursor constants and fractions.

Group	Decay constant (s <sup>-1</sup> )	Fraction
1	0.2160	0.0128
2	0.0182	0.0123
3	0.0259	0.0208
total	0.0768	0.0459

where  $f_j$  and  $\lambda_{d,j}$  are respectively the fraction and the decay constant of the  $j$ -th decay heat precursor family.

The last nuclear parameter that will be used in this thesis is the mean generation life time  $\Lambda$ , which is the average time from a prompt neutron emission by fissions to a neutron emission of the succeeding generation. It is set being  $0.95 \mu\text{s}$ .

## 1.4 OpenFoam CFD software

OpenFOAM (Open-source Field Operation And Manipulation) is an open source computational fluid dynamic (CFD) software [8, 15]. It is a C++ environment that is able to solve scalar and vector differential equations using the finite volume method and based on interpolation and derivative schemes set up by the users.

OpenFoam is not only open, in the sense that is totally free. The most attractive feature is instead its open in terms of source code, utilities, solvers and libraries. It allows users to construct own executables to solve coupled problems and to include new governing equations not yet implemented within OpenFOAM environment. Such executables that are run to solve CFD coupled problems are called *applications*. For *solvers* is intended instead each designed to solve a specific problem in computational quantum mechanics [8].

C++ syntax gives an intuitive language to write down the partial differential equations being solved. As an example, consider the temperature equation solved in a pre-compiled application on OpenFOAM:

$$\frac{\partial T}{\partial t} + \nabla \cdot (\bar{U}T) - \nabla \cdot (\alpha \nabla T) = 0 \quad (1.4)$$

where  $T$  is the temperature,  $\bar{U}$  the velocity vector and  $\alpha$  is the thermal diffusivity (m<sup>2</sup>/s). The above PDE is translated into OpenFOAM environment as:

```
fvScalarMatrixTEqn
(
  fvm::ddt(T)
  +fvm::div(phi,T)
  -fvm::laplacian(alpha,T)
);
TEqn.solve();
```

where phi is the mass flow through the call faces  $\delta \bar{U} \cdot \bar{A}$ , with  $\bar{A}$  the oriented area of the face

and  $\delta$  the mass density.

It is relevant to understand how the pressure is coded within the OpenFOAM solver applications. The total pressure of a flowing fluid is composed by two contributions: the static pressure and the dynamic pressure. The latter one is the term  $1/2\delta U^2$ , while the static pressure could be split into the potential term  $\delta gh$  ( $h$  is the elevation from a reference point) and the hydrostatic term. Within OpenFOAM it is coded the static pressure with the symbol `p` and the hydrostatic term `p_rgh`.



## Chapter 2

# Simplified 0-D semi-analytical model for molten salt fuel draining

*Liquid-fueled reactors allow, among several benefits in terms of fuel handling, heat transfer and neutronics homogeneity, new concepts of fully passive safety systems. Liquids, in fact, lead to rapid and passive fuel geometry reconfiguration driven by gravitational forces, such as the Emergency core Draining System (EDS). The research and development of MSFRs, in the frame of SAMOFAR European project, move also in direction to study and investigate the dynamics of the fuel salt when it is drained in case of accidental situations.*

*A simplified zero-dimensional semi-analytical model is developed here to capture the multiphysics phenomena involved and, in particular, to focus on time evolutions of temperature and system reactivity. The 0-D model is built to analyse and comprehend the general dynamics of the fuel draining and predict if some troubles could occur concerning internal surface thermal damages.*

*The main concern of the model is to couple the fuel salt thermal-hydraulics with the neutronics physics, thus taking into account the power generation produced during the transient.*

*A particular emphasis is placed on computing reactivity feedback coefficients, both temperature and geometry related. The salt, in fact, may be seen as a volume-change multiplying domain and this impacts significantly on the neutron economy.*

### 2.1 Introduction

The main innovative feature of molten salt reactors consists in liquid fuels. The immediate benefits that liquid fuels entail are the stronger negative reactivity temperature feedback, the versatility in terms of composition and the absence of dedicated fluid as coolant. Moreover the liquid fuel offers the opportunity of a new fully passive safety systems driven by the gravitational force: the Emergency Draining System (see section 1.2.2).

Imagine that, due to accidental conditions, it is decided to drain the fuel out into a tank underneath the core, where subcritical conditions are ensured and a proper cooling system is acting. Starting from the core, accidental conditions may rise during the reactor operation. In particular, due to unintentional injection of fissile material, nuclear fuel may undergo supercriticality, which represents the onset conditions of the draining transients. Thus the free surface starts to drop while the power production within the salt will continue to increase. The geometry of the multiplying domain changes: this has a strong impact on the neutron leakages and hence on the system reactivity. This latter one strongly depends also on the temperature due to high temperature reactivity

feedback coefficient of molten salt fuels. Subsequently the reactivity drops and strong subcritical conditions take place in the molten salt multiplying domain.

To conclude, in this work it is wanted to investigate and study in which way and how much the system reactivity is affected by temperature feedback and the variation of the multiplying domain geometry and how its variation has implications on the temperature evolution. Furthermore temperature peak is a concern of internal wall surface safety assessment: during the whole draining, the temperature must not exceed a critical value to bring damages to core materials.

The thesis positions itself in the frame of the European project SAMOFAR (Safety Assessment of the Molten Salt Fast Reactor), that is one of the major Research and Innovation projects in the Horizon 2020 Euratom research programme [7].

The EDS has been object of different conceptual and design studies in past years. It is mentioned here the analysis by Wang et al. developed at KIT in collaboration with the Université Grenoble Alpes [10]. It includes a preliminary evaluation of some orders of magnitude of draining time periods, based on a simplified analytical model and a simplified geometry. The analytical model is able to capture the hydraulic phenomenon of the drainage, predicting the draining time for different geometrical situations. Anyway the thermal problem is not considered and the role of the molten salt as a nuclear fuel completely neglected.

Conversely, the work presented in this chapter intends being on one hand the pursuit of the work by Wang et al., studying deeply the draining transient of a molten salt fuel not only hydraulically, but giving more details to the phenomenon regarding mainly the temperature and the reactivity evolutions and their coupling. Thus the molten salt is not considered as only a passively drained liquid, but as a nuclear multiplying medium, which reactivity strongly depends on temperature and geometry.

In this chapter, a simplified semi-analytic zero-dimensional (0-D) mathematical model is proposed. Such integral lumped approach is able to capture and comprehend the general dynamics of variable transients and the main features of the phenomenon. The temperature time evolution, the system reactivity transient and how it is affected by both temperature and geometry are the main objectives of the model.

## 2.2 System geometry

A simplified geometry is considered in this work and takes up the work by Wang et al. [10]. It is a cylinder, representing the core, with a hole in the center of the bottom surface and followed by a long pipe, to simulate the draining shaft. The reader could refer to figure 2.1.

The reference MSFR conceptual design [1], studied in the frame of EVOL Euratom and SAMOFAR projects, is adopted to impose the dimensions of the simplified geometry domain. The height  $H$  is chosen to be 2.255 m (table 1.1), while concerning the diameter ( $2R$ ), to maintain the fuel salt volume inventory ( $V_{fs}$ ), it is adjusted as follows:

$$V_{fs} = R^2 \pi H \Rightarrow 2R = \sqrt{\frac{4V_{fs}}{\pi H}}. \quad (2.1)$$

In fact, regarding draining phenomena, the most important dimension is the height, so the diameter is just computed to keep the salt volume inventory. The diameter obtained is 3.188 m.

As regards the draining shaft, its dimensions are taken from [10] and corresponds to 0.2 m and 2.0 m respectively for the diameter  $d$  and the axial length  $L$ .

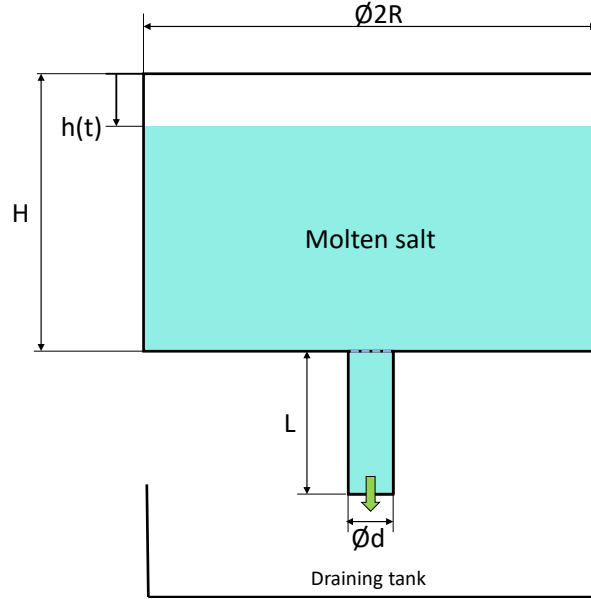


Figure 2.1: Tank geometry configuration. It consists in a cylinder with a long cylindrical pipe at the bottom. The molten salt evolution is detected with the quantity  $h(t)$ , that is the distance of the salt free surface from the tank upper surface.

Table 2.1: Model domain dimensions (Wang et al., 2016).

Tank height	$H$	2.255 m
Tank diameter	$2R$	3.188 m
Shaft length	$L$	2.0 m
Shaft diameter	$d$	0.2 m

The domain dimensions are resumed in table 2.1, while its graphical representation is shown in figure 2.1. The molten salt initially fills completely the tank and, during the draining transient, starts emptying it, exiting through the draining shaft and the bottom outlet section. The molten salt level is monitored by the quantity  $h(t)$ . It is defined as the distance of the salt free surface from the tank upper boundary. It is initially null (full tank) and reaches the value  $H$  when the tank is completely empty.

## 2.3 The mathematical model

The core tank emptying is modelled with a 0-D semi-analytical mathematical model. The lumped integral approach to the draining phenomenon allows to capture and comprehend the general dynamics of variable transients and, thanks to its flexibility and low computational resources, to deduce relevant model features.

The molten salt fuel is a multiphysics transient problem. Observe figure 2.2. The energy balance,

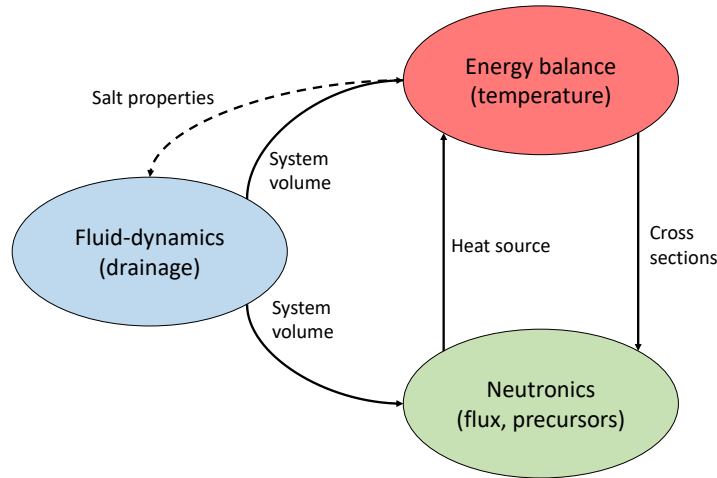


Figure 2.2: Graphic scheme depicting the multiphysics of the molten salt fuel draining. If temperature-dependent salt properties are considered, then also the coupling between fluid-dynamics and energy balance will be modelled.

which determines the temperature time evolution, needs as input the source of heat from fissions and precursor decays, which is the outcome of neutronics. In turn equations for neutrons and precursors require as the temperature in order to model the temperature dependency of cross sections and, indeed, the Doppler broadening effect. Moreover, the multiplying domain, which coincides with the molten salt, changes in time as the liquid is drained out. Thence the system volume is specified by the salt fluid-dynamics. Salt thermo-physical properties are in principle functions of temperature, which implies a coupling between fluid-dynamics and energy balance. However this coupling is neglected since salt properties are kept temperature independent (table 1.2).

Therefore both temperature and geometry affect the system reactivity negatively, which has hence a feedback on the heat production, and in turn on the temperature again.

The model tries to capture the multiphysics described, highlighting the temperature and the system reactivity evolutions in time.

According to the graphical scheme of figure 2.2, the presented model is split into three sub-models, which represent the physical phenomena that it is wanted to describe and couple:

- the thermal-hydraulics sub-model;
- the neutronics sub-model;
- the molten salt level evolution sub-model.

The single sub-models are described in details in the following subsections, presenting the assumptions made and the mathematical strategies adopted.

### 2.3.1 Thermal-hydraulics sub-model

The molten salt is drained in time, leaving an empty space that is occupied by air or some other inert gaseous substance. Two mathematical approaches could be adopted. The problem could be studied considering a fixed control volume, coincident with the whole tank, where air enters from

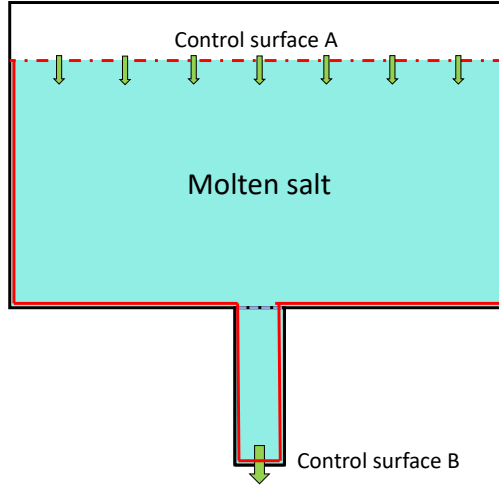


Figure 2.3: A time-varying control volume is adopted to describe the draining phenomenon. No mass nor energy streams can enter or exit in the system, except for control surface B, through which molten salt is drained.

the top, to fill the space left empty by the drained molten salt, and the salt that is exiting from the bottom outlet. Indeed all the boundaries are fixed.

A second approach, which is that one adopted in this work, foresees a time-varying control volume, which coincides with the salt in the tank. The control volume so-defined presents the bottom outlet boundary, lateral fixed borders and the moving upper boundary, which follows the salt free surface. Figure 2.3 shows a scheme of the time-varying control volume approach: Control Surface (CS) A is moving, no mass nor energy streams are entering/exiting from the system; CS B is the outlet section, where a molten salt flux goes out from the domain. Other boundaries are fixed and impermeable to any mass or energy streams.

### Mass balance

The mass variation within the control volume is due only to the quantity of molten salt that is exiting from control surface B. Moreover, for moving CVs, the absolute velocity of streams is replaced by the relative velocity, which is the velocity of the fluid seen by a reference system placed upon the moving boundary [16]. Since the CS A moves with the salt free surface, its relative velocity is null: no mass stream enters in the domain. Thus the mass equation can be written as follows:

$$\left(\frac{dm(t)}{dt}\right)_{CV} = -\dot{m}_B(t), \quad (2.2)$$

where  $m(t)$  is the mass content of molten salt in the Control Volume (CV) at time  $t$  and  $\dot{m}_B(t)$  is the mass flow rate through the CS B. This latter one can be expressed, knowing the CS B area, as

$$\dot{m}_B(t) = \delta \frac{d^2}{4} \pi v_B(t), \quad (2.3)$$

where  $v_B(t)$  is the mean velocity of molten salt at CS B and  $\delta$  is the salt mass density. Whereas the mass content  $m(t)$  is rewritten in terms of mass density and fuel salt volume as follows:

$$m(t) = \delta R^2 \pi (H - h(t)) + \delta \frac{d^2}{4} \pi L. \quad (2.4)$$

Plugging equations (2.3) and (2.4) into (2.2) yields, after some mathematical steps,

$$\frac{dh(t)}{dt} = \left( \frac{d}{2R} \right)^2 v_B(t), \quad (2.5)$$

where  $h(t)$  is the aforementioned monitor length. Therefore the mass balance reduces to equation (2.5), that relates the salt free surface velocity  $v_A(t) = dh/dt$  to the outlet velocity  $v_B(t)$ . The tricky point is how to model  $v_B$  and it will be described later on.

### Energy balance

The variation of energy contained in the CV depends on the energy flux going out through CS B and on the energy source  $\dot{Q}_f(t)$ , linked to neutronics (prompt fission deposition of heat and decay heat). The energy equation thus is

$$\left( \frac{dE_{sys}(t)}{dt} \right)_{CV} = -\dot{m}_B(t) \left( i_B(t) + \frac{v_B^2(t)}{2} + gz_B \right) + \dot{Q}_f(t). \quad (2.6)$$

In the LHS of energy equation, the variation of energy content ( $E_{sys}(t)$ , measured in J) in time is equal to the integral over the whole CV of the energy per unit mass  $e(\bar{r}, t)$  (J/kg), that depends on time  $t$  and position  $\bar{r}$ :

$$\left( \frac{dE_{sys}(t)}{dt} \right)_{CV} = \frac{d}{dt} \int_{CV} \delta e(\bar{r}, t) dV. \quad (2.7)$$

$e(\bar{r}, t)$  is composed by three contributions: the kinetic  $v^2(\bar{r}, t)/2$ , the potential  $gz(\bar{r}, t)$  and the internal energy  $u(\bar{r}, t)$ . The first two can be neglected with respect to the internal energy term, obtaining

$$\frac{d}{dt} \int_{CV} \delta e(\bar{r}, t) dV = \frac{d}{dt} \int_{CV} \delta \left( \frac{v^2(\bar{r}, t)}{2} + gz(\bar{r}, t) + u(\bar{r}, t) \right) dV \simeq \delta \frac{d}{dt} \int_{CV} \tilde{u}(\bar{r}, t) dV. \quad (2.8)$$

The internal energy per unit mass  $u(\bar{r}, t)$  can be approximated for liquids with the product of the temperature  $T(\bar{r}, t)$  times the isobaric specific heat:

$$\delta \frac{d}{dt} \int_{CV} \tilde{u}(\bar{r}, t) dV \simeq \delta c_p \frac{d}{dt} \int_{CV} T(\bar{r}, t) dV. \quad (2.9)$$

A 0-D model assumes a single value of temperature to describe the whole system, that is the average over the CV. For sake of simplicity, such average temperature is called  $T(t)$ . Therefore the variation of energy within the system becomes

$$\begin{aligned} \delta c_p \frac{d}{dt} \int_{CV} T(\bar{r}, t) dV &\simeq \delta c_p \frac{d}{dt} (T(t) V_{CV}(t)) = \delta c_p \frac{d}{dt} \left( T(t) \left( R^2 \pi (H - h(t)) + \frac{d^2}{4} \pi L \right) \right) = \\ &= \delta c_p \left( \left( R^2 \pi (H - h(t)) + \frac{d^2}{4} \pi L \right) \frac{dT(t)}{dt} - T(t) R^2 \pi \frac{dh(t)}{dt} \right). \end{aligned} \quad (2.10)$$

The energy content in the system varies in time due to twofold phenomena: the variation of internal energy, i.e. temperature, and the decreasing of the volume, represented by the quantity  $h(t)$ .

In the RHS of equation (4.15), the first term is related to exiting energy flux from CS B. In brackets there is the energy per unit mass of a flowing fluid, that is composed by the enthalpy  $i_B$ , that is equal to  $c_p$  times the outlet temperature  $T_B(t)$ , the kinetic term  $v_B^2(t)/2$  and the potential term  $gz_B(t)$ . The latter term is imposed being the reference height and set to zero, while equation (2.5) is used to derive a relation of  $v_B^2(t)/2$  and  $\dot{m}_B(t)$  as functions of  $h(t)$ .

Therefore, placing in the LHS and RHS of the energy equation (4.15) respectively equation (2.10) and comments discussed above, it is rearranged as follows:

$$\begin{aligned} \delta c_p \left( \left( R^2 \pi (H - h(t)) + \frac{d^2}{4} \pi L \right) \frac{dT(t)}{dt} - T(t) R^2 \pi \frac{dh(t)}{dt} \right) &= \\ &= -\delta R^2 \pi \frac{dh(t)}{dt} \left( c_p T_B(t) + \frac{1}{2} \left( \frac{2R}{d} \right)^4 \left( \frac{dh(t)}{dt} \right)^2 \right) + \dot{Q}_f(t). \end{aligned} \quad (2.11)$$

After some algebraic steps, the final energy equation for the analysed system is obtained:

$$\left( H - h(t) + \left( \frac{d}{2R} \right)^2 L \right) \frac{dT(t)}{dt} = (T(t) - T_B(t)) \frac{dh(t)}{dt} - \frac{1}{2c_p} \left( \frac{2R}{d} \right)^4 \left( \frac{dh(t)}{dt} \right)^3 + \frac{\dot{Q}_f(t)}{\delta c_p R^2 \pi}. \quad (2.12)$$

If the temperature was spatially homogeneous in the system, then the salt outflow would not cause any variation in the average temperature. This means to set  $T(t)$  equal to the outflow temperature  $T_B(t)$ . It is clear that the first term in the RHS of equation (2.12) disappears.

Anyway, the temperature within the system is not uniform and this feature has to be taken into account in the present 0-D model. The non-uniformity information of the temperature is given to the 0-D model by the difference  $T(t) - T_B(t)$ .

The spatial feature of the draining problem cannot be ignored. For example, think about the position of the draining shaft. The location on the bottom surface affects the molten salt extracted from the tank and indeed its temperature. Therefore  $T_B$  could change according to the position of the bottom pipe. The 0-D model cannot see these kind of spatial information and it has to be given as input.

The most immediate guess is to consider  $T(t)$  as the mean temperature between  $T_B(t)$  and  $T_A(t)$ . Substitute then  $T(t) - T_B(t)$  with  $T_A(t) - T(t)$  and assume a constant  $T_A$  during the transient (imagine that the interface gas-salt brings to injecting gas temperature all along the transient):

$$\left( H - h(t) + \left( \frac{d}{2R} \right)^2 L \right) \frac{dT(t)}{dt} = (T_A - T(t)) \frac{dh(t)}{dt} - \frac{1}{2c_p} \left( \frac{2R}{d} \right)^4 \left( \frac{dh(t)}{dt} \right)^3 + \frac{\dot{Q}_f(t)}{\delta c_p R^2 \pi}. \quad (2.13)$$

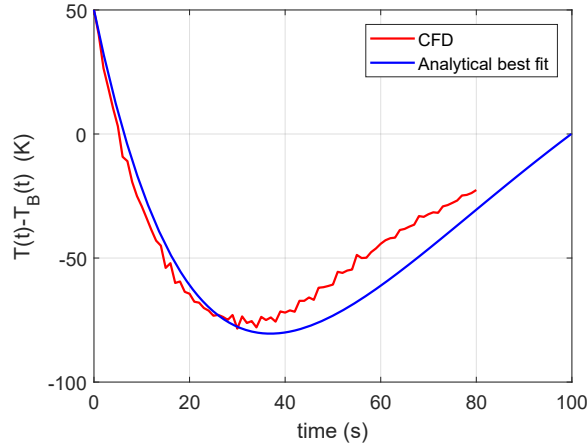


Figure 2.4: Difference between mean and outflow molten salt temperatures. In red the results computed through CFD-based numerical study of the draining transient (described in details in chapter 3), while in blue the analytical best fitting expression.

A more accurate information about non-uniformity could be taken from CFD-based simulations of the problem (that is illustrated in details in the next chapter). From the CFD analysis, the temperature difference is computed and shown in figure 2.4. A best fit analysis is then employed to derive an analytical expression to model the  $T(t) - T_B(t)$  term in time:

$$T(t) - T_B(t) = \Delta T_0 \left( 2 - \left( 1 - \frac{t}{t^*} \right) e^{-\lambda_{mix} t} - 2 \frac{t}{t^*} e^{\lambda_{mix} (t^* - t)} \right) \quad (2.14)$$

where  $\Delta T_0$  is the initial value of the temperature difference, which corresponds to 50 K (table 1.1),  $t^*$  is the draining time (it will be discussed later on in details) and  $\lambda_{mix}$  is a time constant related somehow to temperature spatial heterogeneity and to the salt mixing.

### 2.3.2 Neutronics sub-model

#### Point kinetic equations

The molten salt system neutron kinetics is approximated by the point kinetics equations. Point kinetics ensures integral conservation of neutrons and precursors, that is the relevant feature for the present 0-D lumped model. Spatial distributions of variables are not a concern for the moment. Point kinetics assumes the neutron flux to be dependent on time and space separately, i.e. the spatial shape of the flux is not affected by time. This condition is more valid for fast reactors, which are more tightly coupled neutronicly than thermal reactors, and for homogeneous reactors [17]. MSFRs and the draining neutronic problem allow adopting the point kinetics equations as an approximation of the system kinetics.

The outward stream of fuel adds a new feature to neutronics. For this reason the equations for precursors are derived from the initial balances, as explained in the book of D. L. Hetrick [18].

In the figure 2.5 the reader can see the neutron and precursor balances in the system, inspired by the aforementioned book. Neutrons are lost due to leakages through the boundaries and due to absorptions. A certain percentage of absorptions produce fission events, which end in an instantaneous emission of new neutrons and fission products. Some of the latter ones are neutron

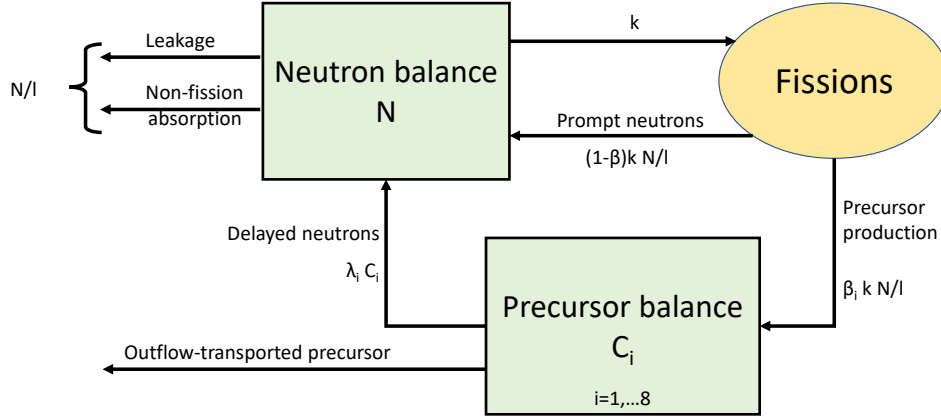


Figure 2.5: Neutron and precursor balances. The scheme is inspired by the book of D. L. Hetrick (1971). The main difference is the new way of escaping possibility, that is the outward mass flow through the control surface B that transports the precursors.

precursors, in the sense that they emit later on further neutrons through  $\beta$ -decay chain events. the outward mass flow of molten salt causes a new escaping possibility for precursors. Such outflow stream of precursors is called outflow-transported precursors. Neutrons instead do not see macroscopic fluid flows since the time and the length scales are much lower. Nevertheless the neutron dynamic is affected by the geometry change of the multiplying domain. So to recap: the molten salt is emptying the tank and this fact has effects, from the point of view of neutronics, on neutrons, since the multiplying domain changes increasing the leakages, and on precursors, since they are escaping from the CV.

The outflow-transported precursor contribution  $\tilde{C}_{i,out}(t)$  (i-th precursors per second) is linked to the mass flow rate  $\dot{m}_B(t)$  as follow:

$$\tilde{C}_{i,out}(t) = \dot{m}_B(t) \frac{1}{\delta} C_i(t) \quad (2.15)$$

where  $C_i(t)$  is the precursor concentration in the system (i-th precursors per  $\text{m}^3$ ) and  $\dot{m}_B/\delta$  is the volume flow rate through CS B ( $\text{m}^3/\text{s}$ ). Actually, also the the outflow-transported precursor term is extremely affected by geometry and spatial features, as the outflow salt temperature  $T_B(t)$ . Nevertheless it is considered of secondary importance and indeed related to mean concentration of precursors.  $\tilde{C}_{i,out}(t)$  is thus the number of precursors per unit time that leave the system. Plugging the relation for  $\dot{m}_B(t)$  as a function of  $dh/dt$ ,  $\tilde{C}_{i,out}(t)$  expression yields

$$\tilde{C}_{i,out}(t) = R^2 \pi \frac{dh(t)}{dt} C_i(t). \quad (2.16)$$

The precursor balance can be written as in [18], but the new contribution just described has to be included:

$$\frac{d\tilde{C}_i(t)}{dt} = \beta_i k \frac{N(t)}{l} - \lambda_{p,i} \tilde{C}_i(t) - \tilde{C}_{i,out}(t), \quad (2.17)$$

where  $N(t)$  and  $\tilde{C}_i(t)$  are respectively the total number of neutrons,  $k$  is the effective multiplication factor and the total number of precursors of the  $i$ -th family in the system and the other nuclear parameters are explained in section 1.3. In terms of neutron  $n(t)$  and precursor  $C_i(t)$  densities and using the equation (2.16), the equation just above becomes

$$\frac{d}{dt} (C_i(t) R^2 \pi (H - h(t))) = \beta_i \frac{k}{l} n(t) R^2 \pi (H - h(t)) - \lambda_{p,i} C_i(t) R^2 \pi (H - h(t)) - R^2 \pi \frac{dh(t)}{dt} C_i(t). \quad (2.18)$$

Adopting the definition of the effective neutron generation time  $\Lambda = l/k$ , after some mathematical steps, the precursor balance yields

$$\frac{dC_i(t)}{dt} = \frac{\beta_i}{\Lambda} n(t) - \lambda_{p,i} C_i(t), \quad (2.19)$$

that is again the traditional point kinetic equation for precursors. The outflow contribution to neutron escaping, the term  $\tilde{C}_{i,out}(t)$ , is balanced by the system volume change and in particular by the time-derivative term that comes out developing  $d\tilde{C}_i/dt$ . Physically it means that the outflow molten salt does not affect the concentration of precursors in the system because the number of precursors that goes out from CS B is perfectly balanced by the volume reduction due to the draining. Anyway this is true if the outflow concentration and the mean concentration of precursors are equal (i.e. the precursors concentration is spatially uniform in the domain), that surely would not happen in a real case or in multi-dimensional models.

Although the neutron point kinetic equation is

$$\frac{dn(t)}{dt} = \frac{\rho(t) - \beta}{\Lambda} n(t) + \sum_i^8 \lambda_{p,i} C_i(t). \quad (2.20)$$

As stated before, neutrons do not see any macroscopic fluid motion.

The model developed in this chapter uses a 0-D approach, thus no diffusive nor streaming terms are considered for precursors.

Moreover a single group of neutron precursors is adopted, using the total decay constant and fraction reported in the table 1.4.

Furthermore, in the present work, the point kinetic equations are normalized with respect to the equilibrium values  $n_0$  and  $C_0$ , related as follows

$$\frac{n_0}{C_0} = \frac{\lambda_p \Lambda}{\beta}. \quad (2.21)$$

Defining the normalized neutron population  $\eta(t) = n(t)/n_0$  and the normalized precursor concentration  $\xi(t) = C(t)/C_0$ , equations (2.20) and (2.19) becomes respectively:

$$\begin{cases} \frac{d\eta(t)}{dt} = \frac{\rho(t) - \beta}{\Lambda} \eta(t) + \frac{\beta}{\Lambda} \xi(t) \\ \frac{d\xi(t)}{dt} = \lambda_p (\eta(t) - \xi(t)) \end{cases} \quad (2.22)$$

### System reactivity

Reactivity is the key parameter concerning the system neutron kinetics. It is the expression of the state of a multiplying domain concerning fission chains trend. It is strongly affected by temperature and geometry and in turn it impacts the temperature again through heat production related to fissions and decay heat. With reference to the present study, the molten salt fuel may start from a supercritical condition, i.e. a reactivity larger than zero, in which neutron population grows up with the time scale of the neutron life time and more or less fast according to the amount of reactivity possessed by the system. The molten salt then reaches the criticality, characterized by a balance between the production and the disappearance of neutrons and consequently goes towards the subcritical conditions, i.e. negative reactivity values.

The reactivity is defined as the relative infinitesimal variation of the effective multiplication factor  $k$ . Making explicit that  $k$  is the product of the infinite multiplication factor  $k_\infty$  times the probability of non-leakage, it yields:

$$\delta\rho = \frac{\delta k}{k^2} \simeq \frac{\delta k}{k} = \frac{\delta k_\infty(T)}{k_\infty(T)} - \frac{M^2(T)B^2(h)}{1 + M^2(T)B^2(h)} \left( \frac{\delta B^2(h)}{B^2(h)} + \frac{\delta M^2(T)}{M^2(T)} \right) \quad (2.23)$$

where  $M^2(T)$  is the migration area ( $\text{m}^2$ ) and  $B^2(h)$  the geometrical buckling of the system ( $\text{m}^{-2}$ ). The migration length is defined as one-sixth of the square of the average distance (in all dimension) between the neutron birth point (as a fast neutron) and its absorption and for fast reactors it could be approximated by the diffusion length to the absorption cross section ratio [12]. Observing equation (2.23), the reactivity variation  $\delta\rho$  is due to two contributions: the variation of infinite multiplication factor, that is strictly related to temperature variation of cross sections; non-leakage probability variation, that is linked to geometrical change (the larger the domain the less the probability for neutrons to escape) and to migration length of neutrons, that is again linked to temperature.

Three terms can be individuated in equation (2.23):

- the first one, related to temperature-dependent variation of the infinite multiplication factor;
- the second related to the geometry variation and influencing the system buckling;
- the third and last one, referred to neutron migration in the domain that is affected by temperature.

Analyse now deeply into details the three terms listed above.

#### A. VARIATION OF INFINITE MULTIPLICATION FACTOR

It is already mentioned that the variation of  $k_\infty$  is produced by the temperature dependence of cross sections, which is expressed by the logarithmic formulae reported in equations (1.1). The expressions of cross sections as functions of temperature intend to model the Doppler broadening effects, that is strong for fast and homogeneous reactors.

The first contribution in equation (2.23), plugging the relations (1.1), can be written as

$$\frac{\delta k_\infty}{k_\infty} = \frac{1}{k_\infty} \frac{dk_\infty}{dT} \delta T = \frac{\Sigma_a(T)}{\nu\Sigma_f(T)} \frac{d}{dT} \left( \frac{\nu\Sigma_f(T)}{\Sigma_a(T)} \right) \delta T = \frac{1}{T} \left( \frac{\alpha_{\nu\Sigma_f}}{\nu\Sigma_f(T)} - \frac{\alpha_{\Sigma_a}}{\Sigma_a(T)} \right) \delta T = \alpha_T^*(T) \delta T \quad (2.24)$$

where  $\alpha_T^*(T)$  is defined as the temperature reactivity feedback coefficient related to variation of  $k_\infty$ :

$$\alpha_T^*(T) = \frac{1}{T} \left( \frac{\alpha_{\nu\Sigma_f}}{\nu\Sigma_f(T)} - \frac{\alpha_{\Sigma_a}}{\Sigma_a(T)} \right). \quad (2.25)$$

See figure 2.7a. An increase of temperature causes a reduction of fission cross section  $\nu\Sigma_f(T)$ , while an increase in the absorptions ( $\Sigma_a(T)$  rises up). Overall the infinite multiplication factor decreases. The respective temperature coefficient  $\alpha_T^*(T)$ , which is defined as the relative variation of  $k_\infty$  with respect to temperature, is thus negative. Furthermore the  $1/T$ -dependence of temperature coefficient can be observed, as stated in [12].

## B. VARIATION OF BUCKLING

The geometrical buckling for the cylindrical multiplying domain is the superposition of the buckling of an infinite slab and that one of infinite cylinder as follows:

$$B^2(h) = \left( \frac{j_{0,1}}{R} \right)^2 + \left( \frac{\pi}{H-h} \right)^2, \quad (2.26)$$

where  $j_{0,1}$  is the first zero of the Bessel function of first kind and zero order [19]. It is clear that the extrapolated dimensions, which the buckling refers to, are approximated to the real dimensions of the cylindrical tank. Furthermore note that the geometry variation is expressed by the monitor length  $h(t)$ , that appears in the buckling relation.

Rearranging the second term in equation (2.23), including equation (2.26) and developing the derivative with respect to  $h$ , it is obtained the following result:

$$\begin{aligned} -\frac{M^2(T)B^2(h)}{1+M^2(T)B^2(h)} \frac{\delta B^2(h)}{B^2(h)} &= -\frac{M^2(T)B^2(h)}{1+M^2(T)B^2(h)} \frac{1}{B^2(h)} \frac{dB^2(h)}{dh} \delta h = \\ &= -\frac{M^2(T)}{1+M^2(T)B^2(h)} \frac{2\pi^2}{(H-h)^3} \delta h = \alpha_h(h, T) \delta h \end{aligned} \quad (2.27)$$

where  $\alpha_h(h, T)$  is defined as the reactivity coefficient due to geometry change:

$$\alpha_h(h, T) = -\frac{M^2(T)}{1+M^2(T)B^2(h)} \frac{2\pi^2}{(H-h)^3}. \quad (2.28)$$

It is the expression of the system reactivity variation due to variation of leakages related to a volume change. Neutrons escape with a higher probability from a small volume than larger domains. Therefore, during the molten salt draining, the reduction of the volume implies the increase of the probability of leakage and hence the insertion of negative reactivity in the system. The infinitesimal amount of reactivity inserted is equal to the geometry reactivity coefficient  $\alpha_h(h, T)$  times the infinitesimal variation of cylindrical height.

Figure 2.6 shows the geometry reactivity coefficient as a function of the monitor length for a fixed value of temperature of 900 K. Variations of temperature implies irrelevant variations of  $\alpha_h(h, T)$  for same values of  $h$  due to poor migration area temperature dependency.

## C. VARIATION OF MIGRATION AREA

The last term in equation (2.23) regards the change of probability of non-leakage due to variation of the migration area  $M^2$ . The larger is the migration capability for neutrons to

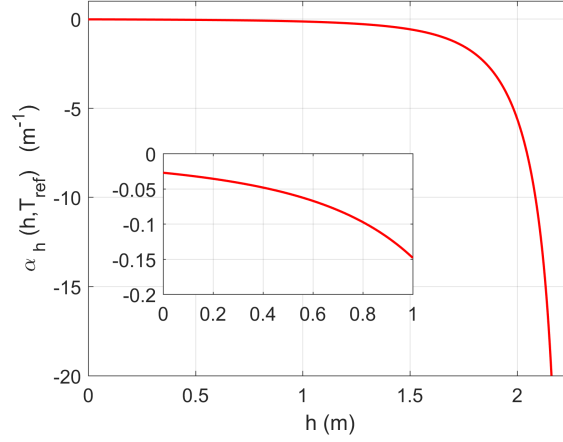


Figure 2.6: Reactivity coefficient  $\alpha_h(h, T)$  as a function of the monitor length  $h$  for a fixed temperature of 900 K.

travel in the medium, the larger is the probability to reach the boundaries and escape. The migration area could change since both temperature and geometry change in the system. Being  $M^2(T) = D_n(T)/\Sigma_a(T)$ , introducing the temperature relations (1.1) and computing the derivative with respect to temperature, it yields:

$$\begin{aligned} -\frac{M^2(T)B^2(h)}{1 + M^2(T)B^2(h)} \frac{\delta M^2(T)}{M^2(T)} &= -\frac{B^2(h)}{1 + M^2(T)B^2(h)} \frac{dM^2(T)}{dT} \delta T = \\ &= -\frac{M^2(T)B^2(h)}{1 + M^2(T)B^2(h)} \frac{1}{T} \left( \frac{\alpha_D}{D_n(T)} - \frac{\alpha_{\Sigma_a}}{\Sigma_a(T)} \right) \delta T = \alpha_T^{**}(h, T) \delta T, \end{aligned} \quad (2.29)$$

where  $\alpha_T^{**}(h, T)$  is the temperature reactivity feedback coefficient due to migration area variation:

$$\alpha_T^{**}(h, T) = -\frac{M^2(T)B^2(h)}{1 + M^2(T)B^2(h)} \frac{1}{T} \left( \frac{\alpha_D}{D_n(T)} - \frac{\alpha_{\Sigma_a}}{\Sigma_a(T)} \right). \quad (2.30)$$

Temperature increase implies on one hand the increase of absorptions of neutrons in the medium, but on the other the reduction of neutron diffusion coefficient. This causes the decrease of the migration area and indeed the decrease of leakage probability. Finally this results in a positive temperature reactivity coefficient due to migration area variations (figure 2.7b). Moreover, also the geometry plays a role in  $\alpha_T^{**}(h, T)$ : the larger the domain (low values of  $h$ ), the smaller the leakage probability and indeed the lower the coefficient  $\alpha_T^{**}(h, T)$ .

It can be defined a total temperature feedback coefficient as the sum of the temperature coefficients aforementioned:

$$\begin{aligned}\alpha_T(h, T) &= \alpha_T^*(T) + \alpha_T^{**}(h, T) = \\ &= \frac{1}{T} \left( \frac{\alpha_{\nu\Sigma_f}}{\nu\Sigma_f(T)} - \frac{1}{1 + M^2(T)B^2(h)} \frac{\alpha_{\Sigma_a}}{\Sigma_a(T)} - \frac{M^2(T)B^2(h)}{1 + M^2(T)B^2(h)} \frac{\alpha_D}{D_n(T)} \right).\end{aligned}\quad (2.31)$$

It is interesting to note the physical meaning of the terms which contribute to the temperature feedback coefficient  $\alpha_T(h, T)$ . In particular the absorption cross section has two opposite impact on the reactivity: the Doppler effect causes the increase in the absorptions and indeed a negative effect on reactivity if the reader thinks to the infinite multiplication factor; conversely, the absorption increase causes a reduction of the leakage rate (think of the migration area  $M^2$ ) and indeed a positive effect on the neutron economics.

Observing figure 2.7d, you can note that the contribution of migration area variations to the total temperature reactivity coefficient is smaller than which one due to  $k_\infty$  variation. In fact the orders of magnitudes of  $\alpha_T^*(T)$  and  $\alpha_T^{**}(h, T)$  are respectively  $10^{-1}$  and  $10^0$  pcm per Kelvin.

Anyway the total differential variation of reactivity is as follows

$$\delta\rho = \alpha_T(h, T) \delta T + \alpha_h(h, T) \delta h.\quad (2.32)$$

It is clear how temperature and geometry differential variations, weighted on the respective reactivity coefficients, influence the differential reactivity variation. To obtain the integral variation of reactivity, both sides of equation just above have to be integrated as follows

$$\rho(h, T) = \int_{T_{ref}}^T \alpha_T(h, T') \delta T' + \int_{h_{ref}}^h \alpha_T(h', T) \delta h' = \rho_T(h, T) + \rho_h(h, T),\quad (2.33)$$

where the reference conditions for temperature and tank height are respectively  $T_{ref}$  and  $h_{ref}$  and it is assumed that the reference reactivity  $\rho(h_{ref}, T_{ref})$  is null, i.e. criticality exists for those temperature and monitor length.  $\rho_T(h, T)$  and  $\rho_h(h, T)$  are respectively the integral reactivity variations due to temperature and geometry.

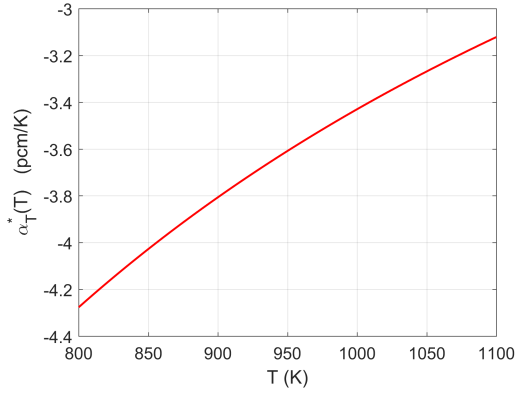
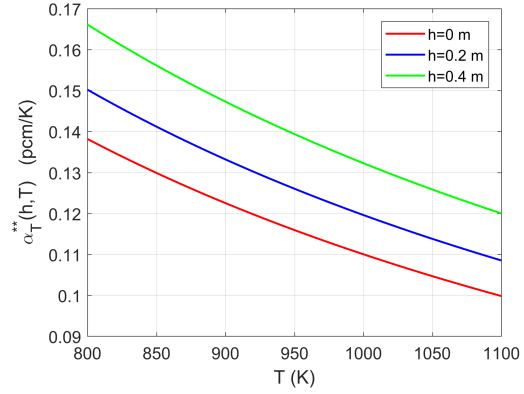
Plugging equation (2.31), the analytical expression for the integral reactivity variation due to temperature can be derived as follows

$$\begin{aligned}\rho_T(h, T) &= \int_{T_{ref}}^T \alpha_T(h, T') \delta T' = \\ &= \ln \left( \frac{\nu\Sigma_f(T)}{\Sigma_a(T)} \frac{1}{1 + M^2(T)B^2(h)} \right) - \ln \left( \frac{(\nu\Sigma_f)_0}{(\Sigma_a)_0} \frac{1}{1 + M^2(T_{ref})B^2(h)} \right),\end{aligned}\quad (2.34)$$

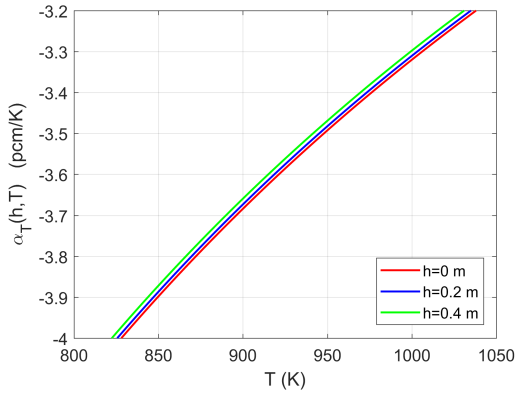
whereas, the integral reactivity variation due to geometry, inserting the equation (2.28), is

$$\rho_h(h, T) = \int_{h_{ref}}^h \alpha_T(h', T) \delta h' = \ln \left( \frac{1 + M^2(T)B^2(h_{ref})}{1 + M^2(T)B^2(h)} \right).\quad (2.35)$$

From a physical point of view, some considerations regarding the results found above can be made. As far as equation (2.34) is concerned, a careful look can notice that the quantity  $\rho_T(h, T)$  is equal to the natural logarithm of the effective multiplication factor  $k$  at temperature  $T$  and length  $h$  to  $k$  at the reference temperature  $T_{ref}$  and same length  $h$  ratio. Regarding the integral reactivity


 (a) Temperature feedback coefficient due to variation of  $k_\infty$ .


(b) Temperature feedback coefficient due to variation of migration area.



(c) Total temperature feedback coefficient.

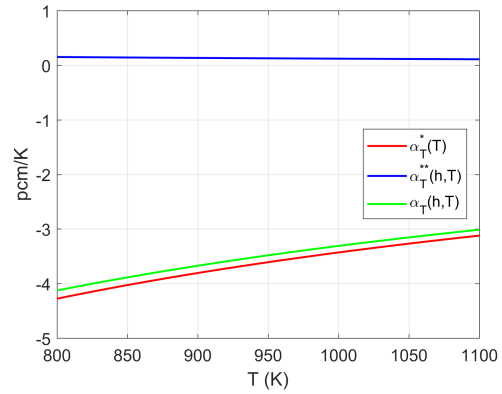

 (d) Comparison between temperature feedback coefficients, with  $h=0.2$  m.

Figure 2.7: Temperature feedback coefficients as functions of temperature. The coefficient  $\alpha_T^{**}(h,T)$  depends also on the monitor length  $h$ , and indeed its dependence is transferred to the total temperature coefficient. The contribution of migration area variation is much lower than one of  $k_\infty$ , as you can see in top bottom right figure.

variation due to geometry, equation (2.35), it results being equal to the natural logarithm of the probability of non leakage computed at  $T$  and  $h$  to the same quantity but computed at  $T$  and  $h_{ref}$ . Figure 2.8 reports the trend of the integral variation of reactivity as a function of  $h$  for a fixed temperature. The system starts from a condition of supercriticality, where the geometry reactivity is about 500 pcm. Then, as the molten salt is drained, the system reaches the reference cylinder height and the reactivity decreases until criticality (about 0.2 m for the case in figure 2.8). Consequently the reactivity continues to decrease rapidly. Those huge values of reactivity reached for  $h$  larger than 1 m are physically meaningless: the neutron flux is already shut down long before.

As far as the reference temperature  $T_{ref}$  is concerned, it is imposed equal to 900 K [13]. Concerning the reference length instead, remind that a multiplying system is critical if the geometrical buckling, expressed by equation (2.26) and computed at  $h = h_{ref}$ , is equal to the material

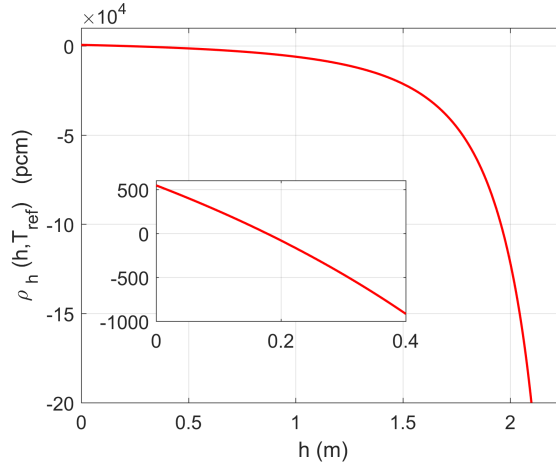


Figure 2.8: Integral variation of reactivity due to geometry change  $\rho_h(h, T)$  as a function of the monitor length  $h$  for a fixed temperature of 900 K.

buckling as follows

$$\frac{k_\infty(T_{ref}) - 1}{M^2(T_{ref})} = B^2(h_{ref}), \quad (2.36)$$

where nuclear parameters refer to temperature of 900 K ( $T_{ref}$ ). Plugging equation (2.26), the expression of the reference monitor length can be obtained

$$h_{ref} = H - \pi \left( \frac{(\nu\Sigma_f)_0 - (\Sigma_a)_0}{(D_n)_0} - \left( \frac{j_{01}}{R} \right)^2 \right)^{-1/2}. \quad (2.37)$$

The geometry, for which the system is critical, is defined in an univocal way by  $h_{ref}$ . The  $\rho_h(h, T)$  dependence on temperature is very slight, since it is related to variation of the migration area  $M^2(T)$  which slightly changes with temperature.

### 2.3.3 Heat source from fissions and decay heat

The power source term in equation (2.12),  $\dot{Q}_f(t)$  (W), is related to neutronics and contains two contributions: the instantaneous deposition of heat due to fissions and the decay heat.

When a fission event occurs, the total energy generated is about 200 MeV. Anyway, only a fraction of this energy amount is instantaneously deposited in the medium. The remaining part is contained in the fission products, stored for some time and then emitted through  $\gamma$ ,  $\beta$  and neutron decay events and deposited in the medium.

The total fission volumetric power  $\dot{q}_{fis}(t)$ , measured in Watt per unit volume, emitted at a certain time instant is expressed by the following formula

$$\dot{q}_{fis}(t) = E_f \Sigma_f(T) \Phi(t) = E_f \Sigma_f(T) v n(t) = E_f \Sigma_f(T) v n_0 \eta(t), \quad (2.38)$$

where  $E_f \Sigma_f(T)$  is the energy per fission event produced multiplied times the fission cross section (J/m; see equation (1.1)) and  $v$  the neutron speed (table 1.3). Note that  $\dot{q}_{fis}(t)$  is a function of

only  $t$ , since the temperature is in turn a function of time, say  $T(t)$ .

As already said, the large part of this power is directly deposited in the medium, while a fraction  $f$  (table 1.5) is stored into decay heat precursors and emitted later in time. Writing a balance for the decay heat precursors in terms of the energy stored in them, where the source is represented by the fraction  $f$  of fission energy produced and the sink is the decay event, yields

$$\frac{dq_d(t)}{dt} = f\dot{q}_{fis}(t) - \lambda_d q_d(t), \quad (2.39)$$

where  $q_d(t)$  is the decay energy stored in the precursors per unit volume ( $\text{J}/\text{m}^3$ ) and  $\lambda_d$  is the decay event rate ( $1/\text{s}$ ). One group of decay heat precursors is considered. An outflow term has to be included in the decay heat precursor balance, but, assuming a spatially uniform distribution, it goes away as for the neutron precursors.

Consequently the proportion of volumetric power emitted by decay heat precursors corresponds to the term  $\lambda_d q_d(t)$  ( $\text{W}/\text{m}^3$ ).

By summing the instantaneous fission energy production and the decay heat, the total volumetric thermal power source is then obtained:

$$\dot{q}_f(t) = (1 - f)\dot{q}_{fis}(t) + \lambda_d q_d(t). \quad (2.40)$$

Multiplying it times the molten salt volume, which is time-dependent, the energy source appearing in equation (2.12) can be finally derived:

$$\dot{Q}_f(t) = \dot{q}_f(t) R^2 \pi (H - h(t)). \quad (2.41)$$

### 2.3.4 Molten salt level sub-model

In the previous sections, the energy balance and the neutronic physics mathematical sub-models are illustrated and described. The equations governing the temperature and the neutronic variables contain a term that is left unexplained until now: the free surface velocity  $v_A(t)$

$$v_A(t) = \frac{dh(t)}{dt}. \quad (2.42)$$

It is clear that the dynamics of the fuel salt draining depends strongly on the time derivative of the monitor length  $h$ . It identifies the time evolution of the free surface of the salt that is emptying the tank and affects the energy content in the system and mostly the neutronic dynamics. Therefore modelling of  $dh/dt$  constitutes the closure to our problem.

Isothermal draining phenomena of incompressible fluids are old and well-established problems. An analytical solution is available in the current literature [20]. However, the molten salt fuel draining presents strong temperature variations during the transient and in principle it is not possible to treat it as isothermal. As a first approximation in the present study the approach explained in [20] for isothermal draining phenomena is adopted, even if temperature variations are the main concern of the problem. The approximation allows to find a first guess of the free surface evolution of molten salt in time. Better functions for  $h(t)$  could be developed in the future. Nevertheless, for what is worth in this work, this assumption is suitable to analyse the reactivity and the temperature draining transients. Moreover the draining time estimated with this approach are conformed to those in the current literature ([10]) and also CFD simulations (section 3.6.2) will confirm the

suitability of the approach adopted also for strongly non-isothermal transients.

As already said, to express analytically the time dependency of the salt free surface is adopted a procedure for common drainage problems present in the current literature for isothermal incompressible fluids [20]. The method assumes a quasi-steady set of equations: an unsteady mass balance, while a steady energy balance.

As far as the energy balance is concerned, the Bernoulli's law is applied between control surfaces A and B, including dissipations due to frictions and local losses, since the three mechanical energy terms possess comparable weights. The Bernoulli's law, written in terms of energy head (meter), states that

$$z_A(t) - z_B + \frac{p_A - p_B}{\delta g} + \frac{v_A^2(t) - v_B^2(t)}{2g} = H_{loss}(t) \quad (2.43)$$

where  $z$  is the elevation with respect to a reference height,  $p$  the fluid pressure,  $v$  the velocity and  $H_{loss}$  represents the head losses; subscripts A and B identify respectively CS A and B. As far as the potential energy term is concerned, the difference between the free surface elevation  $z_A(t)$  and the outlet elevation  $z_B$  corresponds to the height of the molten salt domain within the tank (see figure 2.1):

$$z_A(t) - z_B = H - h(t) + L. \quad (2.44)$$

While, regarding the kinetic term, the free surface velocity  $v_A(t)$  can be neglected with respect to the outlet velocity. Concerning the head losses, they refer to both continuous friction of fluid moving along the wall surfaces and local loss due to tank-pipe contraction. Moreover the frictions could be split in two terms referring to fluid moving along the tank wall surfaces and along the pipe surfaces. Continuous friction pressure drop can be computed multiplying the kinetic energy times the length-to-diameter ratio of the duct and in turn times a friction factor (Darcy's formula). Whereas, for a local loss, the kinetic energy has to be multiplied times a factor of concentrated loss, that depends on the type and geometry of the pressure drop [21]. Therefore the expression for the head losses  $H_{loss}$  is as follows

$$H_{loss}(t) = 4C_t \frac{H - h(t)}{2R} \frac{v_A^2(t)}{2g} + 4C_p \frac{L}{d} \frac{v_B^2(t)}{2g} + K_c \frac{v_B^2(t)}{2g} \quad (2.45)$$

where  $C_t$  and  $C_p$  are respectively the Fanning friction factors for the tank wall and the shaft wall and the  $K_c$  the local friction factor due to tank-pipe contraction. The three terms in equation (2.45) are thus, in the same order, the continuous head loss due to friction against the tank wall, the continuous head loss due to friction against the bottom pipe wall and the local head loss due to tank-pipe contraction.  $v_A(t)$  can be related to  $v_B(t)$  using equation (2.5); in this way, gathering the kinetic energy related to the outlet velocity, it yields

$$H_{loss}(t) = \left( 4C_t \frac{H - h(t)}{2R} \left( \frac{d}{2R} \right)^2 + 4C_p \frac{L}{d} + K_c \right) \frac{v_B^2(t)}{2g}. \quad (2.46)$$

Assuming smooth surfaces, different correlations are available in the literature for the Fanning friction factor. A suitable correlation of the latter quantity as a function of the Reynolds number is the Morrison's correlation [22]. The valuable characteristic for this correlation is its wide validity range ( $Re < 10^6$ ). The expression of the Morrison's correlation is as follows

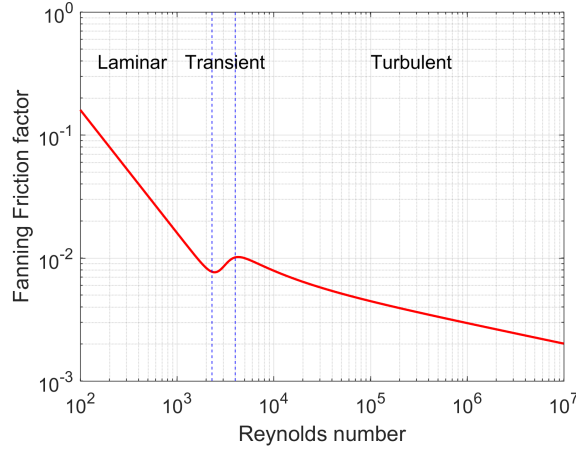


Figure 2.9: Morrison’s correlation for Fanning friction factor as a function of Reynolds number for smooth pipes (Morrison, 2013). It is valid for laminar, transient and turbulent flow regimes ( $Re < 10^6$ ).

$$C(Re) = \frac{16}{Re} + \frac{0.0076(3170/Re)^{0.165}}{1 + (3170/Re)^7}, \quad (2.47)$$

while its graphical representation is plotted in figure 2.9. The flow in both the tank and the pipe is turbulent (average Reynolds numbers are  $Re_p = 7.4 \times 10^5$  and  $Re_t = 4.7 \times 10^4$  respectively for the pipe and the tank). The Fanning friction factor strongly depends on the Reynolds number in the laminar regime, while for turbulent flow regimes it could be assumed constant. Therefore Fanning factors could be computed with the Morrison’s correlation at  $Re$  equal to the values above and constant numbers could be adopted for the tank and the pipe wall friction:

$$\begin{aligned} C_p &= C(Re_p) \simeq 0.0031; \\ C_t &= C(Re_t) \simeq 0.0054. \end{aligned} \quad (2.48)$$

As far as the local pressure drop is concerned, the local friction factor  $K_c$  is equal to 0.5 for sudden contractions where the pipe-to-tank contraction area ratio tends to zero [23]. Substituting equation (2.45) into equation (2.43) and solving for  $v_B$ , it yields

$$v_B(t) = \sqrt{\frac{2g(H - h(t) + L) + 2(p_A - p_B)/\delta}{4C_t \frac{H-h(t)}{2R} \left(\frac{d}{2R}\right)^2 + 4C_p \frac{L}{d} + K_c + 1}}. \quad (2.49)$$

The term related to friction along the tank surface is negligible with respect to the other terms in the denominator. It follows

$$v_B(t) = \sqrt{\frac{2g(H - h(t) + L) + 2(p_A - p_B)/\delta}{4C_p \frac{L}{d} + K_c + 1}}. \quad (2.50)$$

Defining the dimensionless constant  $\theta$  as

$$\theta = \sqrt{\frac{1}{4C_p \frac{L}{d} + K_c + 1}}, \quad (2.51)$$

equation (2.50) becomes

$$v_B(t) = \theta \sqrt{2g(H - h(t) + L) + 2\frac{p_A - p_B}{\delta}}. \quad (2.52)$$

Reconsider now equation (2.5) expressing the unsteady mass balance of the salt draining. Plugging the relation for  $v_B(t)$  found in equation (2.52) it is obtained

$$v_A(t) = \frac{dh(t)}{dt} = \left(\frac{d}{2R}\right)^2 v_B(t) = \left(\frac{d}{2R}\right)^2 \theta \sqrt{2g(H - h(t) + L) + 2\frac{p_A - p_B}{\delta}}. \quad (2.53)$$

It is derived an ODE for the variable  $h$  as a function of time, which, knowing the initial condition  $h(0)=0$  (tank full of salt), becomes an initial value problem. The solution is as follows

$$h(t) = H + L - \left( \sqrt{H + L + \frac{p_A - p_B}{\delta g}} - \sqrt{\frac{g}{2} \left(\frac{d}{2R}\right)^2 \theta t} \right)^2 + \frac{p_A - p_B}{\delta g}. \quad (2.54)$$

The time evolution of the salt free surface results is a second degree polynomial of  $t$ . From the above equation, deriving with respect to time yields

$$\frac{dh}{dt} = \theta \sqrt{2g} \left(\frac{d}{2R}\right)^2 \left( \sqrt{H + L + \frac{p_A - p_B}{\delta g}} - \sqrt{\frac{g}{2} \left(\frac{d}{2R}\right)^2 \theta t} \right). \quad (2.55)$$

Equation (2.54) represents the closure to the problem analysed. Having an analytical expression for the salt free surface time evolution, the equations governing the temperature and the neutronics are fully defined and numerically solvable.

The draining time corresponds to the time period needed to empty completely the tank. The analytical expression can be derived from equation (2.54) imposing  $h(t^*)$  equal to  $H$  and solving for  $t^*$ . It is obtained:

$$t^* = \frac{1}{\theta} \frac{\sqrt{2}}{g} \left(\frac{d}{2R}\right)^2 \left( \sqrt{\frac{p_A - p_B + \delta g(H + L)}{\delta}} - \sqrt{\frac{p_A - p_B + \delta gL}{\delta}} \right). \quad (2.56)$$

Imposing atmospheric pressures both for the free surface and the bottom pressures, the expression of the draining time is rearranged as

$$t^* = \frac{1}{\theta} \frac{\sqrt{2}}{g} \left(\frac{d}{2R}\right)^2 \left( \sqrt{\frac{\delta g(H + L)}{\delta}} - \sqrt{\frac{\delta gL}{\delta}} \right) \quad (2.57)$$

and results being 94.82 s, that is in the range expected in [10]. In turn, the pressure difference goes away also in equation (2.54) and (2.59) yielding respectively

$$h(t) = H + L - \left( \sqrt{H + L} - \sqrt{\frac{g}{2} \left(\frac{d}{2R}\right)^2 \theta t} \right)^2 \quad (2.58)$$

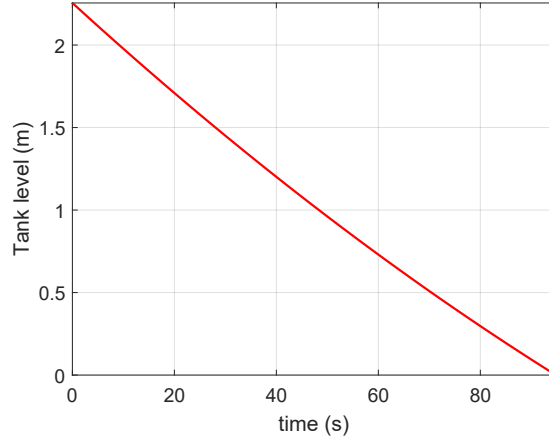


Figure 2.10: Molten salt level evolution in time. It goes from the the initial value  $H=2.255$  m (full tank) to zero (empty tank).

and

$$\frac{dh}{dt} = \theta \sqrt{2g} \left( \frac{d}{2R} \right)^2 \left( \sqrt{H+L} - \sqrt{\frac{g}{2} \left( \frac{d}{2R} \right)^2 \theta t} \right) = \theta \sqrt{2g} \left( \frac{d}{2R} \right)^2 \sqrt{H-h(t)+L}. \quad (2.59)$$

The molten salt level in the core time evolution is plotted in figure 2.10. Remind that it is computed simply subtracting from the total tank height  $H$  the distance from the top of the free surface  $h(t)$  (figure 2.1).

### 2.3.5 Analytical expression for geometry-related reactivity

Assume now to fix the system temperature to the reference  $T_{ref}$ , where the contribution to the total reactivity due to temperature effects are null ( $\rho_T=0$ ). The purpose is to write down an analytical expression for the evolution in time of the system reactivity due to moving boundaries of a multiplying domain, as the molten salt fuel during the draining.

The system reactivity due to only geometrical changes is expressed by equation (2.35). The reference length  $h_{ref}$  is equal to 0.1768 m, i.e. the system is critical at about 20 cm from the top of the tank. Combining equations (2.35) and (2.58) together with the definition of the buckling in equation (2.26), it is possible to write down the time evolution of the reactivity due to variation of the height of a cylindrical multiplying system:

$$\rho_h(t) = \ln \frac{k_\infty(T_{ref})}{1 + M^2(T_{ref}) \left( \left( \frac{j_{0,1}}{R} \right)^2 + \pi^2 \left( \left( \sqrt{H+L} - \sqrt{\frac{g}{2} \left( \frac{d}{2R} \right)^2 \theta t} \right)^2 - L \right)^{-2} \right)}. \quad (2.60)$$

The geometry-related reactivity evolution is shown in figure 2.11. The system starts from a condition of supercriticality: the volume at  $t=0$  is larger than the critical volume. Then the multiplying

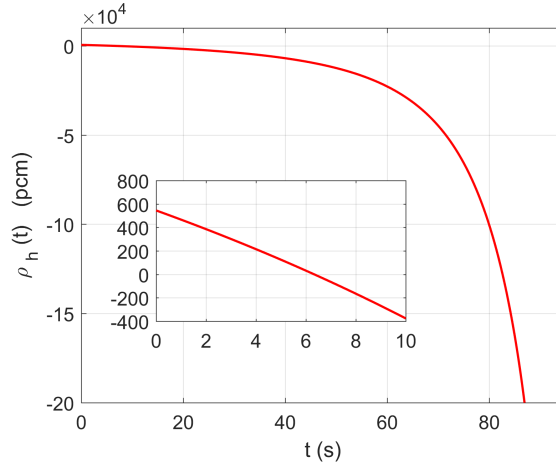


Figure 2.11: System reactivity as function of time due to geometry change (molten salt draining) for a fixed value of temperature.

domain height is shortening, since the molten salt is draining. The salt volume is decreasing, which implies the increase of neutron leakages and indeed the decrease of reactivity. The system hence becomes critical when the monitor length  $h$  approaches the reference value  $h_{ref}$ . After that the reactivity evolves rapidly towards values more and more negative while the cylindrical salt domain reduces.

### 2.3.6 Initial conditions

As far as the initial conditions are concerned, firstly it is set the initial value for the average temperature in the domain ( $T_0$ ): 700 °C has been chosen as the reference MSFR mean operating temperature (table 1.1).

Concerning the normalized neutron population and the normalized neutron precursors, they both are set to unity, assuming the equilibrium condition between neutrons and precursors before the transient beginning. The normalization quantity  $n_0$ , which is the initial neutron density in the system, can be derived from the total initial power  $\dot{Q}_f(0)$  defined, combining equations (2.40) and (2.41) at  $t = 0$ , as follows

$$\dot{Q}_f(0) = ((1 - f)\dot{q}_{fis}(0) + \lambda_d q_d(0)) R^2 \pi (H - h(0)). \quad (2.61)$$

Assuming steady-state conditions for the decay heat precursors before the transient, from equation (2.39) it can be obtained that the term  $\lambda_d q_d(0)$  corresponds exactly to  $f\dot{q}_{fis}(0)$ . Furthermore, knowing that  $h(0) = 0$  (full tank at  $t = 0$ ), it yields

$$\dot{Q}_f(0) = \dot{q}_{fis}(0) R^2 \pi H. \quad (2.62)$$

Making explicit  $\dot{q}_{fis}(t)$  from equation (2.38) and imposing  $\eta(0) = 1$ , equation (2.62) can be solved in  $n_0$  to find the initial neutron population as follows

$$n_0 = \frac{\dot{Q}_f(0)}{E_f \Sigma_f(T_0) v R^2 \pi H}. \quad (2.63)$$

Table 2.2: List of initial conditions.

Mean system temperature	$T_0$	700 °C
Normalized neutron density	$\eta(0)$	1
Normalized precursor concentration	$\xi(0)$	1
Total system thermal power	$\dot{Q}_f(0)$	$3.5 \times 10^9$ W
Neutron population	$n_0$	$1.33 \times 10^{13}$ neutron/m <sup>3</sup>
Neutron precursors concentration	$C_0$	$7.68 \times 10^{17}$ 1/m <sup>3</sup>
Decay heat precursor energy	$q_d(0)$	$1.16 \times 10^8$ J/m <sup>3</sup>

Thence, from equation (2.21), the initial neutron precursor concentration  $C_0$  can be derived. Initial conditions for the draining problem presented in this study are grouped and listed in table 2.2. The model has four grades of freedom, which are constituted by setting the initial values for the mean salt temperature, the normalized neutrons and neutron precursors and the total system power. Specifically, 3.5 MW for the total thermal power is slightly larger than the reference MSFR thermal power to simulate a power ramp during which a certain accident occurs and triggers the salt draining.

Lastly, the 0-D energy balance, equation (2.12), requires the specification of  $T_B(t)$ . Such boundary is represented by equation (2.14), which specifies analytically the temperature difference  $T(t) - T_B(t)$ .

## 2.4 Semi-analytical model simulations

The governing equations, that model the draining of molten salt fuel, present a strong coupling among them and high non-linearity. The energy source depends on both neutron population and decay heat precursor concentration. The first one is affected by the system reactivity, that is the expression of temperature again and geometry. The decay heat precursors are in turn dependent on neutrons. The geometry, which also affects the temperature equation, is defined through an analytical expression of the molten salt free surface as function of time.

The model is composed indeed by a set of strongly coupled non-linear equations; it then follows the need to be solved them numerically. Although the ordinary differential equations are solved with numerical mathematical methods, they are fed by analytical expressions, in the sense that analytical equations for the salt free surface time evolution and for the mean-outflow temperature difference are inputs for the whole model. This is why semi-analytical model stands for.

### 2.4.1 Simulink environment

The ordinary differential set of equations is solved numerically using the MathWorks Simulink platform [24]. Simulink is a block diagram environment for Model-Based Design. Model governing equations are implemented on Simulink as block diagrams, connections and mathematical operation boxes and the numerical solution is obtained as discrete values associated to a discrete time vector. The process of computing the states of a model, time step by time step, is known as solving the model [24]. The choice of the solver is strictly important in solving a numerical problem on

Table 2.3: Time scales of the different physical phenomena involved in the fuel salt draining.

Physics		Time scale (s)
Temperature	$\tau_T$	0.96
Neutrons	$\tau_n$	$10^{-6}$
Neutron precursors	$\lambda_p^{-1}$	16
Decay heat precursors	$\lambda_d^{-1}$	13

Simulink. The simplified coupled thermo-hydraulic and neutronic multiphysics problem presents time scales that range from the neutron one ( $\sim 10^{-6}$  s) to precursors' time scales ( $\sim 10$  s). They are listed in table 2.3. Numerical problems, characterized by largely different time scales, are referred as *stiff*. Actually, it is not straightforward to define an equation system being stiff, but the main idea is that it includes some terms that can lead to rapid and unstable variations in the solution. Equation sets with wide time scale range are surely included among stiff problems.

A suitable solver must be selected in order to solve stiff model equations, otherwise it will be ineffective and the solution completely incorrect. Among the available solvers offered by the Simulink environment, it is individuated the *ode15s*. It is a variable-order solver based on the numerical differentiation formulas (NDFs). NDFs are related to the Gear's method [24, 25].

### 2.4.2 Model scheme

The model is represented as block diagrams and implemented on Simulink (figure 2.12). The scheme is arranged to reproduce the three sub-models described in the previous pages. In light blue the block to produce the signal regarding the free surface of molten salt. Remind that it is fully analytical and refers to equation (2.58). The green block at center contains block diagrams modelling the neutronics governing equations (neutron point kinetics with system reactivity, neutron precursors and decay heat precursors). Lastly, the red block regards the energy equation (2.12).

In the green block, it is generated the monitor length  $h(t)$  signal that, as already mentioned, represents a feeding signal for both the neutronics and the energy blocks. The latter one also requires as input the energy source from fissions and decay heat and returns the temperature signal in time. In turn, the temperature and the monitor length  $h$  are inputs in order to compute the system reactivity within the neutronics block. Among the different quantities of interest given back by the green block, there is the thermal power production that goes into the energy block, closing the loop. Furthermore it could be said in principle that if one would like to model the temperature dependence about the salt properties, there will be also a temperature feedback signal to feed the blue block again.

## 2.5 Results and plots

Simulations of the zero-dimensional semi-analytical model of fuel salt draining are now launched, shown and discussed.

The section is organized as follows. At first, it will be shown and commented results and relative graphs regarding the simulation with input parameters discussed in the previous pages, giving an overview on the physics and dynamics of the fuel draining. Subsequently an uncertainty analysis is carried out concerning thermo-physics and the neutronics properties of fuel salt.

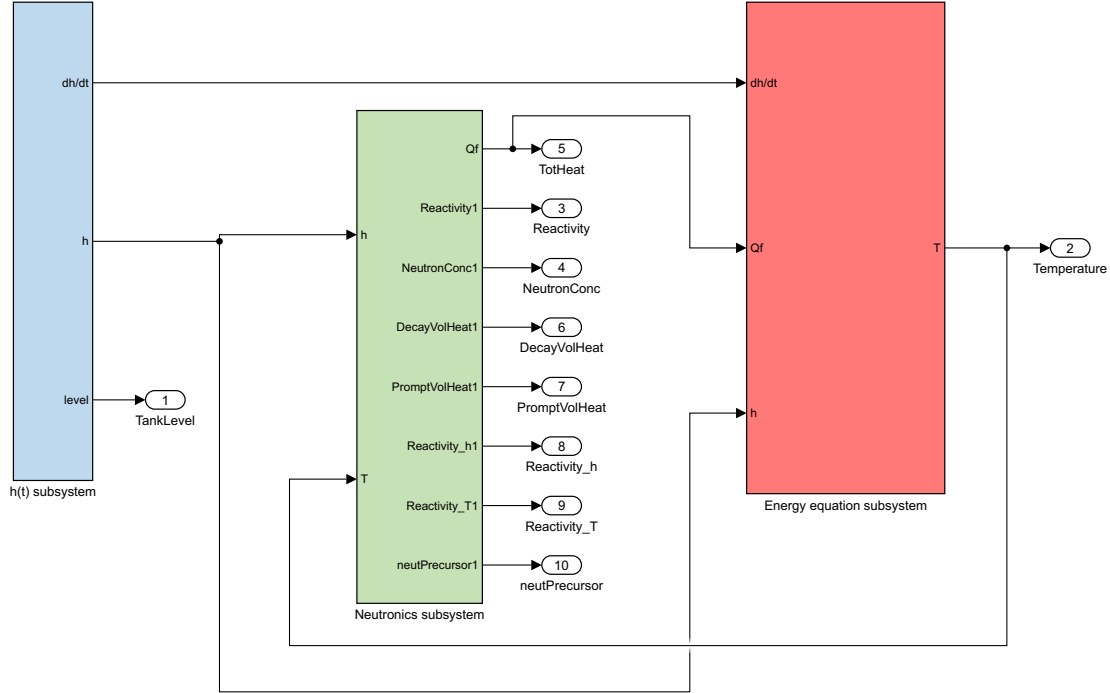


Figure 2.12: Simulink scheme of the fuel salt draining model. The light blue, the green and the light red blocks represent respectively the salt fluid-dynamics, the neutronics and the energy sub-models.

### 2.5.1 Simulation results

At  $t=0$  the tank is full of molten salt, the system temperature is  $700\text{ }^{\circ}\text{C}$  ( $973\text{ K}$ ) and the core thermal power corresponds to  $3.5\text{ MW}$ . Furthermore the system is in a supercritical state, with a reactivity of  $285\text{ pcm}$  ( $0.85\text{ \$}$ ). An hypothetical emergency situation is assumed and the draining transient then starts.

Figure 2.13 shows the system reactivity evolution during the first 7 seconds. The green and the blue lines are respectively the terms  $\rho_h(h, T)$  and  $\rho_T(h, T)$  described in equations (2.34) and (2.35). Their summation produces the total system reactivity, in red. The integral reactivity due to temperature is negative as a result of temperature feedback (the system starts from an initial value larger than the reference temperature  $T_{ref}$ ). Conversely the molten salt cylinder is larger than the critical configuration (which is reached at  $h_{ref}=0.1768\text{ m}$  and about  $6.5\text{ s}$ ), producing an overall supercritical initial phase. The latter one lasts about 1 second, but has a strong impact on the system dynamics.

The initial supercritical phase induces a sudden increase in the number of neutrons in the system (figure 2.14a), that rises up from its initial value of  $1.33\times 10^{13}$  neutrons per meter cubed to about  $8.3\times 10^{13}$ , with the time scale of the effective neutron lifetime  $\Lambda$ . Such neutron production causes both the increase of neutron precursors (figure 2.14b) and decay heat precursors (figure 2.14d), since neutrons are involved in the sink terms of the precursors' governing equations.

The system temperature increases due to the production of heat coming from the instantaneous deposition from fission events (prompt volumetric heat, which is the dominant contribution) and from the decay heat. Figures 2.14c and 2.14d show the prompt and the decay volumetric heat

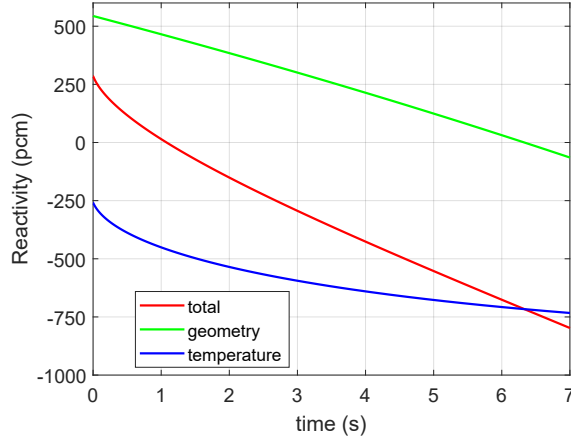


Figure 2.13: System reactivity as function of time, zoom on the first 7 seconds of transient. The red, the green and the blue lines represent respectively the total  $\rho(h, T)$ , the geometry-related  $\rho_h(h, T)$  and the temperature-related  $\rho_T(h, T)$  system reactivity.

time evolutions. The first one follows the trend of the neutron population, since it is proportional to  $\eta(t)$  according to equation (2.38). In turn, the temperature impacts strongly on the reactivity due to the negative feedback coefficient. Furthermore, the lowering of the salt free surface level causes the reduction of the multiplying system volume, the increase of neutron leakages and indeed another negative effect on neutron economics. Therefore the reactivity goes down and the system reaches the critical state within 1 s, then it goes towards more and more negative values. Neutrons suddenly drop down and the precursors approach their decay exponential forms (figures 2.14b and 2.14d).

As far as the temperature is concerned, its time derivative depends on three terms observing the RHS of equation (2.12):

$$\begin{aligned}\Pi_1(t) &= (T(t) - TB(t)) \frac{dh(t)}{dt}; \\ \Pi_2(t) &= -\frac{1}{2c_p} \left(\frac{2R}{d}\right)^4 \left(\frac{dh(t)}{dt}\right)^3; \\ \Pi_3(t) &= \frac{\dot{Q}_f(t)}{\delta c_p R^2 \pi}.\end{aligned}\tag{2.64}$$

The second term, related to outflow kinetic energy, is negligible all along the transient: it assumes values of the order of  $10^{-4}$  Km/s (figure 2.15a). The heat source, involved in the term  $\Pi_3(t)$ , is positive and causes the temperature to rise up during the first part of transient. However the contribution of the third term decreases in time, since the total heat rapidly decreases (figure 2.14e), and in the meanwhile the first term depending on the temperature difference between the mean value  $T(t)$  and the outflow value  $T_B(t)$  becomes dominant. After a while the first negative term overcomes the positive term related to heat production and the temperature begins to reduce (figure 2.15a). The heat source term is dominant for the first 20 s and then it is overcome by the term related to molten salt outflow. Figure 2.15b shows the relative weight of the terms in computing the temperature time derivative.

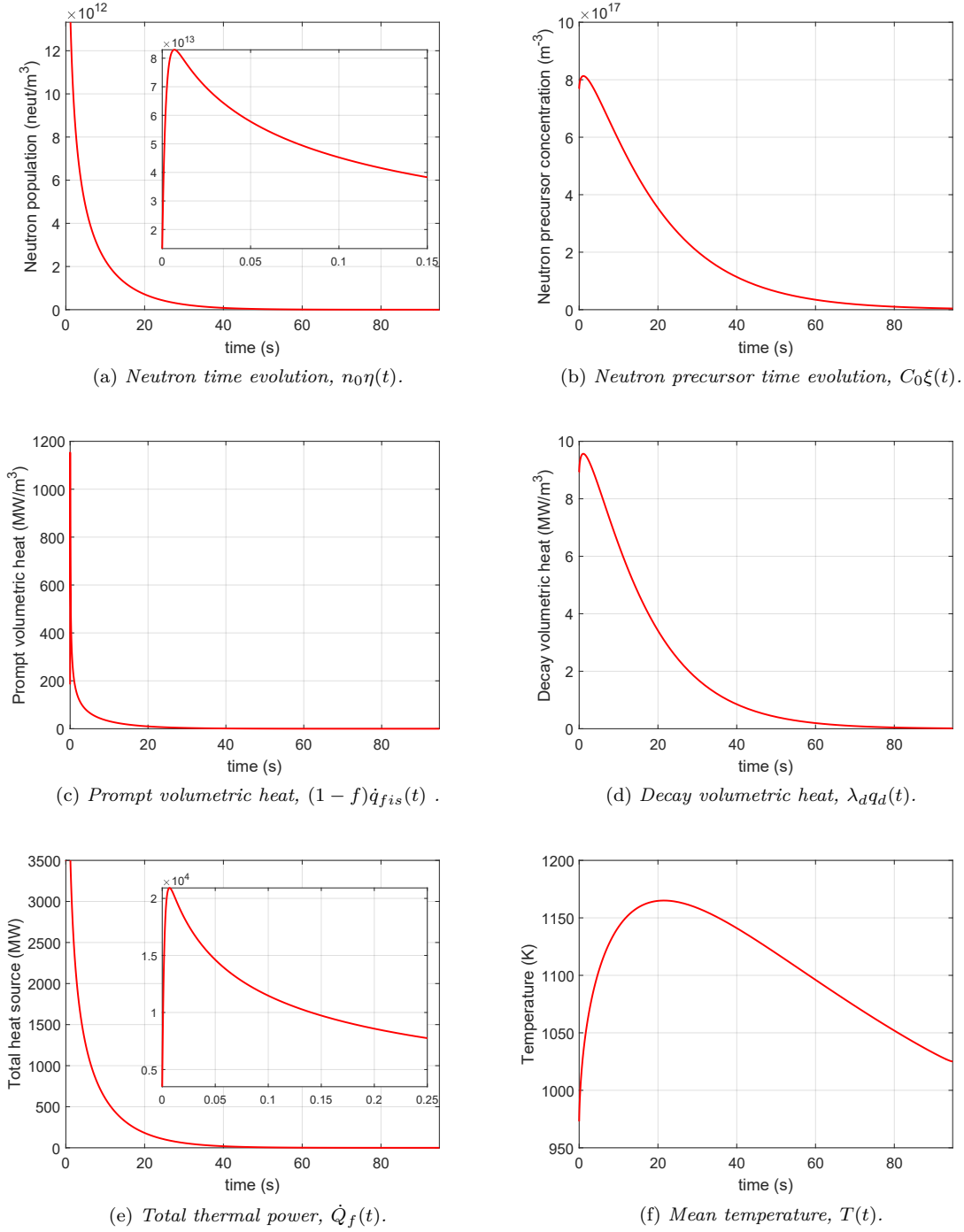


Figure 2.14: Simulation results of the 0-D semi-analytical model with input parameters of table 2.2.

The temperature time evolution is reported in figure 2.14f. The first part of the transient is characterized by the temperature ramp due to power production within the salt. The mean temperature

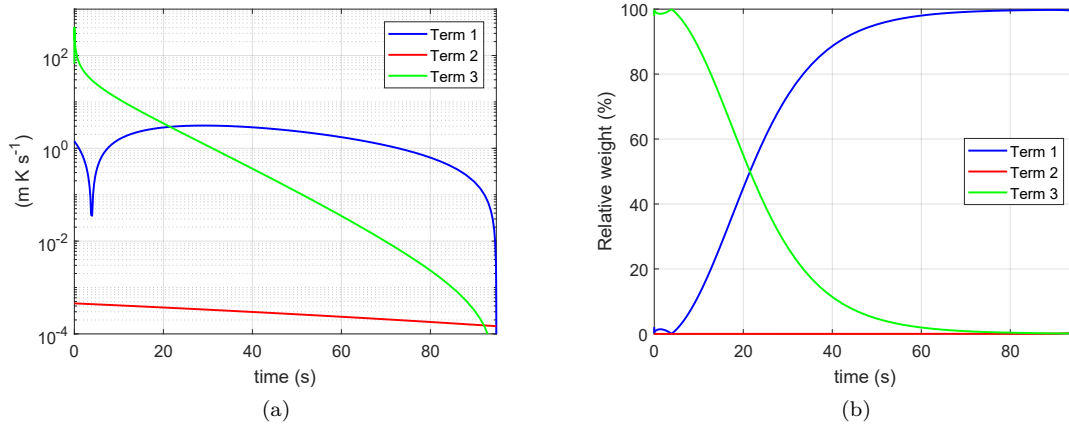


Figure 2.15: Terms of the RHS of energy equation as function of time. They are expressed by (2.64) and refer to equation (2.12). On the left, their values in a logarithmic scale, while in the right plot it is shown their relative weights.

increases by 200 K, reaching a peak of 1165 K (892 °C). This value is far below the critical temperature to cause damages to core inner surfaces. After this ramp, the molten salt outflow enthalpy overcomes the power source term and the temperature starts decreasing to reach 1025 K at the transient end.

The molten salt fuel is intrinsically safe. The strong temperature feedback coefficient (around -4 pcm/K) causes the immediate reactor shutdown in case of hazardous temperature (or power) rise.

Remind that the results reported above are based on the energy equation (2.12) closed with relation (2.14) derived from CFD analyses. It could be of interest to see the temperature transient if the energy equation was closed keeping constant the free surface temperature  $T_A$ , as reported in equation (2.13). Figure 2.16 compares the temperature evolutions obtained using equation (2.14) and constant  $T_A$  as boundary condition to the energy equation. The constant- $T_A$  model is significantly affected by the choice of  $T_A$ , both in the tail of the transient and in the temperature peak. This model is considered too much approximate and, for this reason, discarded.

## 2.5.2 Local uncertainty analysis

An uncertainty analysis is carried out to understand and quantify the effects on the solution, in terms of temperature, reactivity and heat production, regarding variations of thermo-physical and neutronic properties of the molten salt fuel.

The one-factor-at-time method (local uncertainty) is adopted: a parameter varies at a time while keeping others fixed [26]. An uncertainty of  $\pm 10\%$  on thermo-physical and neutronic parameters is studied and the effect on the model solution is evaluated.

As far as the mass density is concerned (figures 2.17a and 2.17b), an increase in the density causes a decrease in the source term of energy equation (2.12). Indeed higher mass densities implies a lower temperature transient. This in turn causes a minor temperature reactivity feedback; it results in an increase of neutron population, and thence of power production, but it is of small effect.

The viscosity of the fluoride salt, in conformity with the developed model, has an impact on the calculation of the parameter  $\theta$  according to equation (2.51). The temperature variations caused

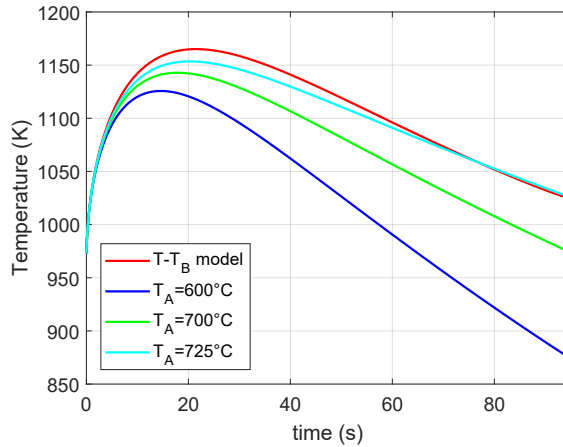


Figure 2.16: Comparison between the two boundary conditions considered for the energy equation: in red the time-varying temperature difference  $T(t) - T_B(t)$  expressed by equation (2.14); in blue, green and cyan the constant- $T_A$  boundary condition represented by equation (2.13).

by the viscosity uncertainties is negligible, whereas it implies a slight variation on the draining period: the larger viscosity, the larger the draining time to empty the tank.

Concerning the specific heat (figures 2.17c and 2.17d), it has the same effects on the solution as the mass density (look at the energy equation).

As far as neutron cross sections and diffusion coefficient are concerned, the variation of the single parameter as a heavy effect on the solution. As an example, the increase of the fission cross section of the 10 % causes an initial reactivity of 30 \$, resulting in an unphysical solution. This is why uncertainties regarding cross sections and diffusion coefficient are studied all together. In this sense, the variation on the temperature evolution is negligible.

The effective mean generation time  $\Lambda$  determines the slope of the neutron jump up to the peak. It has no implication on the magnitude of the peak, neither to solution transient after the neutron peak. Therefore it has no influences on the whole solution.

The neutron precursor decay constant,  $\lambda_p$ , has impact on the transient tail. In fact, lower decay constants mean an increase in the delayed neutron production and indeed in the power generation. This hence results in a higher temperature in the transient tail (figure 2.17e). The same is valid for the decay constant of decay heat precursors, where its evolution is reported in figure 2.17f.

As far as  $\beta$  is concerned, this has a strong impact on neutronics, since it establishes how much precursors are important in the neutron dynamics and further it has a direct impact on the neutron prompt jump. Larger delayed neutron fractions enhance the neutron precursor importance and indeed imply smaller prompt neutron jumps (figure 2.18c). The temperature is anyway affected by less than the 0.6 %.

Lastly, the decay heat precursor fraction has a negligible impact on the solution.

Finally, the uncertainty analysis results are summarised in table 2.4. It shows the maximum variation on the temperature transient if a parameter, listed in the left column, is varied of plus or minus 10 % with respect to its nominal value, that the reader can find in tables 1.2, 1.3, 1.4 and 1.5.

Concluding, superimposing the effects of all parameter uncertainties, the overall relative discrepancy on the temperature transient is obtained and corresponds to  $\pm 6$  %.

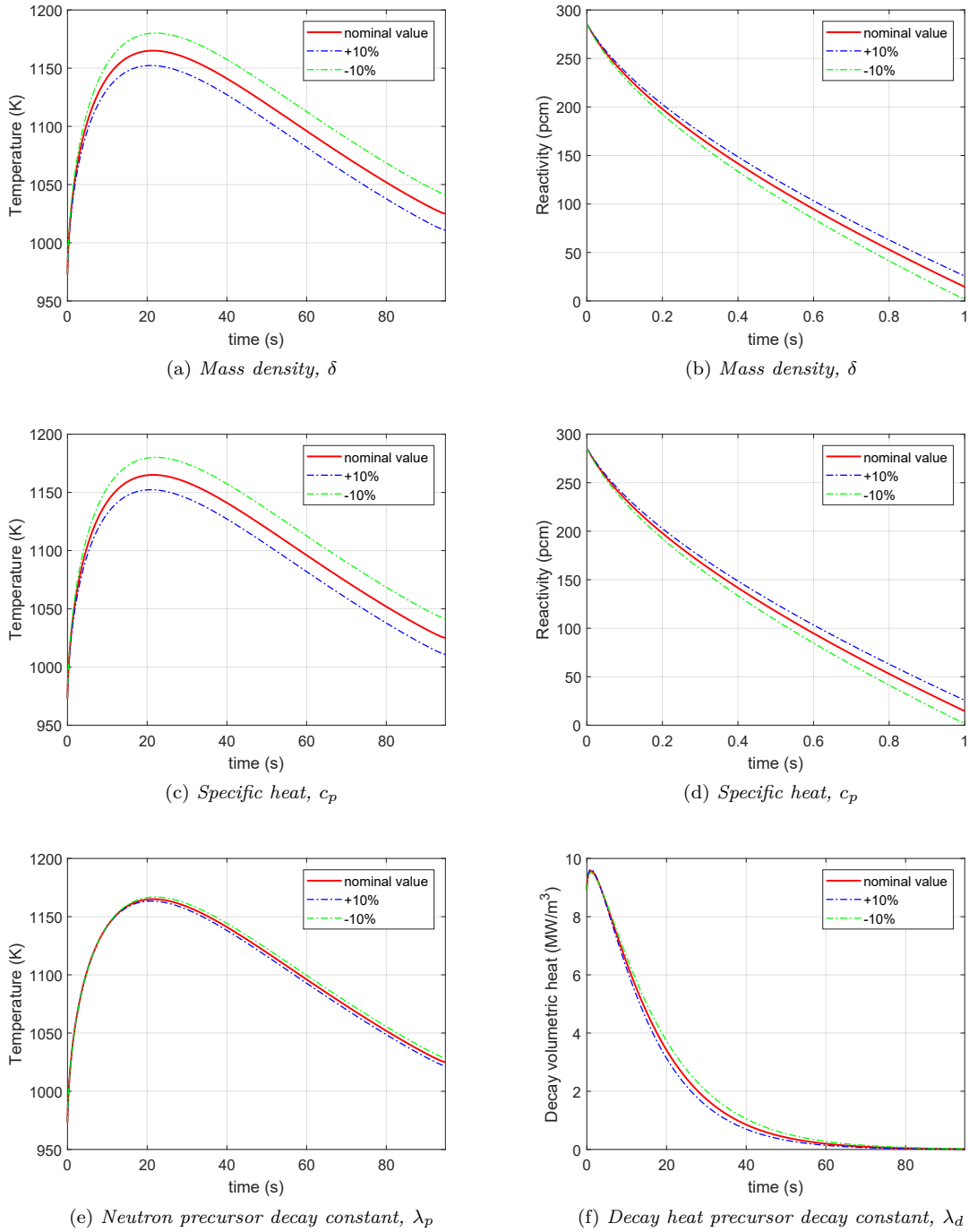


Figure 2.17: Transients of temperature and other variables of interest, where the nominal problem solution (red line) is compared with variation of parameters of  $\pm 10\%$  (dash-dot lines).

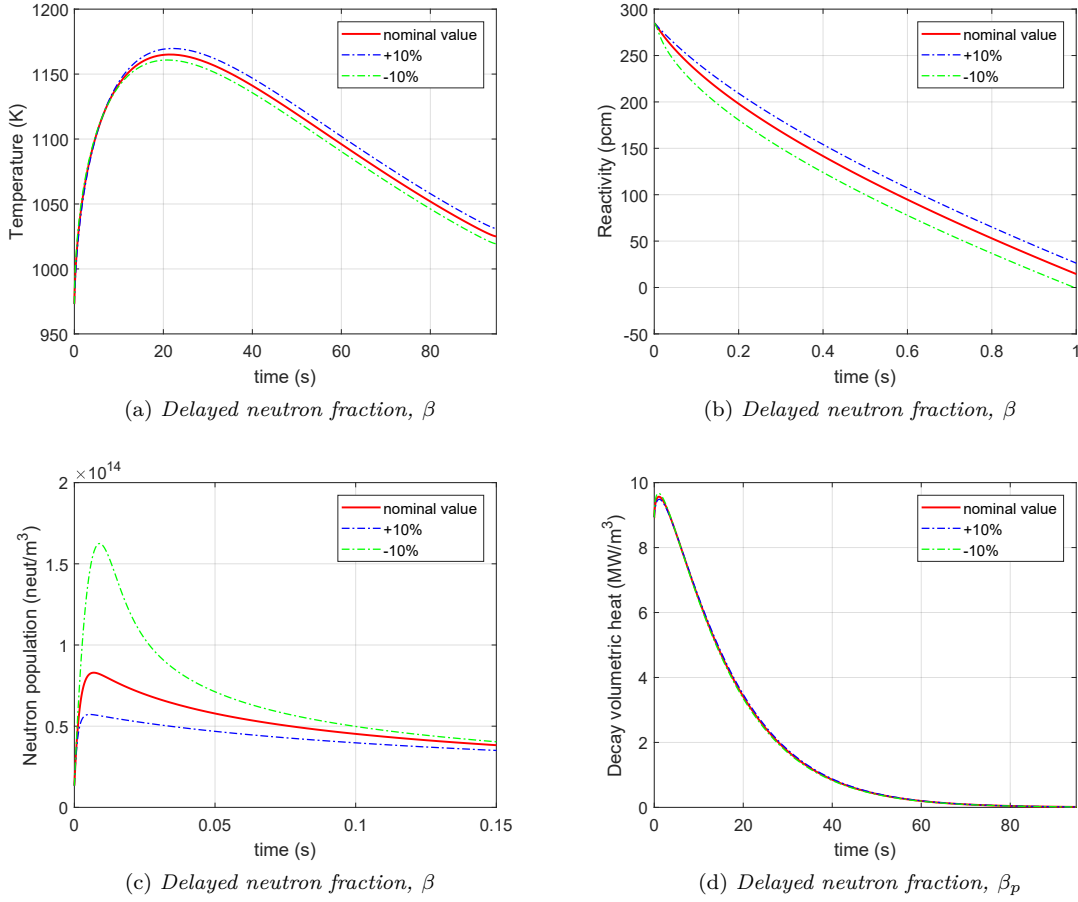


Figure 2.18: Refer to figure 2.17 for the caption.

## 2.6 Concluding remarks

The Emergency core Draining System is a fully-passive safety system concept thought for liquid-fueled molten salt reactors. In case of severe accidental situations, salt plugs, located at the core bottom, open and the fuel salt starts being drained, thanks to gravitational force, and stored in a draining tank underneath the core.

A simplified zero-dimensional semi-analytical model is proposed to capture the multiphysics phenomena involved in the fuel draining. Point kinetics equations are used to model the neutronics and are coupled with the energy equation that governs the temperature. The salt level time evolution is finally given analytically, adopting a quasi-steady approach, to close the problem.

The reactivity decreases in time due to twofold phenomena: the increase of the temperature (the salt has strongly negative feedback coefficient) and the volume decrease (that means the increase in neutron leakages). The fuel salt draining gives the opportunity to study a volume-change multiplying domain problem and to derive a general analytical model to describe the reactivity feedback due to geometry variations.

The temperature rises up for the first 20 seconds thanks to thermal power production related to fissions and decay heat. From the initial value of 700 °C, it reaches its peak of about 900 °C, that

Table 2.4: Maximum relative variation of the temperature transient for a parameter shift of  $\pm 10\%$  from its nominal value. The center column shows temperature maximum change for a parameter increase of 10 %, while in the right column the parameter is decreased of the same percentage.

Parameter	Maximum relative variation on the temperature (%)	
	+10 %	-10 %
$\delta$	-1.4	+1.6
$\nu$	+0.02	-0.02
$c_p$	-1.4	+1.6
Cross sections and $D_n$	-0.003	+0.003
$\Lambda$	-0.003	+0.003
$\lambda_p$	-0.32	+0.35
$\beta$	+0.59	-0.56
$\lambda_d$	-0.15	+0.19
$f$	+0.17	-0.17

is consistently under the critical point to produce damages to the structures. After this ramp, the temperature starts decreasing due to outflow enthalpy stream.

The system reactivity starts from an assumed value of 285 pcm, it reaches criticality in about 1 second and then it goes toward more and more negative values. The simulation proves the intrinsic stability of the molten salt fuel thanks to highly negative temperature feedback coefficient. Furthermore, there is the negative contribution on reactivity of the salt lowering. The volume initially is larger than the critical configuration; as the draining starts, the reactivity insertion due to geometry gets lower and lower and goes toward greatly negative values.

From uncertainty analyses, it could be deduced a range of uncertainty for the temperature transient of about  $\pm 6\%$ .

The 0-D model manages to describe the general dynamics of variable transients and the main aspects of the phenomenon. Two main comments can be deduced from 0-D model results. Firstly, the transient can be divided into two parts: the first, characterized by the power production and consequent temperature ramp; the second dominated by the effect of outflow enthalpy. Secondly, the problem analysed is intrinsically dependent on spatial distributions of variables. Non-homogeneity in temperature affects the outflow temperature (and enthalpy) and indeed the energy balance itself. Same reasoning concerns also precursors' concentration. 0-D model needs information regarding spatially non-uniformity and such information has been given as analytical boundary condition for the energy equation derived from CFD simulations.

Concluding, to fully characterize the transient, a multi-dimensional model is required. For this reason, a preliminary 2-D approach is developed and described in the next chapter.

## Chapter 3

# Preliminary 2-D CFD-based multiphysics model for molten salt fuel draining

*From 0-D model results it is deduced that temperature transient during salt drainage could be split into two parts: one dominated by internal power production due to fissions and decay heat, followed by a second part affected by the outflow enthalpy due to salt stream exiting through the outlet section. The outflow enthalpy is strictly related to spatial distribution of temperature within the core. For instance, the location of the draining shaft affects the salt extraction and indeed its temperature.*

*It follows the need of multi-dimensional model to properly capture the spatial feature of the problem and hence the thermal dynamics of salt being drained.*

*Here a preliminary two-dimensional computational model, implemented on the open-source CFD code OpenFOAM, is developed and described. The physics employed is able to capture the fluid-dynamics of the drained salt (RANS equations along with realizable  $k-\epsilon$  turbulence model) and the energy governing equation coupled with neutronics (monoenergetic neutron diffusion and precursor balances).*

*The main concern of the study is, on one hand, to analyse the temperature time evolution during the drainage transient triggered by an accidental insertion of reactivity and investigate the possibility of hot spots, that could danger structural materials. On the other hand, subcriticality of salt domain should be granted; reactivity evolution of the salt multiplying system is thus studied, which is not only affected by high negative temperature feedback, but also by the moving boundary domain, which effects the neutron leakage probability. The adiabatic method is employed to compute and monitor the effective multiplication factor of the system for some selected transient snapshots. Finally the model results are shown and compared with the 0-D model solution.*

### 3.1 Introduction

Among the SAMOFAR objectives, it is mentioned the study and investigation of the draining of the fuel salt, as new fully-passive safety system. The liquid fuel can be drained out from the core and, driven by gravitation, displaced into a draining tank located underneath the main tank (see the EDS in section 1.2.2).

In the previous chapter, the fuel salt draining is studied developing a simplified zero-dimensional

semi-analytic mathematical model. The approach is able to capture the general dynamics of salt and the multiphysics of the phenomenon, consisting in the thermal-hydraulics and neutronics, strongly coupled by the volumetric heat generation and the temperature feedback. Two main conclusions could be deduced observing the 0-D model solution. Firstly, it is figured out that the temperature transient could be split into two parts. The first part is dominated by the power production within the system due to fissions and decay heat, which determines the temperature ramp and peak and lasts about 20 seconds. Instead during the second part, the transient tail, from the temperature peak to the total tank emptying, thermal power acquires a minor role in establishing the temperature time derivative and it is overcome by the contribution of the outflow molten salt enthalpy. In other words, the molten salt outflow is the dominant factor in the transient tail and it has a strong impact on temperature and precursor balances. The second conclusion, that could be deduced from 0-D model results, is that the draining transient entails an intrinsic dependence on spatial distribution of the variables. As an example, imagine a temperature distribution that follows the neutron profile in a finite cylinder (an axially cosine and a radially Bessel function of first kind and zero order): the temperature thus would be higher in the cylinder center and lower in the upper and bottom perimeters. If the draining pipe is located in the cylinder center, then it will be extracted a hotter molten salt than the situation in which the pipe is placed in the bottom corner. Therefore the location of the draining pipe determines the enthalpy outflow and indeed the temperature transient.

Spatial non-uniformity of variables is a key feature of the fuel salt draining phenomenon. From this statement the need of a multi-dimensional model, able to capture the variable distributions within the system.

A preliminary two-dimensional (2-D) axial-symmetric CFD-based numerical model is proposed and described in this chapter. The executable developed by the author is able to solve the Reynolds-Averaged Navier-Stokes (RANS) equations for the fluid-dynamics, closed with the *realizable k- $\epsilon$*  turbulence model, and the temperature transport equation, coupled with the neutron diffusion equation and the equations for precursor balances of neutrons and decay heat.

As far as the neutronics physics implementation, it is taken as reference the OpenFOAM model for the analysis of MSFRs proposed by Aufiero et al. at Politecnico di Milano [27]. The model is implemented on the open-source C++ OpenFOAM software [15].

Concluding, it is remarked here the main objective of the thesis, which is the MSFR safety assessment during an emergency core draining. Therefore the temperature spatial distributions are analysed during the whole transient in order to assess the possibility of damages to Nickel-based internal surfaces. Furthermore, reactivity of fuel is monitored to figure out whether subcriticality conditions are established during the drainage.

## 3.2 Problem setup and assumptions

The fuel salt draining is studied adopting the same simplified geometry described for the 0-D model (observe figure 3.1a), which dimensions are reported in table 2.1. Initially the cylinder is completely filled by molten salt. Then the salt starts being drained out through the bottom pipe driven by the gravitational force. The free surface level drops, leaving a space between it and the top surface. This space is hence filled by an inert gas. In the literature there is no explicit references to which type of gaseous substance is intended to be used in the frame of MSFR concepts, but it is supposed Helium or air. The only constraint about the filling gas concerns its temperature, that would be larger than the melting point of the binary fluorides' salt (table 1.1).

Therefore a two-phase solver is needed to model the fluid-dynamics of two immiscible fluids within the computational domain: the exiting salt and the entering air.

Table 3.1: Air thermo-physical properties. They refer to air at 700 °C and 1bar.

Mass density (kg/m <sup>3</sup> )	$\delta$	0.36
Isobaric specific heat (J/kg/K)	$c_p$	1136
Kinematic viscosity (Pa s)	$\mu$	$4.1 \times 10^{-5}$
Prandtl number (1)	Pr	0.71

It is assumed that the air is an incompressible fluid (low Mach number within the system) and its properties temperature-independent. The air properties used in the CFD simulations are listed in table 3.1 and refer to air at 700 °C and 1 bar.

As far as the molten salt properties are concerned, they refer to tables 1.2 and 1.3, to be consistent and to obtain comparable results with the 0-D model. The molten salt is indeed modelled as incompressible liquid with temperature-invariant properties.

In this preliminary CFD-based study of molten salt drainage, buoyancy and thermal expansion effects are not considered, since the salt mass density is kept constant. Future analyses will include temperature-dependent salt properties, which are a key objective in the research concerning MSFR feasibility and fuel salt safety assessment.

The reader must not forget that the molten salt is basically a liquid nuclear fuel and the salt volume consists in a multiplying system. Neutron flux and precursor equations have to be solved exclusively within the salt domain, which is changing in time as the salt is drained. The monoenergetic diffusion equation is adopted to model the neutron flux, which would be able to capture the dynamics of neutrons within the salt as both the temperature and the geometry change.

Balances of precursors, which include the free motion by advection and diffusion, are then solved to model their dynamics and the coupling with the flux.

Two-dimensionality, both of physics and geometry domain, is considered a suitable starting point to investigate the dynamics of the fuel draining and to capture the time evolutions of salt temperature and system reactivity, which are the main concern of the study. 2-D modelling approach means that the swirl caused by the poloidal component of velocity field is not considered. This latter quantity may be non-zero due to Coriolis force, could create vorticity in the system and its presence can contrast significantly buoyancy effects [28]. Future CFD simulations will be performed adopting a full three-dimensional geometry and physics, to capture the importance of these secondary phenomena.

### 3.2.1 Computational domain and mesh grid

As far as the geometry of the domain is concerned, it is kept that one of 0-D semi-analytical model described in section 2.2. The problem geometry consists in a cylinder, which reproduces the reactor core where the liquid fuel is contained. At the bottom, a long pipe is located to simulate the draining shaft, along which the salt flows during the drainage from the core to reach the draining tank. The tank is represented in figure 3.1a. Since axial-symmetry is assumed, the computational domain could be restricted to the red highlighted section.

Within the OpenFOAM environment, axial-symmetries are built starting from the 2-D plane that is wanted to mesh and then extruding poloidally of about 4°. It is obtained a narrow slice of the 3-D geometry, depicted in figure 3.1c, which represents the computational domain. OpenFOAM thus requires a single volume cell in the poloidal direction to force the equations being solved in a two-dimensional space. The mesh grid adopted for the spatial discretization in OpenFOAM is a fine quadrilateral structured grid. Structured grids allow for better space efficient, faster convergence and higher resolution with respect to unstructured grids [29]. A detail of the grid is shown in figure 3.1b.

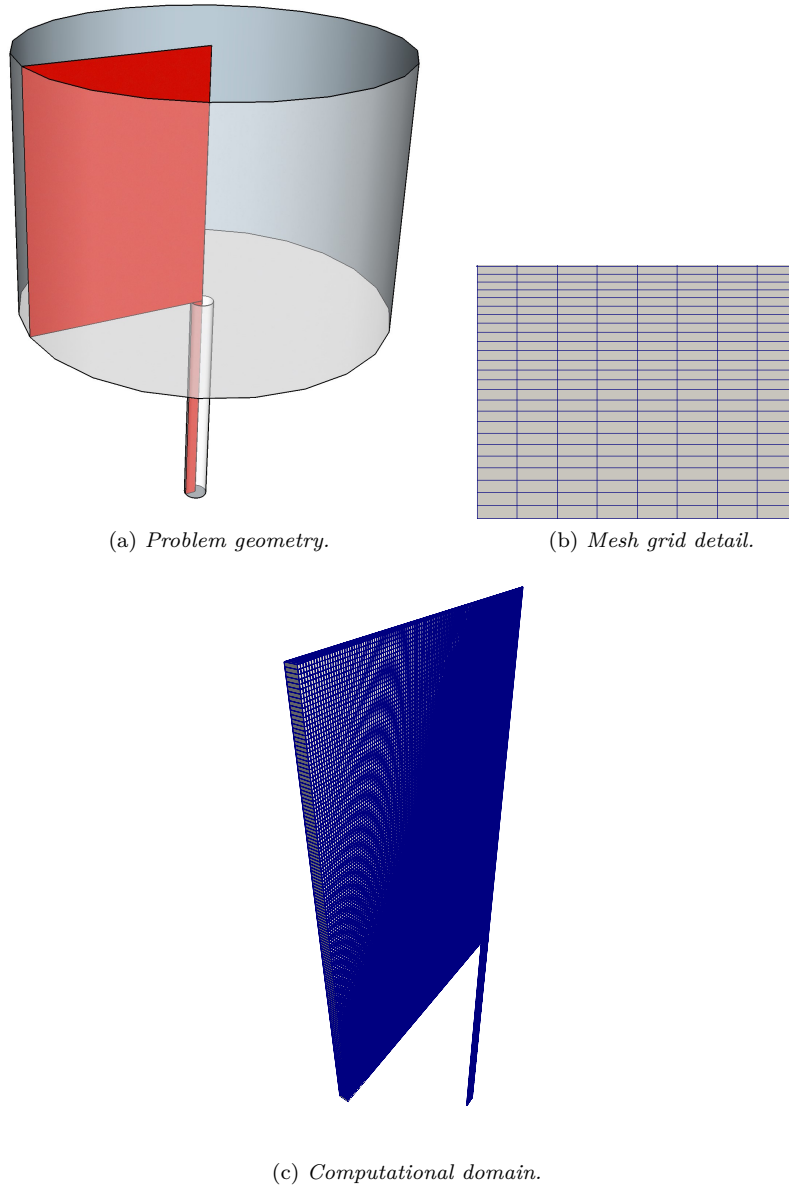


Figure 3.1: The top left figure depicts the geometry of the fuel salt draining. It is a simplified geometry consisting in a cylindrical tank and in a bottom pipe, which simulate respectively the reactor core and the draining shaft. 2-D axial-symmetric approximation allows to restrict the computational domain to the red section, which is then built in OpenFOAM (bottom figure) and meshed with quadrilateral cells. The top right shows a detail of the mesh grid.

The grid independence is ensured for the mesh grid adopted in this study.

### 3.3 OpenFOAM multiphysics modelling

The fuel salt draining problem necessitates the resolution, in the same time step, of partial differential equations of fluid-dynamics and energy (read: temperature) coupled with equations for neutron and precursor balances. A graphic scheme of problem multiphysics is depicted in figure 2.2. Furthermore, fluid-dynamics concerns a two-phase flow composed by the filling air and the liquid being drained. All the equations are discretized and solved within the open-source C++ OpenFOAM environment.

The two-phase Reynolds-Averaged Navier-Stokes (RANS) and energy equations are suitably modelled by the already-available OpenFOAM application *compressibleInterFoam*. This executable is then modified to include diffusion and precursor balance equations.

The section is organized as follows. At first, *compressibleInterFoam* application is described as the solver application which deals with fluid-dynamics and temperature physics. Consequently, the new executable, called *myCompInterFoam11*, is outlined in its equations implemented to capture the neutronics physics and the coupling between it and the temperature. Finally a description of the iteration scheme is reported, illustrating the strategy to couple the thermal-hydraulics with the neutronics physics, and a brief overview on the differentiating schemes is given.

#### 3.3.1 Fluid-dynamics and energy equations

As mentioned above, the fluid-dynamics and temperature equations are solved by the solver application *compressibleInterFoam*, available among the OpenFOAM libraries.

In the application description, it is reported that *compressibleInterFoam* is a “solver for 2 compressible, non-isothermal immiscible fluids using a VOF (Volume Of Fluid) phase-fraction based interface capturing approach” [15].

The choice of a compressible solver is due to allow future studies to include temperature dependencies of salt properties. Anyway, incompressibility and constant properties are assumed in this study.

The VOF method is based on the quantity  $\gamma$ , the volume fraction of a selected fluid over the total volume. If the grid cell is filled completely of fluid A, it acquires a value 1, otherwise it is 0 if the fluid B fully occupies it. At the interface between the two fluids, the volume fraction can assume a value in the range 0 to 1. The thermo-physical properties are computed in each volume cell as a weighted average on  $\gamma$  of fluid properties. Let us say  $\Psi$  a property (it could be the density, the kinematic viscosity and so on). The property associated to a certain volume cell is defined as follows

$$\Psi = \gamma_A \Psi_A + \gamma_B \Psi_B \quad (3.1)$$

where  $\Psi_A$  and  $\Psi_B$  are respectively the properties of fluid A and B and  $\gamma_A$  and  $\gamma_B$  the volume fractions, whose sum is 1 in every cell. Instead of use two different sets of governing equations for the two fluids, such defined properties are used in single set of equations for mass, momentum and energy throughout the whole domain.

The VOF method is computationally advantageous, as it uses one balance equation and hence less memory and computational time. Furthermore it is demonstrated to be suitable for fluids which present high immiscibility and high differences in fluid velocities.

The set of equations, RANS and temperature, solved by *compressibleInterFoam* is as follows:

- mass equation

$$\frac{\partial \delta}{\partial t} + \nabla \cdot (\delta \bar{U}) = 0 \quad (3.2)$$

where  $\delta$  is the mass density and  $\bar{U}$  the velocity vector;

- momentum equation

$$\frac{\partial}{\partial t}(\delta\bar{U}) + \nabla \cdot (\delta\bar{U}\bar{U}) = -\nabla p + \nabla \cdot \bar{\bar{\tau}} + \delta\bar{g} + \bar{F}_T \quad (3.3)$$

where  $p$  is the fluid static pressure,  $\bar{\bar{\tau}}$  the is the deviatoric stress two-order tensor (or Cauchy stress tensor),  $\bar{g}$  the gravitational acceleration and  $\bar{F}_T$  a force per unit volume related to interface surface tension;

- energy equation

$$\frac{\partial}{\partial t}(\delta c_v T) + \nabla \cdot (\delta\bar{U} c_v T) + \frac{\partial}{\partial t}(\delta K) + \nabla \cdot (\delta\bar{U} K) + p(\nabla \cdot \bar{U}) - \nabla \cdot (\tilde{k}_{eff} \nabla T) = 0 \quad (3.4)$$

with  $T$  the temperature,  $\tilde{k}_{eff}$  the effective (laminar plus turbulent) thermal conductivity,  $K$  the kinetic energy and  $c_v$  the specific heat at constant volume;

- volume fraction equation

$$\frac{\partial \gamma_{salt}}{\partial t} + \nabla \cdot (\gamma_{salt} \bar{U}) = 0, \quad (3.5)$$

where  $\gamma_{salt}$  is the volume fraction of salt.

The dependences on space and time of the above variables are omitted for the sake of clarity. As far as the RANS turbulence modelling, it is adopted the *realizable*  $k$ - $\epsilon$  model, with the standard wall function treatment [30]. It differs from the standard  $k$ - $\epsilon$  model for a new formulation for the turbulent viscosity and a new transport equation for the dissipation rate,  $\epsilon$ .

### 3.3.2 Neutronics equations

The neutron and precursor physics has to be added to the previous model and implemented in a new OpenFOAM application called *myCompInterFoam11*.

Neutron dynamics is modelled with the mono-energetic diffusion equation, taking into account the production of delayed neutrons from the single neutron precursor family. The diffusion equation must be solved exclusively within volume cells containing molten salt. It is assumed indeed that, within the cells filled by air, the neutron flux goes to zero. For this purpose, the diffusion equation is weighted on the salt volume fraction: if the molten salt volume fraction  $\gamma_{salt}$  is one (and simultaneously  $\gamma_{air}$  is zero), then flux is computed solving numerically the diffusion equation; otherwise the neutron flux is imposed to be null. The equation implemented in order to solve the diffusion only in salt volume cells is as follows

$$\gamma_{salt} \left( \frac{\partial}{\partial t} \left( \frac{1}{v} \Phi \right) - \nabla \cdot (D_n \nabla \Phi) + (\Sigma_a - (1 - \beta) \nu \Sigma_f) \Phi - \lambda_p C \right) + \gamma_{air} (\Sigma_a \Phi) = 0, \quad (3.6)$$

where the new quantity appearing is the mono-energetic neutron flux  $\Phi$ . The absorption cross section that multiplies the neutron flux in the last term exists just to keep dimensional consistency. The macroscopic cross sections are temperature dependent through logarithmic relations expressed

in equations (1.1).

The delayed neutron production is modelled through the differential balance of neutron precursor concentration  $C$ . One family of precursors is adopted, consistently with the 0-D semi-analytical model. The equation of precursors include the source term proportional to the neutron flux, the sink term related to decay events and the motion within the salt due to both advection and diffusion. This latter phenomenon is, though, of small effect with respect to velocity-transported phenomena. Furthermore, same considerations done for the neutron flux regarding where (in which cells) the precursor equation has to be solved are still valid. Then the neutron precursor equation is

$$\gamma_{salt} \left( \frac{\partial C}{\partial t} + \nabla \cdot (\bar{U}C) - \nabla \cdot (D_{eff} \nabla C) - \beta \nu \Sigma_f \Phi + \lambda_p C \right) + \gamma_{air} (\lambda_p C) = 0 \quad (3.7)$$

where  $D_{eff}$  is the effective diffusion coefficient, laminar plus turbulent terms, of precursor throughout the salt. The effective diffusion coefficient is computed as follows

$$D_{eff} = \frac{\nu}{Sc} + \frac{\nu_T}{Sc_T}, \quad (3.8)$$

where  $\nu$  and  $Sc$  are respectively the dynamic diffusivity of molten salt (table 1.2) and the Schmidt number. Subscript  $T$  refers to turbulent parameters. The Schmidt number can be seen as the analogue of Prandtl number: the first is related to diffusion of mass and atoms, the second to diffusion of heat. Information regarding motion of precursor atoms (i.e. fission products) within molten salts lack in the literature. In this study it is assumed values of 1 and 0.85 respectively for the Schmidt and the turbulent Schmidt numbers [27].

Analogously, concerning decay heat precursors, the implemented equation is as follows

$$\gamma_{salt} \left( \frac{\partial q_d}{\partial t} + \nabla \cdot (\bar{U}q_d) - \nabla \cdot (D_{eff} \nabla q_d) - f E_f \Sigma_f \Phi + \lambda_d q_d \right) + \gamma_{air} (\lambda_d q_d) = 0. \quad (3.9)$$

As far as the energy equation is concerned, it has to be modified to include the source of volumetric heat produced by fission events and decay heat. The instantaneous generation of heat from fissions corresponds to the term

$$P_{prompt} = (1 - f) E_f \Sigma_f \Phi, \quad (3.10)$$

whereas the delayed energy emission due to decay heat precursors is

$$P_{decay} = \lambda_d q_d. \quad (3.11)$$

Both the contributions are plugged in the energy equation (3.4) and multiplied times the salt volume fraction (no neutrons nor precursors exist within the air domain). The energy equation becomes

$$\frac{\partial}{\partial t} (\delta c_v T) + \nabla \cdot (\delta \bar{U} c_v T) + \frac{\partial}{\partial t} (\delta K) + \nabla \cdot (\delta \bar{U} K) + p (\nabla \cdot \bar{U}) - \nabla \cdot (\tilde{k}_{eff} \nabla T) - \gamma_{salt} (P_{prompt} + P_{decay}) = 0. \quad (3.12)$$

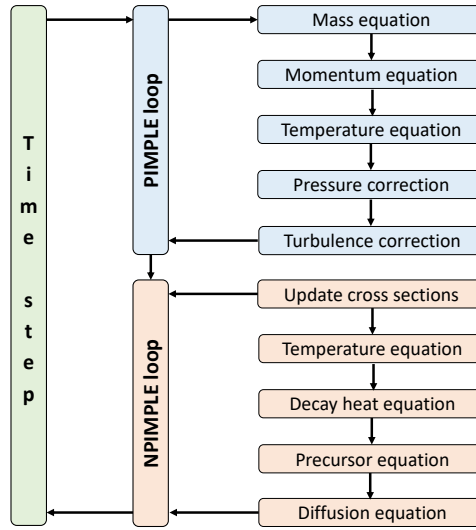


Figure 3.2: Iteration scheme adopted to solve the coupled equations for the fluid-dynamics and the neutronics.

### 3.3.3 Iteration scheme and equation differentiating patterns

Figure 3.2 shows the iteration scheme adopted to solve simultaneously, in the same time step, the coupled governing equations for fluid-dynamics, temperature and neutronics. PIMPLE (Pressure-Implicit Method for Pressure-Linked Equations) algorithm is already implemented into *compressibleInterFoam* application to solve iteratively the coupled equations for volume fraction, mass, momentum and temperature conservations (blocks in blue). Furthermore, in the same loop, corrections for pressure and turbulence effects are taken into account.

Within the same time step, a second separated PIMPLE loop, called NPIMPLE, is introduced to solve iteratively the governing equations for neutronics. First the nuclear parameters (cross sections and neutron diffusion coefficient) are updated according to the temperature spatial distribution. Then equations (3.6), (3.7) and (3.9) for respectively the neutron flux, the neutron precursor and the decay heat are solved iteratively along with (3.12) until an imposed convergence tolerance is reached.

In principle, since salt properties are dependent on temperature, a single iteration loop must be employed to solve all the coupled equations. In this particular case study, temperature-invariant thermal properties are assumed. Therefore it could be decoupled, within the same time step, iteration concerning the fluid-dynamic phenomena from the iteration solving the temperature-neutronics joint equations. The choice of two iteration loops in a time step implies a saving in terms of computational costs and time with respect to adopt a single PIMPLE loop.

As far as numerical schemes are concerned, OpenFOAM gives to the user the possibility to select a scheme for every differentiating and interpolating pattern appearing in the equations to be solved. It is imposed, for the time derivatives, a Euler first order implicit scheme. Gradient terms are instead all solved with central differencing Gaussian interpolation scheme, while an upwind scheme is used to discretize divergence operators. Laplacians are discretized instead with a linear interpolation scheme.

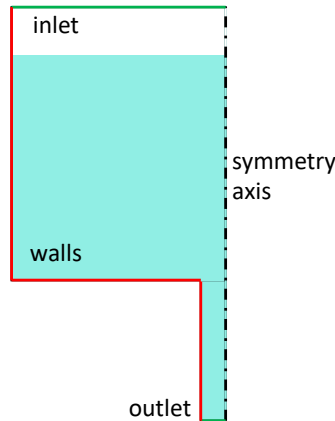


Figure 3.3: Boundaries of the CFD domain. Upper and lower green lines are respectively the inlet and the outlet boundaries. The dot-dash line is the cylinder symmetry axis, while the red lines correspond to wall surfaces.

## 3.4 Initial and boundary conditions

Boundary and initial conditions have to be imposed consistently in order to fully define the draining problem. Conditions of usual fluid-dynamic variables (pressure, velocity, temperature) must be treated, which are compounded by neutronic-related fields. A particular attention is dedicated to the inlet boundary, through which air enters in the domain with a specified pressure, but an undefined velocity field.

Finally, initial conditions are established to obtain as suitable as possible transient.

### 3.4.1 Boundary conditions

Boundary conditions (BCs) have to be imposed consistently to reproduce on one hand the salt draining phenomenon, mainly focusing on the pressure and velocity at the inlet top surface, and on the neutron flux and neutronic-related variables.

Boundaries of the CFD domain is depicted in figure 3.3: red borders represent the wall surfaces; upper and lower green lines correspond respectively to inlet and outlet boundaries; dot-dash vertical line is the symmetry axis.

As far as the salt volume fraction is concerned, inert gas enters during the transient from the inlet boundary. Therefore it is set a Dirichlet type boundary condition for  $\gamma_{salt}$  at the entrance, imposing the null value. Regarding the outlet, zero gradient is imposed to keep the field evolving and zero gradient is imposed at the walls which are impermeable boundaries.

The filling gas enters with a constant temperature along the transient, equal to 873 K. Dirichlet BC is thus applied for the temperature at the inlet, whereas homogeneous Neumann conditions are adopted for the walls and the outlet section.

As far as pressure and velocity fields are concerned, their boundary conditions are fundamental and have to be chosen consistently and jointly to model the gravity-driven drainage [31]. It is assumed that the gas enters with the atmospheric pressure (1 bar) and the same pressure is felt by the molten salt when it comes out from the outlet section. Therefore, at the outlet section, a fixed value (100000 Pa) is imposed as pressure BC, while null gradient is set for velocity. As far as the inlet section is concerned, a pressure value is specified there, which coincides with the entering gas

Table 3.2: Boundary conditions for the CFD simulations.

	Inlet	Outlet	Walls
Salt volume fraction	0	zeroGradient	zeroGradient
Temperature	873 K	zeroGradient	zeroGradient
Neutron flux	0	0	0
Decay heat precursors	0	zeroGradient	zeroGradient
Neutron precursors	0	zeroGradient	zeroGradient
Velocity	pressureInletOutletVelocity	zeroGradient	no slip
Pressure	totalPressure	fixedValue	zeroGradient

pressure, while the velocity field is undefined (usual heat transfer problems have a known velocity field and zero gradient for pressure for inlets). For these kinds of boundaries, the combination of `totalPressure` and `pressureInletOutletVelocity` respectively for pressure and velocity can be adopted. The first one is a Dirichlet type BC which specifies the fluid pressure given the value for the total pressure (static plus dynamic) by the user. Whereas `pressureInletOutletVelocity` imposes generally an homogeneous Neumann BC. The choice of this combination allows the velocity to acquire its own value and in the meanwhile avoids instabilities [15].

Finally boundaries for neutronics-related variables have to be specified. No precursors are entering through the inlet, whereas a null gradient is imposed for both the wall and the outlet sections.

As far as the flux of neutrons is concerned, vacuum boundary conditions are adopted. They suppose that no neutrons enter in the system from outside. Moreover the relative neutron flux gradient at the boundary is equal to  $-1/d$ , where  $d$  (the extrapolating length) is two times the diffusion coefficient  $D_n$ . The neutron flux goes to zero at the distance  $d$  far from the real boundary. Since the order of magnitude of  $d$  is centimeters, it is assumed here that the extrapolating lengths are negligible with respect to the tank dimensions and, thence, the flux is imposed to be zero at the all the real boundaries.

Table 3.2 sums up the BCs described above.

As far as turbulence variables are concerned, wall functions are applied as boundary conditions of both the turbulence kinetic energy and the rate of dissipation of turbulence energy. The  $y+$  parameter is kept in the range  $30 \div 300$  in every volume cells at the wall.

### 3.4.2 Initial conditions

To get the most suitable initial conditions for all the variables, one might run a simulation to model the steady-state conditions in a cylindrical-shaped molten salt reactor and then set the solution as the initial field distributions of the draining transient. This implies the development of new solver application, new CFD models and new OpenFOAM settings. This is out of the scope of the thesis. Furthermore, spatially uniform initial conditions are considered excessively unrepresentative of the problem. Therefore analytical or computational approaches are adopted to obtain suitable initial conditions for all the variables and are discussed here below.

The coordinates  $r$  and  $z$  that compare in this subsection refer to figure 3.4.

As far as the neutron flux is concerned, an analytical expression for the initial spatial configuration is available. It is imposed the steady-state solution for a finite homogeneous cylindrical multiplying system as follows

$$\Phi(r, z) = \Phi_0 J_0 \left( \frac{j_{01}}{R} r \right) \sin \left( \frac{\pi}{H} z \right), \quad (3.13)$$

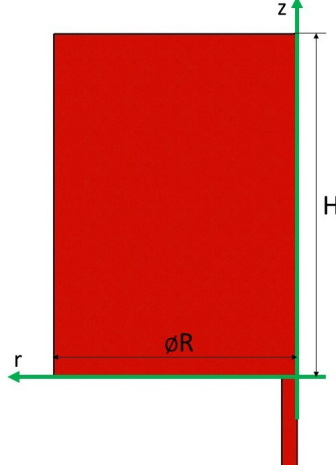


Figure 3.4: Coordinates  $r$  and  $z$  which define the reference system for initial conditions of neutron flux and precursors.

where  $R$  and  $H$  are the cylindrical tank dimensions which have been confounded with the extrapolated lengths.  $j_{01}$  is instead the first zero of the Bessel above and  $\Phi_0$  is the normalization coefficient. The last quantity is computed in order to get consistent initial value with respect to the 0-D model.

Analytical expressions are also derived for precursors, both of neutrons and decay heat. Consider the decay heat precursor balance, equation (3.9), computed within the salt volume cells and in steady-state conditions:

$$\nabla \cdot (\bar{U}q_d) - \nabla \cdot (D_{eff}\nabla q_d) - fE_f\Sigma_f\Phi + \lambda_d q_d = 0. \quad (3.14)$$

Diffusion can be neglected for precursors with respect to other terms in the balance. Furthermore it is assumed an upwards laminar velocity profile as follows

$$\bar{U} = (U_r, U_z) = \left( 0, 2U^* \left( 1 - \frac{r^2}{R^2} \right) \right), \quad (3.15)$$

where  $U_r$  and  $U_z$  are the velocity components and  $U^*$  is the average velocity over a cross section, that is computed knowing the nominal volumetric flow rate (table 1.1). Note that velocity has just one non-zero component which is dependent on  $r$ . Equation (3.14), plugging equations (3.15) and (3.13), becomes

$$\frac{\partial q_d}{\partial z} = -\frac{\lambda_d}{U_z} q_d + \frac{fE_f\Sigma_f\Phi_0}{U_z} J_0 \left( \frac{j_{01}}{R} r \right) \sin \left( \frac{\pi}{H} z \right). \quad (3.16)$$

Imposing at  $z = 0$  the boundary condition

$$q_d = (q_d)_0 \frac{U^*}{U_z} J_0 \left( \frac{j_{01}}{R} r \right), \quad (3.17)$$

the solution is

$$q_d(r, z) = \frac{1}{2(1 - r^2/R^2)} J_0 \left( \frac{j_{01}}{R} r \right) \left( ((q_d)_0 + A\pi) \exp \left( -\frac{\lambda_d}{U_z} z \right) + A \frac{H\lambda_d}{U_z} \sin \left( \frac{\pi}{H} z \right) - A\pi \cos \left( \frac{\pi}{H} z \right) \right), \quad (3.18)$$

where  $A$  is defined as

$$A = \frac{fE_f \Sigma_f \Phi_0 H}{U^* ((H\lambda_d/U_z)^2 + \pi^2)} \quad (3.19)$$

and  $(q_d)_0$  is the normalization parameter.

An analogous equation is derived for the neutron precursors

$$C(r, z) = \frac{1}{2(1 - r^2/R^2)} J_0 \left( \frac{j_{01}}{R} r \right) \left( ((C)_0 + E\pi) \exp \left( -\frac{\lambda_p}{U_z} z \right) + E \frac{H\lambda_p}{U_z} \sin \left( \frac{\pi}{H} z \right) - E\pi \cos \left( \frac{\pi}{H} z \right) \right), \quad (3.20)$$

where  $(C)_0$  is normalization factor and  $E$  is

$$E = \frac{\beta \nu \Sigma_f \Phi_0 H}{U^* ((H\lambda_p/U_z)^2 + \pi^2)}. \quad (3.21)$$

Regarding the temperature, the steady-state balance cannot be solved analytically, since the diffusion term cannot be simply canceled out. The initial temperature distribution is then computed numerically with an OpenFOAM application which solves the temperature equation imposing fission-related heat production (equation (3.13)) and upwards laminar velocity profile (equation (3.15)). The initial condition for the volume fraction is 1 everywhere in the domain, since at  $t = 0$  the tank is filled entirely by molten salt. While concerning the velocity field, it is imposed to be uniformly null in each cell, to avoid computational instabilities at the boundaries.

## 3.5 The adiabatic method

### 3.5.1 The iteration procedure

The system reactivity, together with the salt temperature, is the main concern of the study. The system reactivity evolution is monitored through the computation of the effective multiplication factor within the cylindrical multiplying system and adopting the power method, also known as the adiabatic method, iterative procedure [32, 33].

Consider the diffusion equation (3.6) solved within the molten salt domain and without the neutron precursor contribute:

$$\frac{\partial}{\partial t} \left( \frac{1}{v} \Phi \right) - \nabla \cdot (D_n \nabla \Phi) + (\Sigma_a - \nu \Sigma_f) \Phi = 0. \quad (3.22)$$

For any multiplying system, a steady-state critical condition exists by arbitrarily varying the amount of neutrons produced by fissions. Thus the time derivative goes away and the eigenvalue  $k$ , which represents the effective multiplication factor, appears as a factor that multiplies the fission term as follows

$$-\nabla \cdot (D_n \nabla \Phi) + \Sigma_a \Phi = \frac{1}{k} \nu \Sigma_f \Phi. \quad (3.23)$$

If the initial system presents an excess of neutron disappearances, either through absorptions or leakages, with respect to neutron production, then the  $k$  factor would be less than one to compensate this unbalance. The system is said subcritical. Otherwise, if the production overcomes absorptions and leakages the eigenvalue will be larger than one and the system is supercritical. If production and removal terms are perfectly balanced,  $k$  is 1 and the system is in a critical state. Consider now a generic mathematical model to describe the neutron dynamics within a multiplying system. Let us call  $\hat{L}^*$  the operator of neutron removal and  $\hat{F}^*$  the neutron production operator. No neutron at the initial state.

Consider now a pulsed source  $Q^{(1)}$  that is activated at  $t = 0$ . It produces the first generation of neutrons in the system as follows

$$\hat{L}\Phi^{(1)} = Q^{(1)}. \quad (3.24)$$

The fission operator applied to the first generation of neutrons produce the source for the second generation of neutrons  $Q^{(2)} = \hat{F}\Phi^{(1)}$ . The source then produces the neutron second generation

$$\hat{L}\Phi^{(2)} = Q^{(2)}, \quad (3.25)$$

and so on. For the  $n$ -th generation you have

$$\hat{L}\Phi^{(n)} = Q^{(n)} = \hat{F}\Phi^{(n-1)}. \quad (3.26)$$

It can be demonstrated that the fraction between two succeeding neutron generations, for  $n$  that goes to infinity, is a constant and coincides with the effective multiplication factor of the system considered:

$$\lim_{n \rightarrow \infty} \frac{\Phi^{(n)}}{\Phi^{(n-1)}} = k, \quad (3.27)$$

which yields

$$\hat{L}\Phi^{(n)} = \frac{1}{k} \hat{F}\Phi^{(n)}. \quad (3.28)$$

Therefore the adiabatic (or power) method gives an iterative procedure to compute the multiplication factor for any geometrical system and any mathematical model for neutrons' dynamics description.

Come back now to our diffusion equation and apply the adiabatic method just illustrated. The power method iterative procedure consists in the following steps:

- I) Guess the flux field  $\Phi^{(0)}$  and the effective multiplication factor  $k^{(0)}$  of the first iteration.
- II) Outer iteration

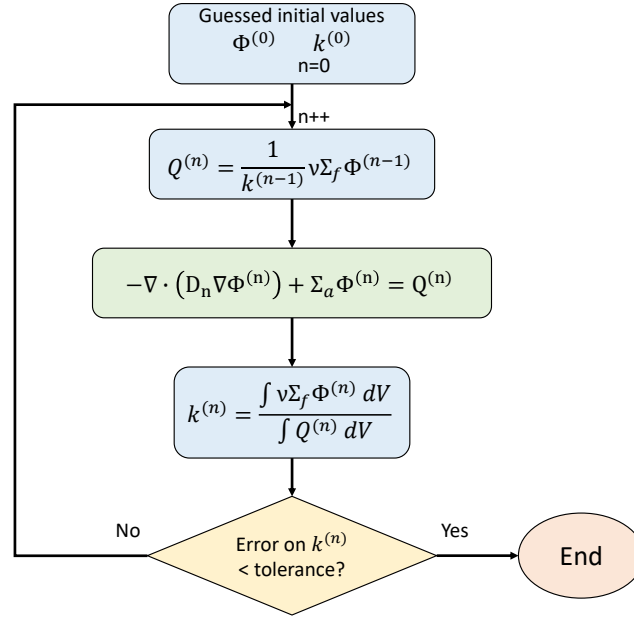


Figure 3.5: Adiabatic method iteration scheme. The green box represents the inner iterations to solve numerically the diffusion equation. The outer equation is instead highlighted by the feedback arrow at left.

1. Compute the neutron source according to the following expression

$$Q^{(n)} = \frac{1}{k^{(n-1)}} \nu \Sigma_f \Phi^{(n-1)} \quad (3.29)$$

2. Solve numerically the steady-state diffusion equation for the flux (inner iteration), where the source is specified

$$-\nabla \cdot (D_n \nabla \Phi^{(n)}) + \Sigma_a \Phi^{(n)} = Q^{(n)} \quad (3.30)$$

3. Compute the new effective multiplication factor

$$k^{(n)} = \frac{\int \nu \Sigma_f \Phi^{(n)} dV}{\int Q^{(n)} dV} = k^{(n-1)} \frac{\int \nu \Sigma_f \Phi^{(n)} dV}{\int \nu \Sigma_f \Phi^{(n-1)} dV} \quad (3.31)$$

4. Compute the error on the succeeding  $k$

$$error = \frac{|k^{(n)} - k^{(n-1)}|}{k^{(n)}} \quad (3.32)$$

III) End when a given tolerance is reached.

The difference between the power method used and the general description given above is that in computing the source  $Q^{(n)}$  the effective multiplication factor at the previous iteration is considered. The adiabatic method is sketched in figure 3.5.

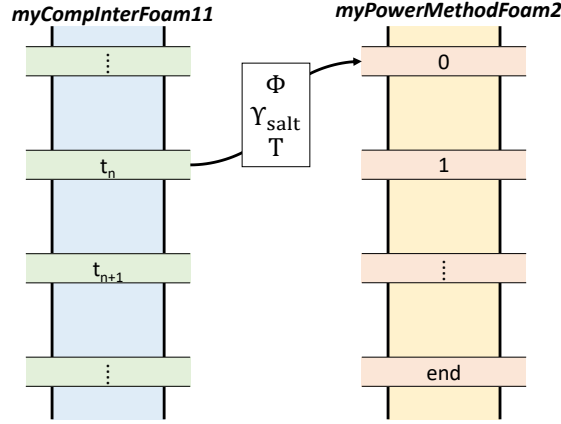


Figure 3.6: Joint between *myPowerMethodFoam2* and *myCompInterFoam11* solver applications. The neutron flux, the temperature and the salt volume fraction resulting from solving the draining transient are input to compute the multiplication factor at that time instant.

### 3.5.2 myPowerMethodFoam2

The power method iterative procedure described above is used to compute the actual effective multiplication factor of the molten salt domain at any time instant. The idea is to take a snapshot of the draining transient at a certain time and analyse it with an OpenFOAM application to run the power method and compute the effective multiplication factor at that time. Such application is called *myPowerMethodFoam2*.

Variables required to run the power method are the neutron flux, the temperature and the volume fraction of molten salt. Their spatial distributions are picked from the transient outcomes and passed as initial conditions for the adiabatic method iterations.

The salt volume fraction defines the configuration of the multiplying domain at a certain time. The domain is changing in time and it strongly affects the reactivity of the system. Therefore the diffusion equation (the inner iteration of the power method) has to be solved only in cells where molten salt is present. Equation (3.30) thus is implemented in *myPowerMethodFoam2* as follows

$$\gamma_{\text{salt}} \left( -\nabla \cdot (D_n \nabla \Phi^{(n)}) + \Sigma_a \Phi^{(n)} - Q^{(n)} \right) + (1 - \gamma_{\text{salt}}) \left( \Sigma_a \Phi^{(n)} \right) = 0, \quad (3.33)$$

where  $Q^{(n)}$  is computed as expressed in (3.29).

The temperature distribution is required to compute cross sections and diffusion coefficient all over the salt domain in order to take into account the negative reactivity feedback.

The neutron flux is not actually necessary to run the power method. Any initial guess for neutron flux is accepted. Anyway, a more suitable neutron flux distribution may speed up the iteration convergence.

The joint between *myPowerMethodFoam2* and *myCompInterFoam11* applications would be better comprehended observing figure 3.6. Spatial distributions of neutron flux, temperature and salt volume fraction are picked from a time instant of draining transient, which is the outcome of *myCompInterFoam11* simulation. They represent hence the initial conditions for *myPowerMethodFoam2* executable, which is launched to compute the multiplication factor  $k$  at that time instant.

## 3.6 Results

Once the initial and boundary conditions for all fields, the air and salt properties, the turbulence modelling, the iterations' parameters and the differentiating and interpolating schemes are set, the CFD simulation can be run launching the solver application *myCompInterFoam11*.

Results and plots are shown and discussed in this section. Variable spatial distributions are depicted for some time snapshots along the transient adopting the open-source application ParaView [34]. Moreover volume averages of fields are computed in order to compare 2-D CFD results with the 0-D semi-analytic transient solution, producing a benchmark.

A final comment regards the time instant to stop the transient. It is imposed 80 s, in order to not consider that part of transient excessively dependent on the outflow stream.

### 3.6.1 Volume and mass balances' verification

In the literature, some cases are attested in which two-phase *compressibleInterFoam* solver application fails in solving adequately the intergral mass balance within the domain. For this reason, a verification of both volume and mass balances is provided in this study, in order to prove the suitability of the CFD model.

At first, consider the volume balance. The system volume does not change in time, then its balance yields

$$\frac{dV}{dt} = \dot{V}_{in} - \dot{V}_{out} = 0, \quad (3.34)$$

where in the LHS there is the time derivative of the volume, which is zero since the domain volume does not vary, whereas in the RHS  $\dot{V}_{out}$  and  $\dot{V}_{in}$  are respectively the volume flow rates computed at the outlet and the inlet sections. Figure 3.7a shows the volume flow rates for the first 30 s of transient. The quantity  $\dot{V}_{in}$  is negative since it is computed as the surface integral of the scalar product of velocity field times the area vector, which is oriented outwards. Summing their absolute values yields approximately zero, confirming the volume balance.

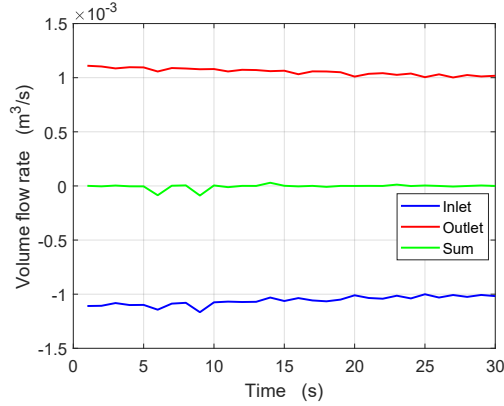
As far as the mass balance is concerned, its integral form is

$$\frac{dm}{dt} = \dot{m}_{in} - \dot{m}_{out}, \quad (3.35)$$

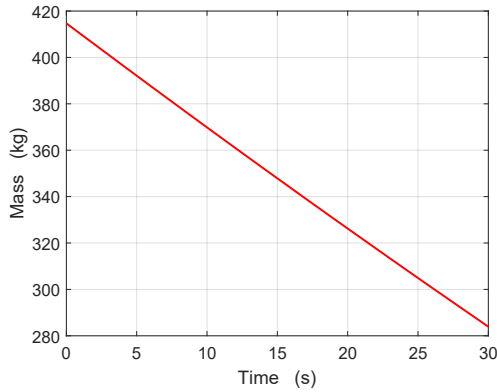
i.e. the mass variation in time (LHS) is equal to the unbalance of the mass flow rates computed at the inlet and outlet sections,  $\dot{m}_{out}$  and  $\dot{m}_{in}$ . Integrating both sides in time, you get

$$m(t) - m(0) = \int_0^t (\dot{m}_{in} - \dot{m}_{out}) dt, \quad (3.36)$$

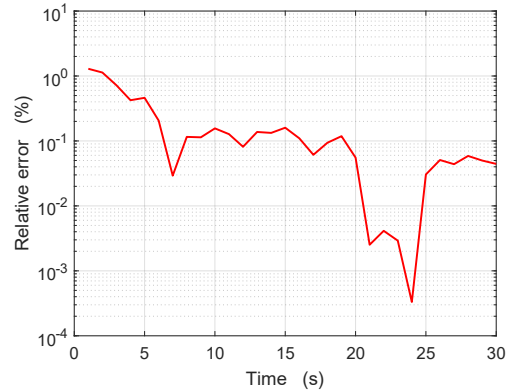
where  $m(t)$  is the mass content in the computational domain at time  $t$ , depicted in figure 3.7b, and  $m(0)$  is the respective initial value. Verifying the mass balance within the domain means ensuring that mass variations of both LHS and RHS of equation (3.36) are equal. Figure 3.7c shows the relative error between the two hand sides, which is around 0.1 %. It is deduced that the mass balance is suitably verified.



(a) Volume balance verification.



(b) Mass content in the system.



(c) Mass balance verification.

Figure 3.7: Volume balance (top graph) verification is represented as the sum of the absolute values of inlet and outlet volume flow rates. The bottom left plot shows the mass content in time and the bottom right plot depicts the relative error between RHS and LHS of equation (3.36), corroborating the mass balance verification.

### 3.6.2 The drainage dynamics

During the transient, the molten salt is drained and exits from the computational system through the outlet section. Before proceeding further with the results' description, the drainage phenomenon, from the hydraulics view point, is investigated and compared with the analytical model (section 2.3.4), in order to understand whether the physics is properly captured by the CFD simulations.

Figure 3.8 shows the molten salt level evolution in time. Blue line depicts the CFD simulation results, while in green it is plotted the salt level computed with the 0-D model where, specifically, the parameter  $\theta$ , that models friction and local losses of the salt within the system through equation (2.51), assumes the value of 0.785. The trend of a second-order polynomial, predicted by the analytical quasi-steady approach, is got by the CFD model, but a certain discrepancy is clearly noticeable. Such mismatch is due to higher friction and local losses in the CFD model, which are underestimated in the 0-D model. In fact, decreasing the  $\theta$  parameter by 10 % (which means increasing viscous dissipations), obtaining 0.710 (red line in figure 3.8), the CFD-based molten salt

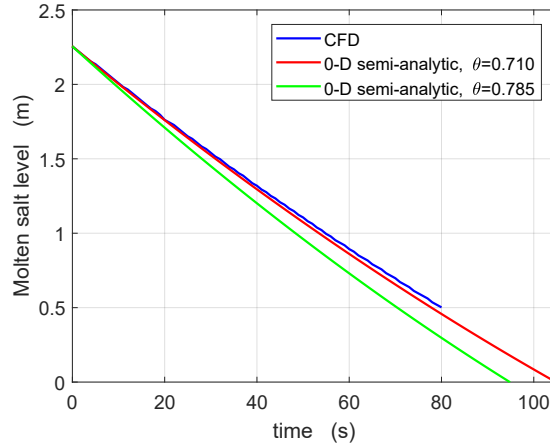


Figure 3.8: Molten salt level time evolution. In blue the CFD-computed salt level, while red and green lines represent 0-D model outcomes with respectively  $\theta=0.710$  and  $\theta=0.785$ .

Table 3.3: Comparison of total head losses due to friction and local dissipations between CFD simulation result and 0-D model with two values of parameter  $\theta$ . Values refer to  $t = 30$  s. The total head loss is computed within the salt domain, i.e. from the free surface to the outlet section.

	CFD	0-D semi-analytic	
		$\theta = 0.710$	$\theta = 0.785$
Total head loss (m)	1.723	1.747	1.326

level time evolution is perfectly matched by the analytical model.

For the sake of clarity, total head losses of the flowing molten salt at  $t = 30$  s are reported in table 3.3, showing a comparison between the CFD result and the 0-D model outcomes for the two values of  $\theta$  discussed above. The total head loss refers to salt flowing and it is computed as the difference between total head at the salt free surface and total head at the outlet section; it includes dissipations due to continuous friction along tank and pipe wall surfaces and due to local tank-pipe contraction. It is clear that  $\theta=0.785$  underestimates the dissipations due to local and continuous friction losses, giving a value of total head loss, computed with the relation (2.46), of 1.326 m. Conversely,  $\theta=0.710$  models more precisely the total pressure drop: a value of 1.747 m is found with the 0-D model, which is closer to the value derived from the CFD simulation (1.723 m). Pressure drops are discussed in details in the successive section.

Therefore,  $\theta$  equals to 0.710 is kept for succeeding comparisons between the 2-D CFD-based model and the 0-D semi-analytic one.

As far as the draining time is concerned, it is foreseen by the CFD simulation a period of about 105 s to empty completely the tank, which is in the range expected in the frame of preliminary considerations concerning the molten salt fuel draining [10].

Figure 3.9 shows the salt volume fraction spatial distribution for different time instants as results of the CFD computational simulation. Red domain corresponds to volume fractions equal to one and identify the molten salt, whereas the value zero is associated to filling air. White vertical lines represent the velocity streamlines across the domain: fluid enters from the top and falls down towards the bottom pipe.

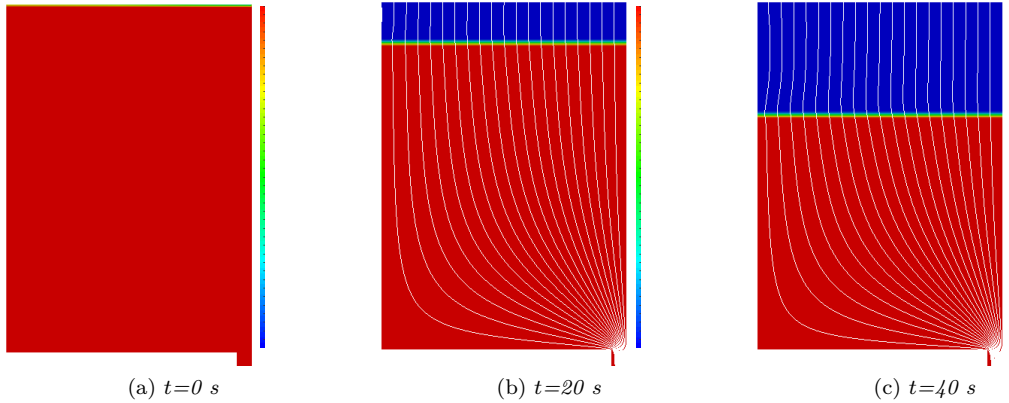


Figure 3.9: Salt volume fraction distributions in the domain for  $t$  equal to 0 (initial conditions), 20 and 40 s. Red domain corresponds to molten salt, while blue one represents the entering air. White lines constitutes velocity streamlines of fluids.

### 3.6.3 Fluid pressure and mechanical energy

The mechanical energy content of a moving fluid (i.e. flow energy apart from its internal energy content) is composed by three terms, as declared in the Bernoulli's trinomial: the pressure, the potential and the dynamic (or velocity) term [35]. The first two terms constitute the static pressure. In terms of meters, it yields

$$z + \frac{p}{\delta g} + \frac{U^2}{2g} = H, \quad (3.37)$$

where the terms are respectively the potential head, the pressure head, the velocity head and the total head. The latter expresses the total amount of mechanical energy possessed by a flowing fluid. Reductions of the fluid total head corresponds to energy dissipations due to continuous friction and local losses.

Observe figure 3.10a. It reports the elevation of molten salt ( $z$  coordinate, where the reference zero is the outlet section) in the ordinates, while in the abscissa the heads in meters. The plot shows the situation of molten salt at a certain time instant of the transient ( $t = 30$  s), where the free surface is 3.5 m far from the outlet section. Therefore, it is not reported the pressure conditions of air filling the space from the free surface to the inlet section. Furthermore, the quantities depicted here are averaged over cross sections. In other words, terms have been averaged on the plane  $x$ - $y$  and then plotted against the  $z$  coordinate:  $z=0$  corresponds to the outlet section; from 0 to 2 m there is the draining pipe; at  $z=2$  m it is located the tank-pipe contraction;  $z=3.5$  corresponds to the molten salt free surface;  $z=4.255$  m coincides with the inlet section.

The red line represents the potential head and, obviously, it is a straight line starting from  $z=0$ . The velocity of molten salt is almost constant in the cylinder tank thanks to incompressibility and assumes values around 0.03 m/s. The corresponding velocity head (blue line) is plotted in blue and it is negligible with respect the other terms within the cylindrical tank. The green line is the pressure head. It increases since the fluid potential energy gets lower. Losses due to continuous friction are negligible within the tank and hence the total head, which is the summation of the three terms above and it is plotted in cyan, keeps constant.

At  $z=2$  m the cross section area suddenly shrinks due to contraction from the cylinder tank to the bottom pipe. The velocity head jumps to higher values since, keeping constant the flow rate

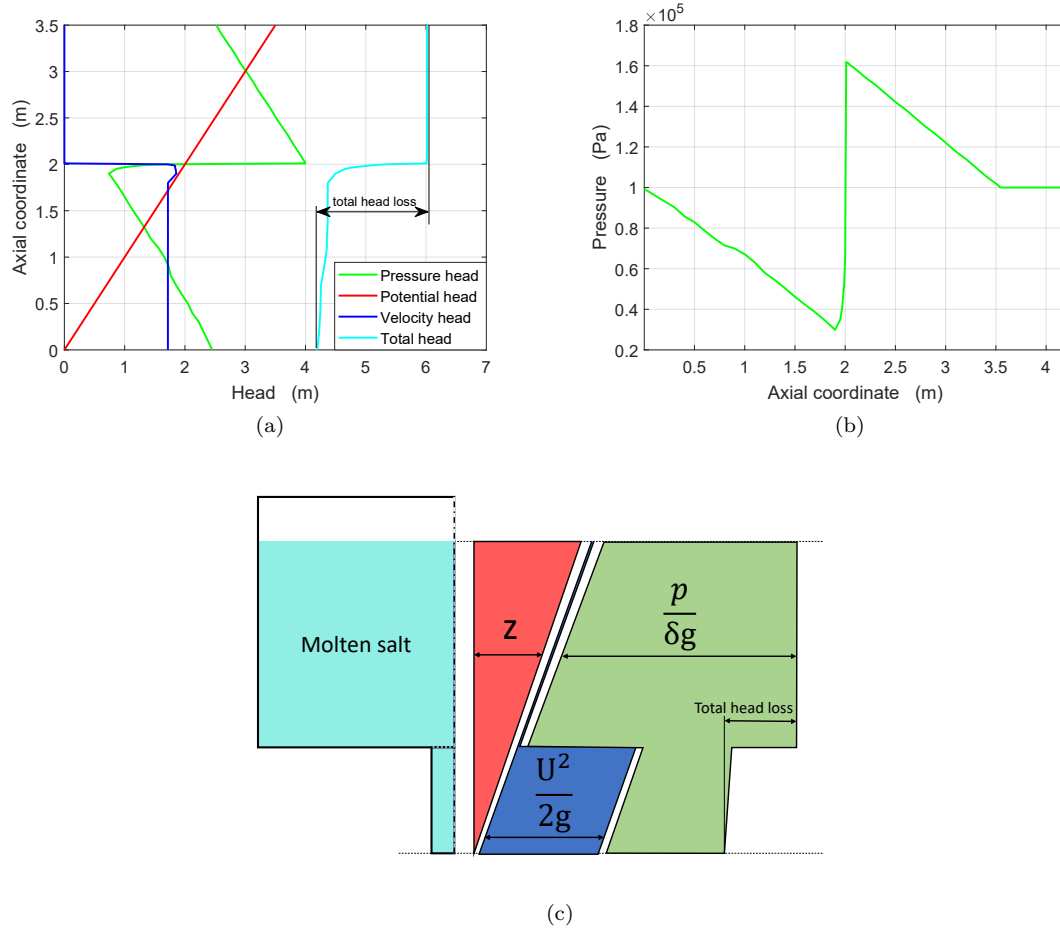


Figure 3.10: Pressure and mechanical energy of flowing salt axial profiles at  $t = 30$  s. Figure (a) shows the Bernoulli's trinomial, in terms of meters, on the abscissa where on the y-axis it is plotted the elevation. Green, red and blue lines are respectively the pressure, the potential and the velocity heads and their summation gives the total head in cyan. The head lines along the tank is represented in figure (c), which has an horizontal orientation. Figure (b) depicts the fluid pressure as a function of the axial coordinate.

and reducing the flow area, velocity increases to about 5.8 m/s. The contraction implies a local dissipation of energy and indeed a local loss in the total head term. In turn the pressure head abruptly goes down, but then increases along the pipe due to reduction in the potential head. The velocity head is almost constant again (incompressibility), while the total head slightly reduces due to continuous friction.

Figure 3.10c shows a graphical scheme of what is discussed above, regarding pressure, potential and velocity heads lines along the salt domain. The hydraulic and energy lines are depicted horizontally, not vertically as in the conventional schemes. The summation of the three terms gives the total head or energy line of the fluid [35].

Figure 3.10b, instead, shows the pressure axial profile, from the inlet to the outlet sections. The pressure at the inlet section acquires its boundary value of 1 bar, that is kept constant for the

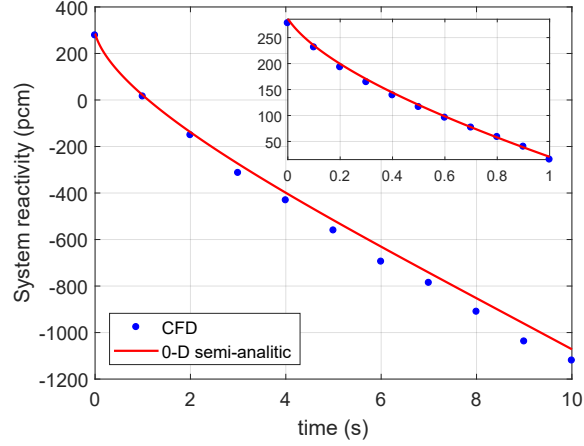


Figure 3.11: System reactivity time evolution. Blue dots and red line correspond respectively to CFD-based and 0-D semi-analytic results. A further zoom on the first second is depicted.

whole transient. The increase of the pressure within the air domain (from  $z=3.5$  to  $z=4.255$  m) is negligible since the potential energy reduction is small (small mass density of air). Within the molten salt, pressure increases to compensate the potential energy loss, then it suddenly drops due to tank-pipe contraction and kinetic energy jump and consequently increases up to 1 bar again at the outlet.

### 3.6.4 System reactivity

System reactivity is monitored during the draining transient launching the power method solver application, *myPowerMethodFoam2*, for a set of selected snapshots, as explained in section 3.5. Actually, the solver returns the effective multiplication factor  $k$  at a certain time instant. The reactivity of the system,  $\rho$ , at that time is then derived as follows:

$$\rho = \frac{k - 1}{k}. \quad (3.38)$$

Figure 3.11 shows the system reactivity time evolution. Blue dots represent the results of the adiabatic method applied to selected time instants of the transient, while the red line corresponds to 0-D semi-analytic model solution. Moreover, a zoom on the first second is reported.

The CFD-derived reactivity starts from a positive initial value of 277.7 pcm, that corresponds to a reactivity insertion of 0.83 \$. Such amount of initial reactivity causes a sharp increase in neutrons population (figure 3.14). Consequently, the reactivity decreases as the temperature rises and the salt volume reduces. In fact, the multiplying system feels a negative insertion of reactivity due to twofold phenomena: strong negative temperature feedback related to temperature-dependent cross sections; reduction of volume domain and resultant increase of neutron leakage probability. The two phenomena are captured by the CFD numerical model and the obtained results match consistently with those from the 0-D semi-analytic model.

Both the two model foresees the system criticality being reached at about 1.1 s. After this time instant, the system acquires more and more negative values, confirming the intrinsic stability of molten salt fuels.

A final comment regards the nature of the two reactivities here compared, the semi-analytic-based and the CFD-based ones. As far as the first reactivity is concerned, in the semi-analytic model the reactivity is somehow imposed to the mathematical model. In other words, both the geometry-related and the temperature-related reactivities, equations (2.34) and (2.35), are expressed through a-priori-known analytic relations. On the other side, the CFD-based reactivity results from the system evolution, i.e. it is computed a posteriori, through the power method on a transient snapshot.

The fact that the two reactivities match so perfectly gives indications about the validity and consistency of the two models. Specifically the 0-D model gives analytical expressions as functions of temperature and domain height, that are suitable in predicting the reactivity trend in a volume-changing multiplying system.

### 3.6.5 Neutron flux

It is well understood that the molten salt represents a multiplying domain in which the monoenergetic diffusion equation is solved and a flux distribution computed. It is further highlighted, in expression (3.6), the mathematical strategy to get the diffusion solved solely within the molten salt phase.

Figures 3.12a and 3.12b show the neutron flux distributions in the system at  $t = 1 \times 10^{-5}$  s, basically at the transient onset, for two, an horizontal and a vertical, selected lines within the domain. The flux axial profile is reported in figure 3.12a: the abscissa represents the  $z$  coordinate (vertical line), while  $r$  is kept fixed to 0.1 m from the cylinder axis. Coordinates  $z$  and  $r$  refer to figure 3.4. The flux matches perfectly a cosine for the entire tank, since at the beginning the salt fills completely it. A Bessel function of first kind and zero order is instead clearly consistent with the CFD-computed radial shape of the flux (figure 3.12b) along a horizontal line ( $z=3.1$  m).

As the salt is drained, the multiplying domain changes and so do the volume cells where diffusion have to be solved. The mathematical strategy to weight the diffusion equation on the salt volume fraction, equation (3.6), works greatly: the flux assumes its axial-cosine and radial-Bessel profile exclusively where the molten salt is present in the domain, while in the volume cells occupied by air it is null. Figures 3.12c and 3.12d show the neutron flux axial profiles respectively at  $t = 10$  s and  $t = 20$  s. As the molten salt is drained and air enters in the system, the flux adjusts to occupy the volume-changing multiplying domain consistently with the diffusion equation solution. Furthermore, one can notice that the flux magnitude is decreasing in time, due to both the action of temperature feedback and volume-dependent increasing leakages.

It could be concluded that the CFD numerical model is able to capture the moving boundary domain and furthermore to take into account the leakage increase due to volume shortening.

Figure 3.13 depicts the flux spatial profile within the system. It is highlighted, once again, the suitability of the computational model in solving the neutron diffusion exclusively in volume cells filled by fuel salt. As the fuel salt is drained and the volume reduces, the neutron flux follows consistently the new multiplying domain.

Finally, a comparison between the 2-D computational model and the 0-D semi-analytic model is employed. Figure 3.14 reports the transient of the neutron flux for the early 0.14 s. For the CFD model, a volume-averaged value for the neutron flux is computed in order to compare it with the 0-D results. The graph shows a higher prompt jump for the 0-D model flux with respect to the CFD one. This is anyway consistent with the system reactivity results presented at the previous subsection, since initial reactivity for the 0-D model is slightly larger than the 2-D computational one. However, it is supposed that the one-group point kinetics model overestimates the neutron production with respect to the result obtaining from CFD simulation. The larger production of neutrons, consequently, has significant effects on the transient evolutions of other variables, such

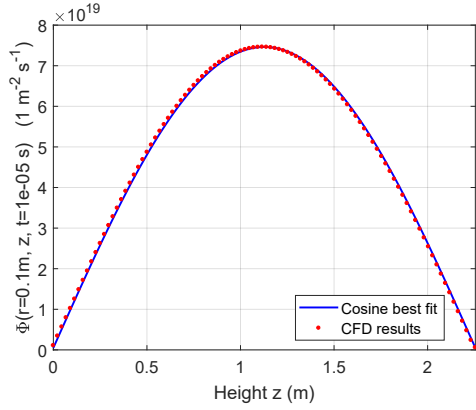
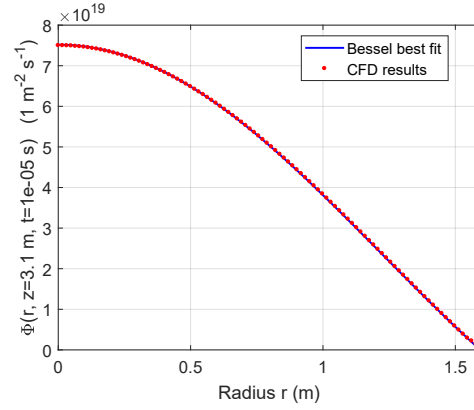
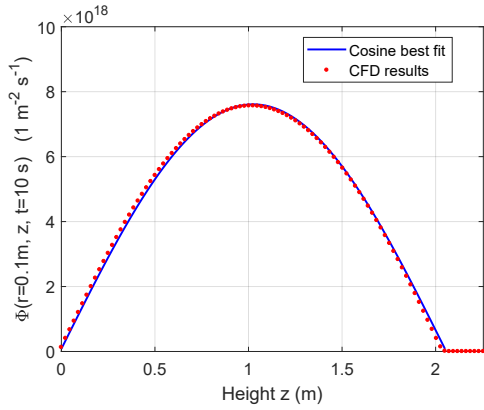
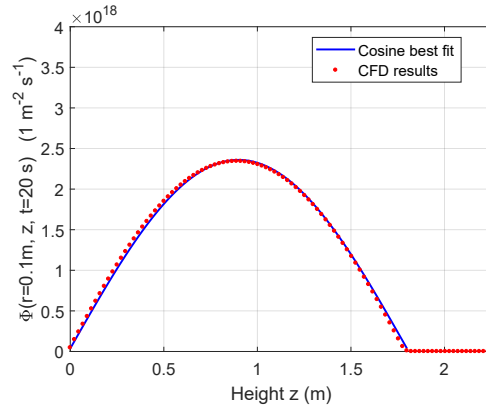
(a) Axial flux profile at  $t = 1 \times 10^{-5}$  s,  $r=0.1$  m(b) Radial flux profile at  $t = 1 \times 10^{-5}$  s,  $z=3.1$  m(c) Axial flux profile at  $t = 10$  s,  $r=0.1$  m(d) Axial flux profile at  $t = 20$  s,  $r=0.1$  m

Figure 3.12: In figures (a), (c) and (d) neutron flux axial profiles is plotted at the transient onset and at  $t$  equal to 10 and 20 s. Figure (b) shows the initial neutron flux radial profile. Red dots refer to results obtained from CFD simulations, while blue lines represent analytical best fits.

as the precursors and the temperature. It will discuss later on about the transients of such quantities.

### 3.6.6 Precursors of neutrons and decay heat

Precursor, both of neutrons and decay heat, time evolutions are plotted in figure 3.15, where they are also compared with the results obtained from the 0-D semi-analytic model. CFD-based precursors' transients follow the trends of the semi-analytic solution: both precursor concentrations slightly increase during the first seconds of transient due to the large neutron production; subsequently they decay exponentially with their respective decay constant. Incidentally, the higher neutron production resulted in the 0-D model causes the greater production of both neutron and decay heat precursor concentrations with respect to the CFD solution.

Precursor distributions within the system for some time instants are plotted in figure 3.16. Two phenomena can easily be appreciated. Firstly, the highest values, both for precursors of delayed

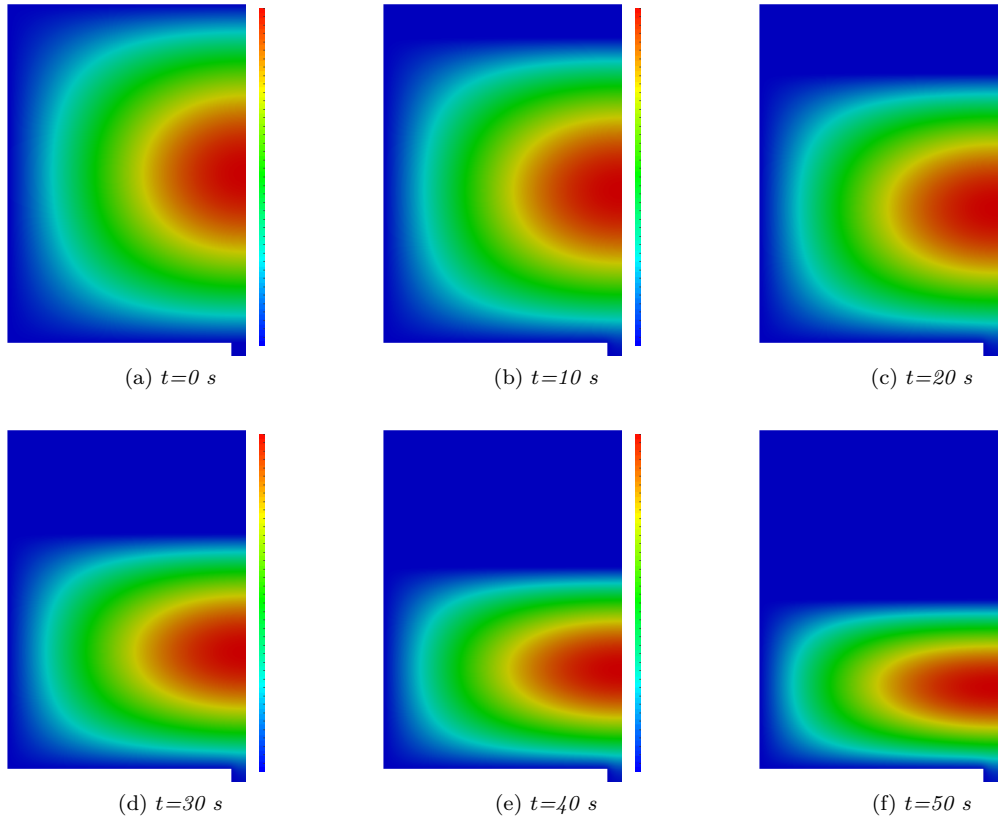


Figure 3.13: Neutron flux spatial distributions for some time snapshots.

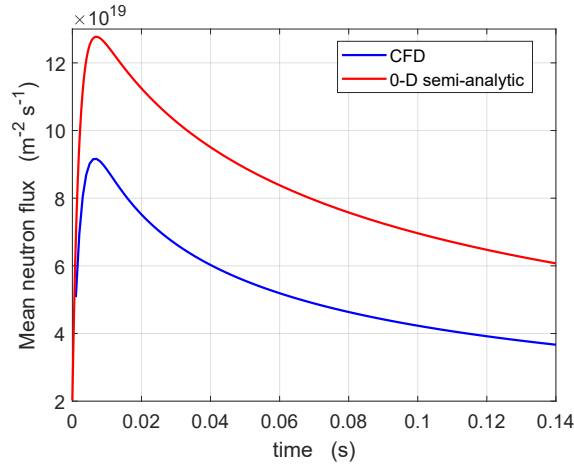


Figure 3.14: Neutron flux time evolution for the early 0.14 s. Blue and red lines are respectively the results of the CFD simulation and the 0-D semi-analytic model.

neutrons and decay heat, are located in the cylinder center, since neutron flux concentrates there.

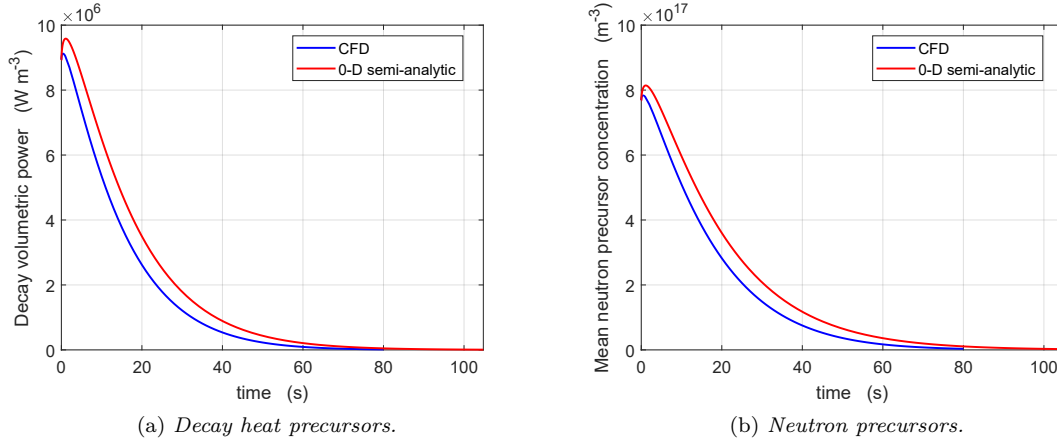


Figure 3.15: Average precursor concentrations of decay heat and neutrons are respectively depicted in left and right figures.

Secondly, the advection dominates the motion over diffusion: precursors are transported by the bulk motion of salt towards the bottom pipe. This is confirmed by the high values of Péclet numbers (advective-to-diffusive transport rate ratio) for precursors moving in the salt. As far as computational resolution of equations (3.7) and (3.9) is concerned, precursor balances are correctly solved solely within the salt domain, while in the space occupied by air they are properly set to zero.

### 3.6.7 Molten salt temperature

Figure 3.17 shows the temperature spatial distributions within the cylindrical tank for three selected snapshots. Air enters from the top at a temperature of 873 K and this value is averagely kept within the space above the salt free surface (no source of heat is present within the air domain). The temperature reaches the highest values in the cylinder center, where heat production is concentrated. Moreover temperature, as precursors' motion, is transported by the fluid streamlines and simultaneously diffuses in the salt medium.

The temperature time evolution is compared against the 0-D semi-analytic model in figure 3.18. A mean temperature, representative of the entire molten salt, is computed as the average weighted on the salt volume fraction (in order to take into account solely the salt domain) over the vertical coordinate of the bulk temperature computed on a cross section  $S(z)$ :

$$\langle T \rangle = \frac{\int_0^H \left( \int_{S(z)} T \bar{U} \cdot d\bar{S} \right) \gamma_{salt} dz}{\int_0^H \left( \int_{S(z)} \bar{U} \cdot d\bar{S} \right) \gamma_{salt} dz}. \quad (3.39)$$

The initial temperature ramp has a steeper slope for the 0-D model than CFD-based results. This is due to the larger heat production foreseen by the semi-analytic calculations. Consequently, after reaching the peak, the temperature decreases almost linearly with the same inclination. Globally, the temperature dynamics resulting CFD simulations shows a delay in time of about 5 s with respect to the semi-analytic model.

As far as safety of structural materials is concerned, the critical point to weak damages to core

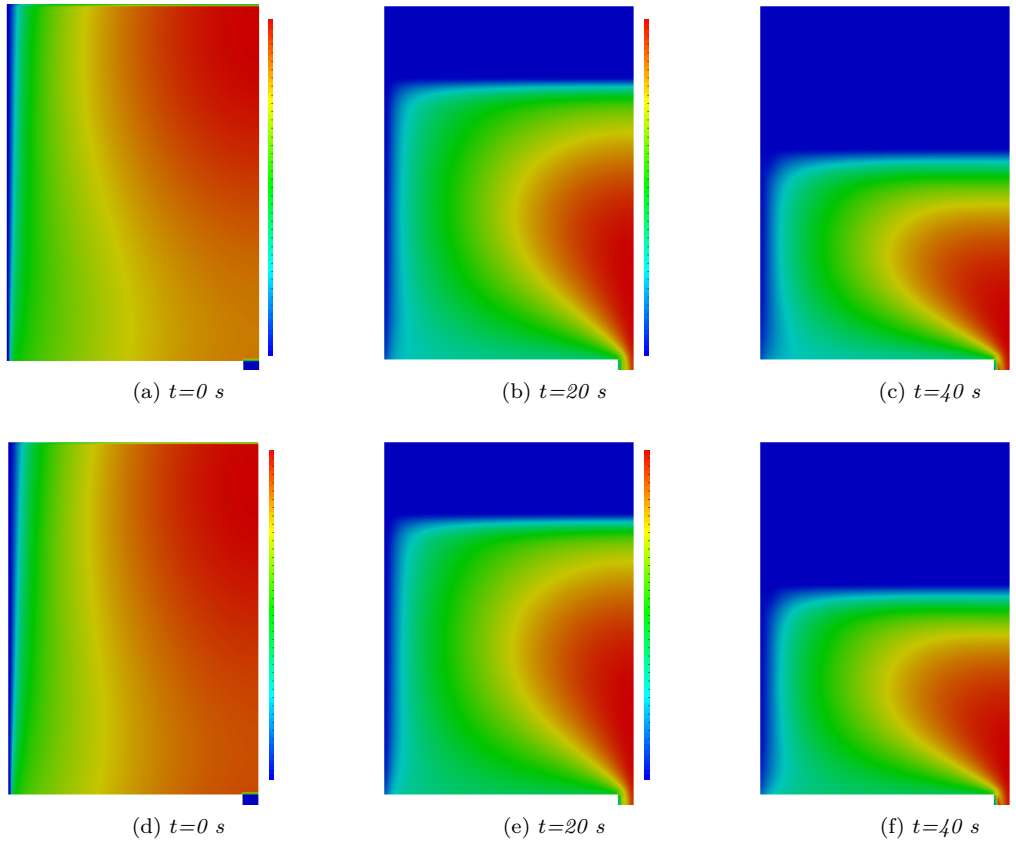


Figure 3.16: The three top figures show the decay heat precursor distributions for  $t=0$ , 20 and 40 s. Figures (d), (e) and (f) depicts neutron precursor distributions for the same time instants.

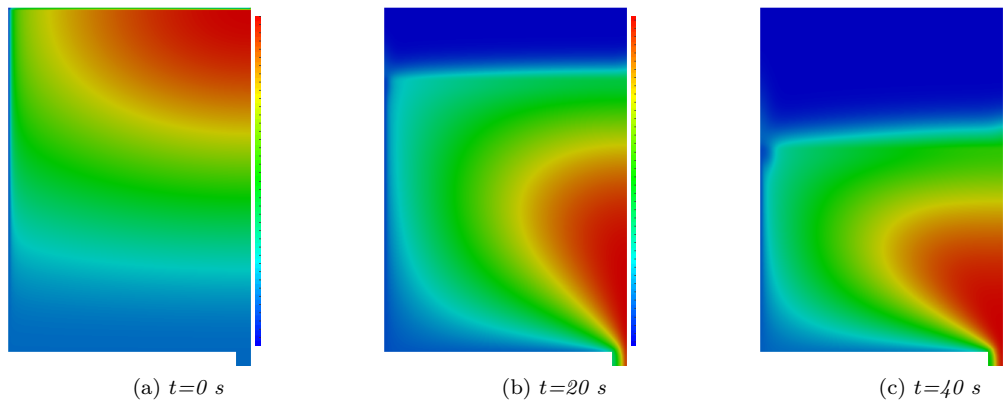


Figure 3.17: Temperature spatial distributions for  $t$  equal to 0, 20 and 40 s.

internal surfaces is about 1300 °C (~1600 K) [11]. The safety margin is largely maintained nearby the walls. Moreover, the temperature peak, located in the core center, is kept below that threshold

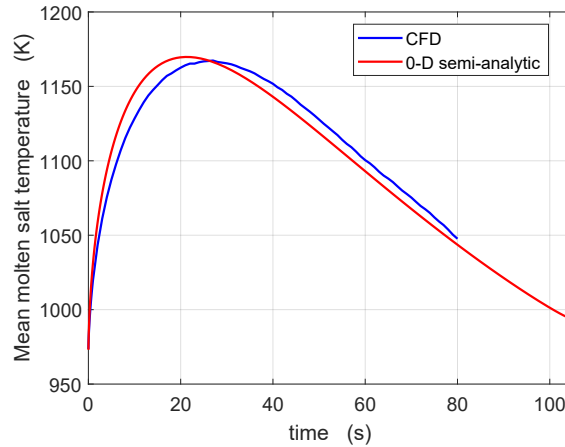


Figure 3.18: Mean temperature of molten salt versus time. Blue and red lines are respectively the CFD and the 0-D model results.

for the whole transient.

Some troubles could occur along the draining shaft (bottom pipe) during an emergency draining. The fuel still continues to produce heat internally while it flows along the bottom pipe, to be discharged then into the draining tank underneath the core. The thermal-hydraulics problem of a fluid flowing in channels and featured by an internal heat generation could be characterized by significant differences concerning heat transfer mechanisms with respect to conventional fluid problems. Therefore, to not underestimate the temperature of walls, and indeed the thermal load on surfaces, appropriate correlations for the Nusselt number must be used. This problem will be faced in the next chapter.

### 3.7 Concluding remarks

The fuel salt draining is featured by the relevance of spatial distributions of fields, such as temperature and precursor concentrations. The intensity of variables extracted at the outlet section influences the respective balances significantly during a great part of the whole transient, from about 20 s to the end. Therefore a multi-dimensional model is needed to truly characterize the phenomenon.

In this study, a preliminary computational model is developed. It consists in a two-dimensional numerical model implemented on the open-source CFD code OpenFOAM. The fluid-dynamics is modelled with RANS equations, where the turbulence effects are captured with *realizable k- $\epsilon$*  model. The temperature transport equation includes the thermal power generation resulting from prompt fission production and decay heat. As far as neutronics is concerned, monoenergetic diffusion and precursor balances, which include fluid motion due to advection and diffusion, are finally implemented in the model physics.

Nuclear properties are temperature dependent, in order to model the broadening Doppler effects within the fuel. Conversely, regarding thermo-physical properties of the salt, in this preliminary study they are kept constant with the temperature. Therefore, density-related effects, such as buoyancy and thermal expansion of salt, are not considered and will be faced in future studies.

The main concern of the problem is to analyse the temperature transient in the scenario studied.

Initial system reactivity of about 280 pcm implies a maximum mean temperature increase of about 200 K, while a maximum local hot spot of 1450 K. It follows that, from the point of view of safety, internal surfaces would not be damaged in this foreseen scenario. As far as the draining shaft is concerned, safety assessment will be faced in the next chapter, applying the correlation for internally heated fluids flowing in circular ducts.

Furthermore, the reactivity analysis confirms the intrinsic stability of molten salt fuels to variations of temperature. 0.85 \$ of initial insertion are totally absorbed within 1 second thanks to high negative temperature feedback. Subcriticality conditions are thus granted all along the transient. In particular, the system reactivity evolution shows good agreement with the 0-D model outcomes, where the expression of reactivity are derived from analytical considerations regarding temperature and geometry variations.

The study presented in this chapter would represent a preliminary simplified analysis of the draining of fuel salt, in the frame of EDS concept. Future studies will remove some approximations and improve the physics of the model. Improvements will concern the energy multi-group neutron flux and more families of precursors, both of neutrons and decay heat. Thermo-dynamics of the salt will be improved implementing the analytical relations for salt properties in table 1.2: mass density and viscosity are key parameters regarding molten salt fluid-dynamics. Specifically, temperature-dependent density allows for the analysis of buoyancy and thermal expansion effects.

Finally, the toroidal-shaped geometry of MSFR concept, developed in the frame of SAMOFAR European project, might be adopted.

Nevertheless, the computational model developed in the frame of this thesis manages to capture the salt drainage phenomenon, the temperature transient and the evolution of system reactivity, giving suitable results for the purposes and concerns posed in this preliminary study and attesting the safety conditions during the emergency core draining.

## Chapter 4

# Heat Transfer Coefficient for internally heated fluids

*Molten Salt Fast Reactors are selected reactor concepts in the frame of Generation IV nuclear reactors. They feature liquid fuels, which represent the main innovative solution and bring several benefits, primarily concerning the reactor safety. Furthermore, apart from core-related safety aspects, liquid fuels are a concern of MSFR out-of-core components, such as pipes, heat exchanger tubes and the draining shaft. The heat transfer mechanism of a fluid flowing in circular ducts featured by an internal heat generation (in this case from fissions and decay heat) is significantly different with respect to conventional thermal-hydraulic problems. This has strong implications on the wall-bulk temperature difference and indeed on the wall surface thermal loads. This problem is indeed a concern regarding the safety assessment of the fuel flowing along the draining shaft in the frame of molten salt draining.*

*Correlations regarding the heat transfer coefficient of internally heated fluids flowing in ducts lack in the literature, aside from analytical studies by Fiorina et al. (C. Fiorina, A. Cammi, L. Luzzi, K. Mikityuk, H. Ninokata, M. E. Ricotti, 2013) and Poppendiek (H. F. Poppendiek, 1954).*

*In this study a CFD-based computational model is developed in order to analyse internally heated fluid heat transfer mechanism. Firstly the analytical results by Fiorina and Poppendiek are compared with the computational ones, producing a benchmark between the present and the Fiorina's studies. Then an improved correlation is developed based on CFD numerical outcomes.*

*The CFD model is implemented on open-source C++ OpenFOAM v4.1 software.*

*Ultimately, the correlation is applied to the molten salt fuel flowing within the draining shaft, as a conclusion of the safety assessment of fuel emergency draining.*

### 4.1 The need of a new correlation

The last chapter is dedicated to the analysis of internally heated fluids flowing in circular channels. Flows featuring an internal heat source are of interest of several industrial fields. These flows are employed not only in nuclear sector, but also in the field of chemical reactors, in which chemical reactions among reagents are often exothermic. As examples, it is cited the combustion as a common exothermic reaction and a type of chemical reactor, the Plug Flow Reactor, where the reagents stream along a pipe.

Molten salt fuels represent fluids with an internal generation of heat, produced by fissions and decay chain events, and flowing, apart from the core, along pipes, heat exchanger tubes, draining

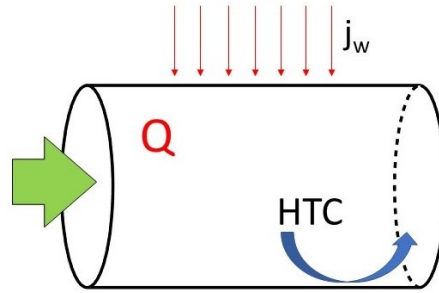


Figure 4.1: The goal: computing the HTC for a fluid subjected to both external heat flux and internal heat generation flowing in circular ducts.

shaft and so on. Therefore the study of the thermal-hydraulic of such flows is a concern of the safety characteristics of molten salt reactors and, specifically, of the draining shaft in the frame of molten salt fuel draining.

The heat transfer mechanism of such fluids are completely different with respect to conventional thermal problem in which fluids are subjected to only the external heat flux; internal generations of heat may produce higher wall-bulk temperature differences. Hence, in order to foresee the wall temperature and indeed the surface thermal load, it is really important to analyse and predict the Heat Transfer Coefficient (HTC) for internally heated fluids flowing in pipings and channels (figure 4.1). Correlations for the Nusselt number for circular duct flows characterized by both an external wall heat flux and an internal heat generation lack in the current literature, except for the study by Fiorina et al. [9] and other past researches. In [9] the idea is to use the available and various correlations for the Nusselt number without a heat source and correct them with a factor that takes into account this flow feature. Hence the aim is to develop a correlation for the corrective factor aforementioned as a function of the traditional dimensionless numbers that characterize the whole thermal-hydraulic problem.

Firstly a brief overview of the approach adopted by Fiorina et al. for turbulent flows and their results are reported, which is based on a fully analytical study. Then the same problem is faced with numerical CFD simulations. Therefore Fiorina's analytical results are compared against the computational ones, producing a benchmark. In the second part, simulations are performed in order to obtain an improved CFD-based estimation of the corrective factor correlation for the turbulent flow regime.

Finally, the developed correlation is applied to the case study of the molten salt flowing within the draining shaft in the frame of emergency fuel draining.

The numerical simulations are performed using the CFD open source software OpenFOAM v4.1 [8].

## 4.2 Analytical analysis by Fiorina et al.

The problem of a fluid subjected to both external heat fluxes and internal heat generation has been faced analytically since 1954. In that year a study was published by Poppendiek [36], which analysed the case of fluids flowing in circular ducts in the laminar regime. In 2014, at Politecnico di Milano, Fiorina et al. investigated the same problem in the turbulent flow regime: a brief overview of the model and results is reported below.

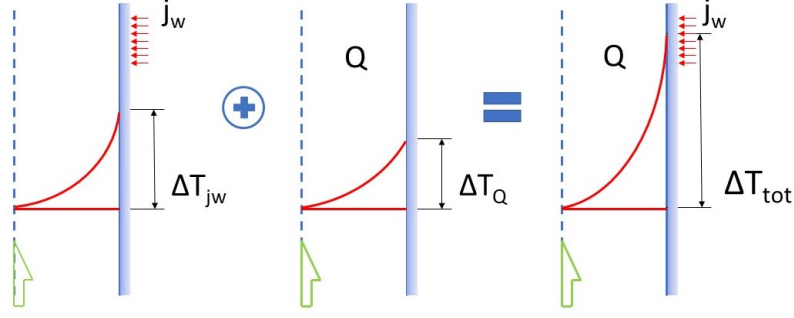


Figure 4.2: Graphic representation of the superposition of external wall heat flux  $j_w$  (left) and internal heat generation  $Q$  (center) to give the overall solution  $tot$  (right).  $\Delta T$  represents the wall-bulk temperature difference.

The research of the Nusselt number as a function of the thermal and hydrodynamic parameters is based on the analytical model developed by Di Marcello, Cammi and Luzzi [37]. The assumptions adopted are axial-symmetry geometry configuration and physics, steady-state conditions, incompressible fluid and constant thermo-physical properties, negligible natural convection and buoyancy force, hydro-dynamically and thermally developed flow, uniform internal heat generation and uniform heat flux at the wall, negligible axial conduction and no components of time-averaged velocity in the radial direction. The energy equation under the previous hypotheses becomes

$$u \frac{\partial T(r, z)}{\partial z} = \frac{1}{r} \frac{\partial}{\partial r} \left( r \left( \frac{\nu}{Pr} + \frac{\nu_t}{Pr_t} \right) \frac{\partial T(r, z)}{\partial r} \right) + \frac{Q(r, z)}{\delta c_p}, \quad (4.1)$$

where  $u$  is the (only) velocity component in the stream direction,  $r$  and  $z$  the cylindrical coordinates,  $T(r, z)$  the temperature,  $Q(r, z)$  the volumetric heat source ( $\text{W}/\text{m}^3$ ),  $\nu$  the kinematic viscosity,  $Pr$  the adimensional Prandtl number. Quantities with the subscript  $t$  refer to turbulence effects. Taking advantage of the linearity feature of the thermal problem, the overall solution could be written as the superposition of the solution linked to the external heat flux imposed on the wall (identified by the subscript  $j_w$ ) and the other due to the internal generation of heat (identified by  $Q$ ). The reader can observe figure 4.2 for the graphic scheme, while the mathematical relation for this approach is:

$$(T_w - T_b)_{tot} = (T_w - T_b)_{j_w} + (T_w - T_b)_Q. \quad (4.2)$$

Generally an heat transfer coefficient is defined as the wall heat flux to the wall-bulk temperature difference ratio. Therefore including this definition into equation (4.2) yields

$$h_{tot} = \frac{1}{1/h_Q + 1/h_{j_w}} \quad (4.3)$$

where the single HTC's are

$$\begin{aligned} h_{j_w} &= \frac{j_w}{(T_w - T_b)_{j_w}}, \\ h_Q &= \frac{j_w}{(T_w - T_b)_Q}. \end{aligned} \quad (4.4)$$

The  $h_Q$  is not exactly a HTC since no heat flux is imposed on the wall in the internal source situation.

From equation (4.3), an expression for the total Nusselt number can be derived:

$$Nu_{tot} = \frac{h_{tot} 2R}{\tilde{k}} = \frac{1}{1/h_Q + 1/h_{j_w}} \frac{2R}{\tilde{k}} = \frac{1}{\tilde{k}/2R/h_Q + \tilde{k}/2R/h_{j_w}} = \frac{1}{1/Nu_Q + 1/Nu_{j_w}}, \quad (4.5)$$

where  $2R$  is the tube diameter and  $\tilde{k}$  the thermal conductivity. Gathering the term  $1/Nu_{j_w}$  at denominator, equation (4.5) becomes

$$Nu_{tot} = \frac{Nu_{j_w}}{1 + \frac{Nu_{j_w}}{Nu_Q}}. \quad (4.6)$$

Equation (4.6) allows computing the Nusselt number for the whole thermal situation starting from the traditional and well-studied Nusselt number for fluids under an imposed heat flux and correcting it with the factor  $\zeta$ , that depends on the Prandtl and Reynolds numbers and on the thermal load  $QD/j_w$ , where  $D$  is the channel diameter:

$$\zeta(QD/j_w, Pr, Re) = \left(1 + \frac{Nu_{j_w}}{Nu_Q}\right)^{-1} = (1 + \sigma(QD/j_w, Pr, Re))^{-1}, \quad (4.7)$$

and thus equation (4.6) is written as follows

$$Nu_{tot}(QD/j_w, Pr, Re) = \zeta(QD/j_w, Pr, Re) Nu_{j_w}(Pr, Re). \quad (4.8)$$

For the sake of clarity, it is made explicit the dependencies: the conventional Nusselt  $Nu_{j_w}$  depends only on  $Pr$  and  $Re$ , as it is well established; whereas both  $Nu_{tot}$  and  $\zeta$  are functions of  $QD/j_w$  ratio too. Furthermore, in  $\sigma(QD/j_w, Pr, Re)$  the dependency on  $Pr$  and  $Re$  can be separated from the dependency on  $QD/j_w$  defining the quantity  $\varphi(Pr, Re)$  as follows [bib:Fiorina]:

$$\sigma(QD/j_w, Pr, Re) = \frac{QD}{j_w} \varphi(Pr, Re). \quad (4.9)$$

Combining equations (4.8) and (4.9) yields

$$\varphi(Pr, Re) = \frac{j_w}{QD} \left( \frac{Nu_{j_w}}{Nu_{tot}} - 1 \right). \quad (4.10)$$

In a compact and clearer formulation, the total Nusselt number is obtained as follows

$$Nu_{tot}(QD/j_w, Pr, Re) = \frac{1}{1 + \frac{QD}{j_w} \varphi(Pr, Re)} Nu_{j_w}(Pr, Re). \quad (4.11)$$

It can be assumed that  $\varphi(Pr, Re)$  is a typical function of the type  $aPr^b Re^c$ . A best fit analysis with the results coming from [37] gives the following formula:

$$\varphi(Pr, Re) = 1.656 Pr^{-0.4} Re^{-0.5}. \quad (4.12)$$

The equation above is valid in the turbulent range of Reynolds numbers. In the laminar flow regime  $\varphi(Pr, Re)=3/44$  is proposed by Poppendiek [36].

### 4.3 Numerical CFD-based analysis

The thermal-hydraulic problem of a fluid flowing in a circular duct subjected to external heat flux and internal heat generation is now faced numerically and computationally with the open source CFD code OpenFOAM v4.1 [8]. CFD analysis allows to obtain improved and more suitable results, removing some assumptions adopted in the analytical model that will be discussed later.

At first, numerical results are compared with the analytical ones, producing a benchmark of the activity by Fiorina et al. for flows in the turbulent regime and of Poppendiek's results for laminar flows. Subsequently an improved CFD-based correlation is proposed for the corrective factor  $\varphi(Pr, Re)$  in the turbulent regime.

#### 4.3.1 The CFD model and domain

The problem of a molten salt flowing in a channel subjected to an external heat flux and an internal homogeneous heat source is analysed computationally, both in the turbulent and in the laminar regimes. Some assumptions are adopted in solving it:

- 2D axial-symmetry geometry;
- steady-state conditions;
- constant thermo-physical properties and fluid incompressibility;
- negligible natural convection and buoyancy;
- uniform internal generation of heat and uniform heat flux at the wall.

The OpenFOAM application used is *buoyantBoussinesqSimpleFoam* for the turbulent regime simulations. It is a steady-state solver for buoyant, turbulent flow of incompressible fluids. Buoyancy is neglected.

As far as the laminar fluid flow simulations are concerned, *icoFoam* (a transient solver for incompressible, laminar flow of Newtonian fluids) is used, modified to include the temperature equation. The equations implemented and solved are as follows:

$$\begin{aligned}\nabla \cdot \bar{U} &= 0, \\ \nabla \cdot (\bar{U}\bar{U}) - \nabla \cdot ((\nu + \nu_t) (\nabla \bar{U} + (\nabla \bar{U})^t)) &= -\nabla p, \\ \nabla \cdot (\bar{U} T) - \nabla \cdot \left( \left( \frac{\nu}{Pr} + \frac{\nu_t}{Pr_t} \right) \nabla T \right) &= Q_T,\end{aligned}\tag{4.13}$$

where  $\bar{U}$  is the velocity vector,  $p$  the pressure,  $T$  the fluid temperature and  $Q_T$  the source term. The latter quantity,  $Q_T$ , is actually a temperature rate (Kelvin per second). Therefore, knowing the value of volumetric heat generation ( $Q$ ,  $W/m^3$ ) to be imposed, the temperature source can be computed accordingly to the following relation:

$$Q_T = \frac{Q}{\delta c_p},\tag{4.14}$$

Table 4.1: Thermo-physical properties of the Lithium-Thorium Fluoride binary salt.

Kinematic viscosity	$2.46 \times 10^{-6}$	$\text{m}^2/\text{s}$
Prandtl number	20	1
Mass density	4125	$\text{kg}/\text{m}^3$
Thermal conductivity	1.01	$\text{W}/\text{m}/\text{K}$

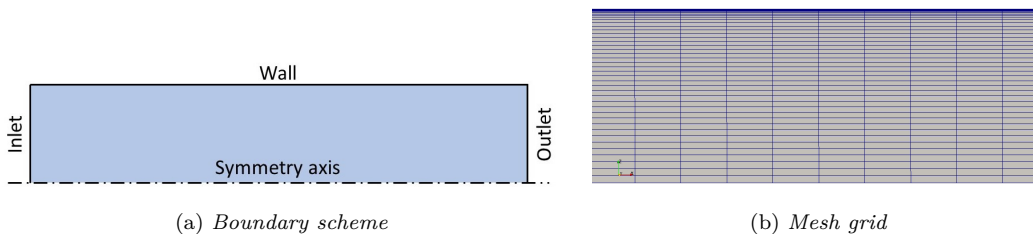


Figure 4.3: Boundaries for the computational domain, represented by a 2D axial slice of the channel (top graph). The length ensures the thermal-hydraulic development of the fluid flow. A section of the channel is reported in figure (b) to show the mesh grid.

where  $\delta$  is the mass density and  $c_p$  the isobaric specific heat. Such formulation of source term is required by the OpenFOAM applications used.

The gravitational force is not considered in the model.

The reader can appreciate the difference between the above equation for the temperature and equation (4.1). The conduction is now solved both axially and radially and no velocity component is arbitrarily set to zero.

The thermo-physical properties used refer to a  $\text{LiF-ThF}_4$  (78-22 mol%) molten salt [1], computed at  $700\text{ }^\circ\text{C}$ . The properties are reported in table 4.1. In particular, the value for kinematic viscosity is higher with respect to common liquids and has significant implications on fluid-dynamics of streaming molten salts.

As far as the turbulence is concerned, the choice of the turbulence modelling is a crucial issue since it has a strong impact on the wall temperature and indeed on the Nusselt number.  $k-\epsilon$  class of turbulence models is selected, since the problem studied is the traditional fluid flow in circular channel. A low-Reynolds turbulence approach in the wall cell is used and a value of  $y^+$  less than one near the wall is reached. Launder and Sharma low-Reynolds RANS  $k-\epsilon$  turbulence model is adopted, with a very fine grid up to the wall [38].

The computational domain, figure 4.3, is represented by a 2-D axial slice of the cylindrical channel. The length is set forty times the channel diameter to ensure the thermal and hydraulic development of the fluid flow. The boundary conditions for the pressure, temperature and velocity are reported in table 4.2. Symmetry boundaries are imposed for the symmetry axis. Furthermore as boundary condition for the temperature at the external wall, it is imposed a temperature gradient. The value for the temperature gradient is derived from the wall heat flux  $j_w$  just dividing it times the thermal conductivity  $\tilde{k}$ .

A grid independent solution is ensured for the mesh grid used (Fig. 4.3b).

Table 4.2: Boundary conditions imposed.

	Pressure	Temperature	Velocity
Wall	Zero-gradient	Fixed gradient	No slip
Inlet	Zero-gradient	Fixed value	Fixed value
Outlet	Zero	Zero-gradient	Zero-gradient

### Validation of the CFD model

Before proceeding further with the study, the reliability and the suitability of the CFD numerical model hereby described has to be investigated and ensured.

Firstly the analytical mass and energy balances,

$$j_w 2R\pi L + QR^2\pi L = \dot{m} c_p (T_{out} - T_{in}), \quad (4.15)$$

are verified for each CFD simulation.  $\dot{m}$  is the mass flow rate and  $T_{out}$  and  $T_{in}$  are respectively the bulk temperatures at the outlet and the inlet sections.  $T_{out}$  is derived from equation (4.15) and compared with the CFD outcome. It is found that the energy balance is respected, showing errors between the analytical and the computational results in the order of cents of Kelvin.

Furthermore, results from simulations with only the external heat flux (conventional heat transfer problem) are compared with the Dittus-Boelter and the Gnielinski correlations for the Nusselt number. The Dittus-Boelter and the Gnielinski equations have been confirmed experimentally and are valid for the thermo-hydraulic conditions used in this paper [21].

Results are shown in figure 4.4. The computed Nusselt numbers are consistent with the Gnielinski's correlation for every Reynolds numbers investigated.

It can be concluded that the CFD model is perfectly suitable and reliable for the conventional (only external heat flux) thermo-hydraulic problems and its suitability is extended also for the total (external heat flux plus internal heat generation) problem.

## 4.4 Comparison between analytical and CFD-based corrective factors

The correlation for  $\varphi(Pr, Re)$  developed by Fiorina et al. (equation (4.12), [9]) is compared with the values obtained from the numerical simulations solved with OpenFOAM. CFD results are obtained as described below.

Each CFD run is identified by four setup quantities:

- the fluid Prandtl number;
- the inlet velocity, that defines the Reynolds number together with the channel diameter and the kinematic viscosity (table 4.1);
- the heat generation within the fluid  $Q$ ;
- the external heat flux at the wall  $j_w$ .

In turn a run includes two CFD simulations, one with both the internal heat generation and the external wall heat flux to get the total Nusselt number  $Nu_{tot}$  and the second one with only  $j_w$

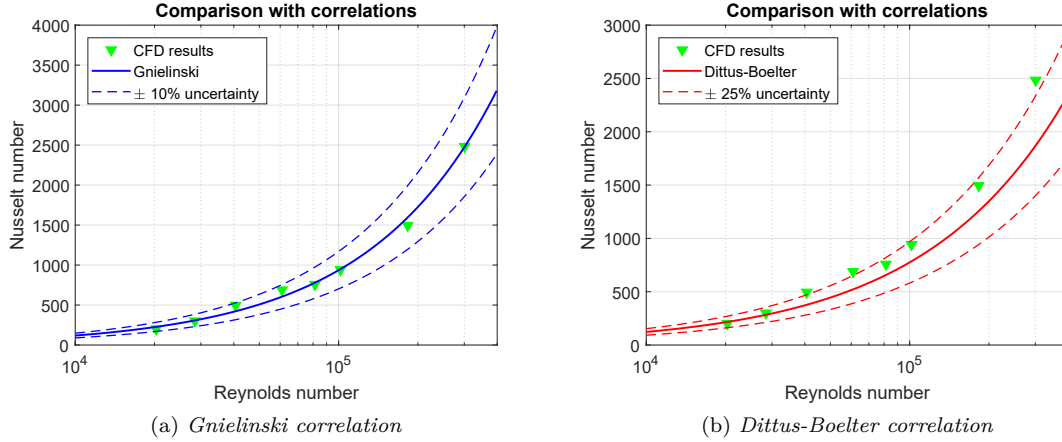


Figure 4.4: Comparison between the CFD numerical simulations (green triangles) and the available correlations for the Nusselt number for a fluid flow with an imposed heat flux, the Gnielinski (left) and the Dittus-Boelter (right) correlations. For the sake of comparison, correlation uncertainties are plotted (dashed lines).

Table 4.3: Thermal conditions setup. Two situations are studied, represented by two couples of external heat flux  $j_w$  and internal heat generation  $Q$ .

	$j_w$ $W/m^2$	$Q_T$ $K/s$	$Q$ $W/m^3$
Situation A	50000	0.1	$8.6 \times 10^5$
Situation B	40000	0.3	$2.6 \times 10^6$

obtaining the  $Nu_{j_w}$ . For the sake of clarity, it is highlighted that the  $Nu_{j_w}$  is derived from CFD simulations, not from available correlations (Dittus-Boelter nor Gnielinski).

For each simulation the wall and the bulk temperatures are evaluated at the outlet section and, according to equation (4.4), the HTCs can be computed. The Nusselt numbers are then calculated and finally the value of  $\varphi$  is derived ( $\varphi_{CFD}$ ) through equation (4.10).

A Prandtl number equal to 20 is imposed and a set of inlet velocities ranging from 0.07 m/s ( $Re=2.8 \times 10^4$ ) to 0.74 m/s ( $Re=3 \times 10^5$ ) is considered, to cover the turbulent regime. As far as the thermal conditions are concerned, to obtain an appreciable temperature increase between the inlet and the outlet sections, orders of magnitude of  $10^4$  and  $10^6$  are imposed respectively for the external heat flux and the internal heat source. Therefore two different thermal situations are studied and represented in table 4.3.

As an example, figures 4.5a and 4.5b show the temperature and the velocity radial profiles at the outlet where the inlet velocity is 0.15 m/s and the thermal situation B is considered. Furthermore, a comparison between the two profiles normalized to the respective bulk temperatures is plotted in figure 4.5c. From the latter, it is possible to notice that the two situations, with and without the internal heat source, have different thermal-hydraulic mechanism features since they show different normalized temperature profile calling for the need of specific correlation for internally heated fluid flow. Moreover it is clearly noticeable how the wall-bulk temperature difference is higher for the

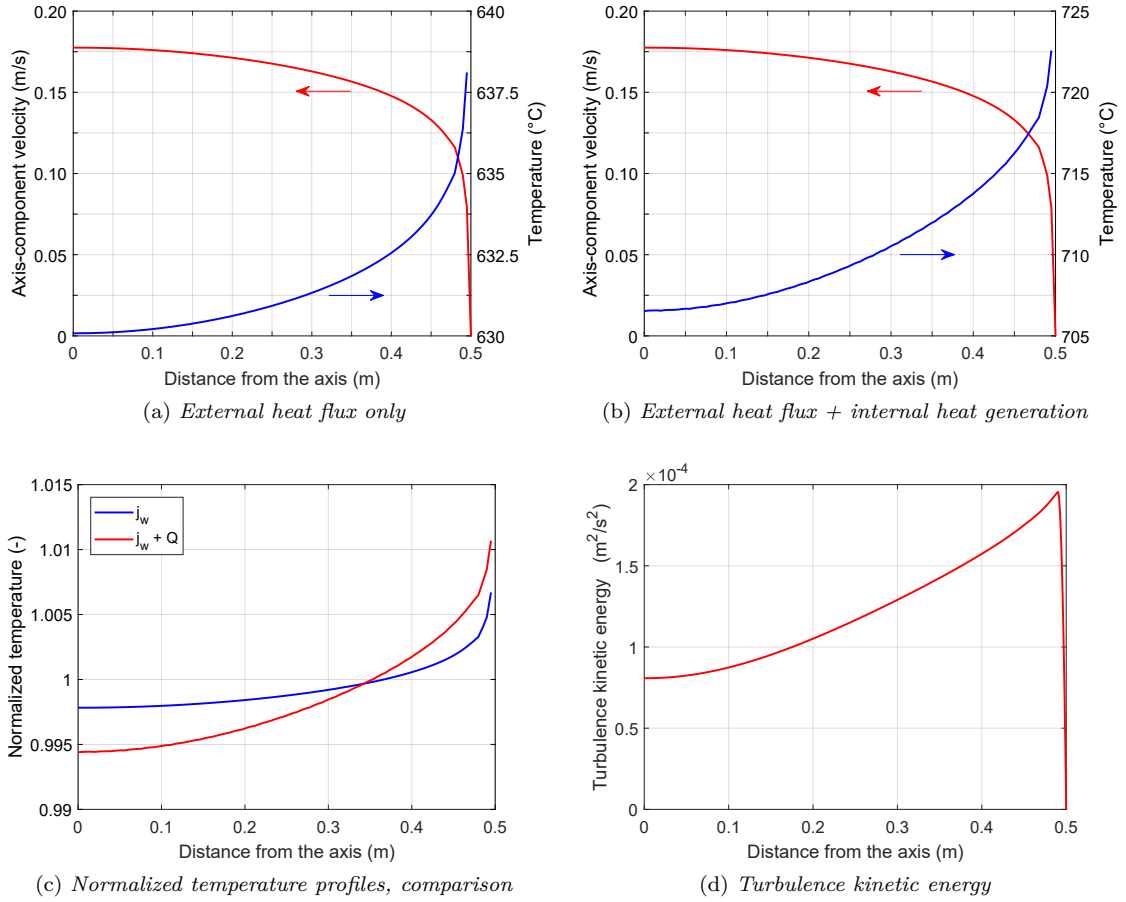


Figure 4.5: Temperature and velocity radial profiles for the externally heated configuration (a) and the externally and internally heated molten salt (b), at the outlet. Prandtl number equal to 20, inlet velocity of 0.15 m/s, heat flux 40000 W/m<sup>2</sup> and 2.6 MW/m<sup>3</sup> as heat source. Figure (c) represents a comparison between the two temperature profiles normalized to the respective bulk temperature. Figure (d) depicts radial profile of the turbulence kinetic energy at the outlet.

total situation with respect to only heat flux thermal situation.

In figure 4.5d instead, it is depicted the radial profile of the turbulence kinetic energy  $k$ , that is solved along with the turbulence dissipation rate  $\epsilon$  to model turbulence effects. It shows that turbulence energy is higher nearby the wall, where it reaches the peak value, confirming the suitability in solving equations for the two turbulent variables.

Figure 4.6 shows the corrective factor  $\varphi$  as a function of the Reynolds number for a fixed Prandtl number. The blue line represents the correlation proposed by C. Fiorina. Red points and green triangles represent the numerical results from CFD simulations respectively for the thermal situations A and B. A good agreement between the analytical and computational results are shown: the discrepancy between the results presented here and the Fiorina's correlation is below 15%. Furthermore the important aspect to notice is that the factor  $\varphi$  does not depend on the thermal situations, i.e. on the internal heat generation and on the external heat flux, as it was predicted by Fiorina. The corrective factor depends only on the Reynolds and Prandtl numbers.

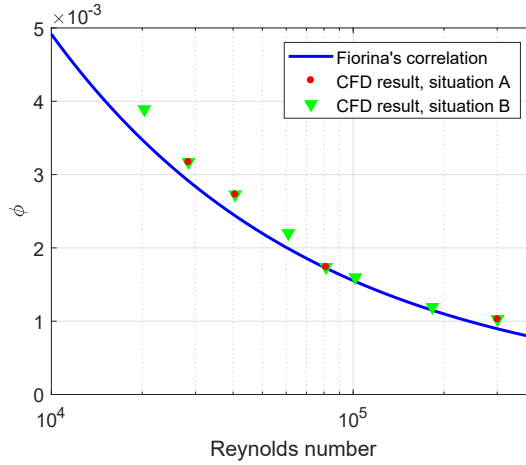


Figure 4.6: Comparison between the study by Fiorina et al. [9] and the numerical CFD analysis. The blue line represents the correlation derived by Fiorina (equation (4.12)). The red points and green triangles are the CFD results respectively for thermal situation A and B (table 4.3).

Table 4.4: CFD-based corrective factors ( $\varphi_{CFD}$ ) for the laminar flow regime. In the last column, the relative errors with respect to the analytical value of  $3/44=0.0682$  (Poppendiek, 1954).

Re	$\varphi_{CFD}$	relative error
406	0.0660	3.2 %
813	0.0649	4.8 %
1626	0.0647	5.1 %
2032	0.0660	3.2 %

The same thermal-hydraulic problem is faced in the laminar regime.  $3/44$  has been proposed as  $\varphi$  corrective factor [36]. Imposing a Prandtl number of 20 and a Reynolds numbers from 400 to 2000, CFD simulations are performed and an average value of 0.0654 is computed. The relative error between the computational and the analytic  $\varphi$  is about 4%. Results are reported in table 4.4.

Overall, the analytical proposals for the corrective factor  $\varphi$  of an internally heated flow both in the turbulent and in the laminar regimes show a good agreement with respect to computational CFD-based results.

## 4.5 CFD-based improved correlation

New simulations are performed to investigate a wide range of Reynolds and Prandtl numbers. Same values for the Reynolds number of the previous chapter are considered. Instead two new Prandtl numbers are considered besides  $Pr=20$ :  $Pr=10$  and  $Pr=30$ . As far as the thermal conditions are concerned, the internal heat generation and the heat flux are imposed according to the thermal situation B (table 4.3). Results are plotted in figure 4.7.

The improved correlation proposed by the author is constructed fitting the numerical results for

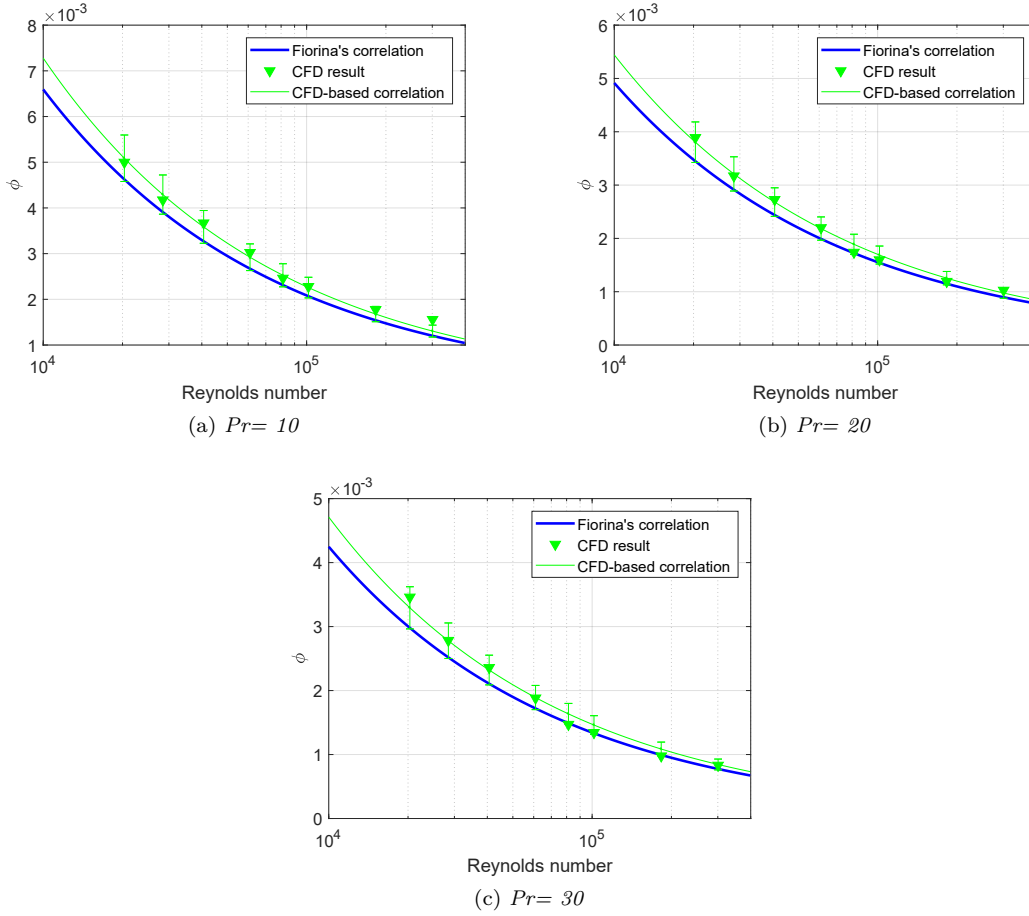
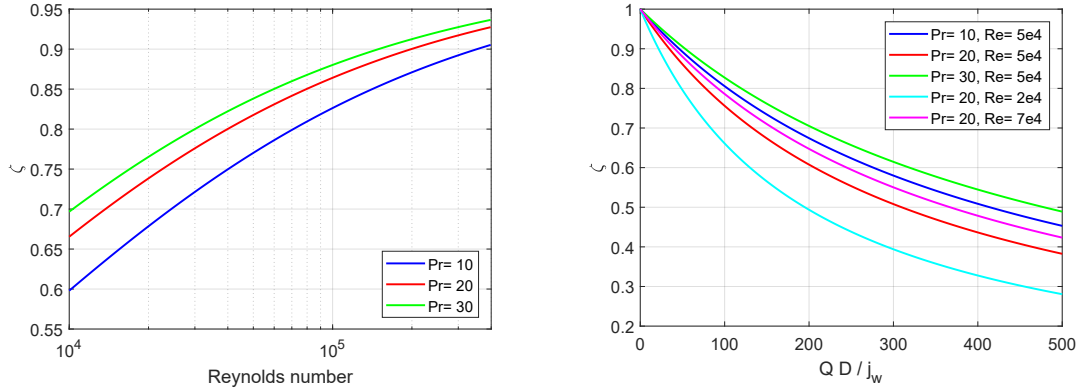


Figure 4.7: Corrective factor  $\varphi$  as a function of the Reynolds number for different Prandtl numbers. Green triangles are the numerical simulations, the thicker line is the Fiorina's correlation and the thinner is the new correlation proposed by the author. An uncertainty of 10 % is considered for the CFD-based correlation.

all  $Re$  and  $Pr$  numbers with a curve of the type  $aPr^bRe^c$ . The best-fitting analysis, based on an iterative reweighted least squares algorithm [39], yields the following result:

$$\varphi(Pr, Re) = 1.895Pr^{-0.396}Re^{-0.505}. \quad (4.16)$$

The equation above is valid in the turbulent flow regimes. The exponents coincide with those in equation (4.12). The main difference is in the coefficient. The trend of  $\varphi$  with respect to both  $Re$  and  $Pr$  is well captured by the correlation proposed in this work. An increasing Prandtl number means a reduction of the corrective factor and, observing equations (4.6) and (4.9), an increase in the total Nusselt number; the  $Pr$  number enhances the HTC for the global situation (external heat flux plus internal heat generation). Similarly, an increase of Reynolds number causes a decrease in  $\varphi$  and consequently the raising of the total HTC. The CFD-based correlation foresees higher values of  $\varphi$  for low Reynolds numbers with respect to the analytic-based correlation.



(a)  $\zeta$  as function of  $Re$  for different  $Pr$ , for a fixed  $QD/j_w = 65$  (thermal situation B). (b)  $\zeta$  as function of  $QD/j_w$  for some couples of  $Pr$  and  $Re$ .

Figure 4.8: Dependencies of the corrective factor  $\zeta$ , equation (4.6), on the Reynolds number, on Prandtl number and on the adimensional ratio  $QD/j_w$ .

The corrective factor  $\zeta$  represents how much  $Nu_{j_w}$  is corrected to obtain  $Nu_{tot}$ . In this regard, figures 4.8a and 4.8b report the corrective factor  $\zeta$  and its functional dependencies. Observe figure 4.8a: fixing the ratio  $QD/j_w$ , it can be seen that  $Nu_{j_w}$  is less corrected ( $\zeta$  approaches the unity) for higher values of both  $Re$  and  $Pr$ . Moreover, the higher the  $QD/j_w$  adimensional ratio, the higher the correction. In fact, when the ratio is null, that is no internal generation is present, the corrective factor  $\zeta$  is 1, i.e. no correction is done to obtain  $Nu_{tot}$ . Whereas, when the internal generation becomes important,  $\zeta$  assumes values lower and lower.

## 4.6 Inward and outward external heat fluxes

Reminding what is already written in the previous sections, the Nusselt number for the total thermal problem is equal to the Nusselt number of the conventional problem (a fluid subjected to a wall heat flux) corrected with a corrective factor  $\zeta$ , which takes into account the internal generation (for the sake of clarity it is omitted the functional dependencies):

$$Nu_{tot} = \zeta Nu_{j_w}. \quad (4.17)$$

Therefore the corrective factor  $\zeta$  is equal to

$$\zeta = \frac{Nu_{tot}}{Nu_{j_w}} = \frac{h_{tot}}{h_{j_w}} = \frac{\Delta T_{j_w}}{\Delta T_{tot}}. \quad (4.18)$$

So far it is analysed the case of an inward flux of heat at the wall, i.e. the heat flux is heating up the fluid. In this situation both the external heat flux and the internal heat generation acts on the radial temperature profile in the same way: the radial temperature reaches the minimum at the channel axis and gradually grows up toward the wall where it assumes the highest value, that is the wall temperature.

However the situation in which the fluid is cooled down externally and simultaneously there is an internal heat source presents some particularities. In fact outward heat fluxes cause different radial

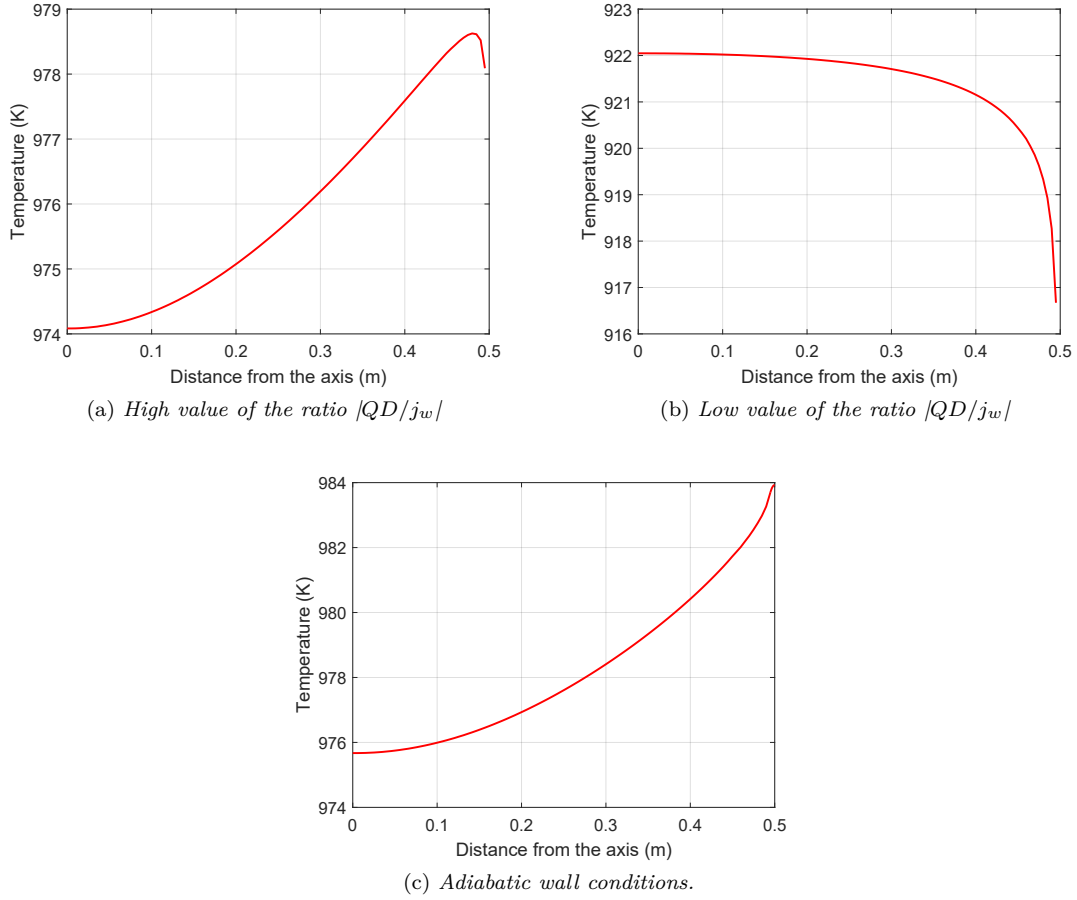


Figure 4.9: Radial temperature profiles at outlet for: (a) outward heat flux plus dominant internal heat generation; (b) dominant outward heat flux plus internal heat generation; (c) adiabatic wall conditions ( $Q=2.6 \times 10^6 \text{ W/m}^3$ ).

profiles, where the temperature is maximum at the pipe center and minimum at the wall. When the outward heat flux and the internal temperature profiles superimpose, it is not straightforward what happens: it depends on which one between the two driven energies is dominant.

Figures 4.9a and 4.9b present two simulations where the setup quantities are reported in the table 4.5. The figure of merit is the ratio  $|QD/j_w|$ , that represents the internal generation to the external energy contribution ratio. Qualitatively, high values of this ratio correspond to situations in which the internal heat generation is dominant. The temperature in the inner region is lower than the temperature in the outer region due to the velocity profile (the heat in the inner region is transported more efficiently than in the outer region); however on the wall a negative gradient exists due to the outward flux. This situation is represented by the figure 4.9a. Whereas low values of  $|QD/j_w|$  (figure 4.9b) means that the cooling is dominant and this results in a decreasing radial temperature profile from the center up to the wall: the bulk temperature is greater than the wall temperature.

Finally, for the sake of completeness, it considered the case of adiabatic walls, i.e. null heat flux and indeed null temperature gradient at the wall. Results are plotted in figure 4.9c. The internal

Table 4.5: Setup quantities for simulations referring to figures 4.9.

	Figure 4.9a	Figure 4.9b	Figure 4.9c
$Pr$ (1)	20	20	20
$U$ (m/s)	0.15	0.15	0.15
$j_w$ (W/m <sup>2</sup> )	-20000	-40000	0
$Q$ (W/m <sup>3</sup> )	$2.6 \times 10^6$	$8.6 \times 10^5$	$2.6 \times 10^6$
$ QD/j_w $	130	21.5	/

heat generation implies the temperature to grow from the channel axis toward the wall at which null gradient is imposed due to adiabaticity.

## 4.7 Application to the draining shaft

The problem of a fluid flowing in channel, which is featured by an internal source of heat, is of interest for the safety assessment of the draining shaft during an emergency core draining of molten salt.

Assume an uniform volumetric heat production within the draining shaft of  $10 \text{ MW/m}^3$ , which is a conservative value obtained from the CFD simulation (chapter 3) at the time instant of worst thermal conditions. Furthermore assume a mean fluid velocity along the pipe of 5 m/s. Prandtl number is 16 (table 1.2), while the Reynolds, knowing the fluid velocity and the shaft diameter (20 cm, table 2.1), is equal to  $4.1 \times 10^5$ . In these thermal and hydraulic conditions, applying equation (4.16), it yields

$$\varphi = 1.895 Pr^{-0.396} Re^{-0.505} = 9.2894 \times 10^{-4}. \quad (4.19)$$

The conventional Nusselt number is obtained through Gnielinski's correlation and a value of 2908 is obtained. Wall-bulk temperature difference due to internal heat generation can be computed, rearranging equations described in section 4.2 [9], as follows

$$(T_w - T_b)_Q = \frac{Q d^2 \varphi}{k Nu_{j_w}}, \quad (4.20)$$

which yields a wall-bulk temperature difference of 0.1 K is obtained, that is clearly negligible. Moreover, applying an energy balance to the bottom pipe, the temperature increase along the pipe is computed and it yields a value less than 1 K. It is concluded that, for the thermal, hydraulic and geometrical conditions analysed here, the power production within the molten salt along the draining shaft does not represent a hazard to structural Nickel-based alloy materials.

Wall-bulk temperature differences are so small thanks to high Reynolds in the draining shaft, specifically high salt velocities. A reduction of fluid velocity (due for example to a not-completely-melted salt plug) could increase the  $(T_w - T_b)_{tot}$  and produce harmful thermal loads on walls. As this regard, figure 4.10 shows the increment in the wall-bulk temperature differences due to the presence of internal heat generation, the quantity  $(T_w - T_b)_Q$ , as function of shaft diameter and salt velocity [9]. As far as  $Nu_{j_w}$  is concerned, it is used 4.36 for the laminar region ( $Re < 2300$ ), while the Gnielinski's correlation for turbulent regimes ( $3000 < Re < 5 \times 10^6$ ) [21]. Transitional laminar-to-turbulent region is left blank.  $10 \text{ MW/m}^3$  is kept for the internal heat generation. The colorbar is upperly limited at 120 K in order to visualize clearly the temperature map.

Internal heat generation becomes harmfully significant in the laminar region (bottom right), where

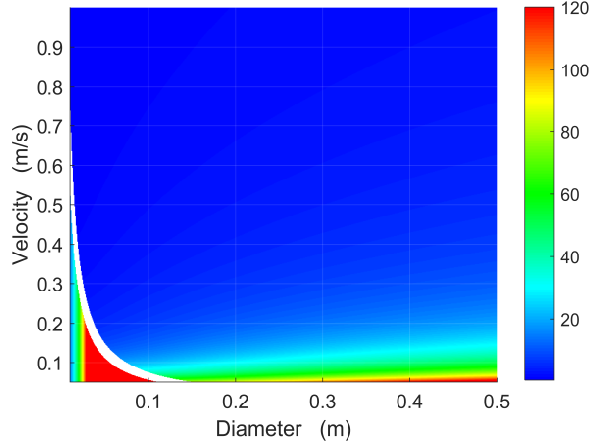


Figure 4.10: Increment of the wall-bulk temperature difference,  $(T_w - T_b)_Q$ , expressed in K, due to internal heat generation within circular channels as function of velocity and diameter. Internal source is set as  $10 \text{ MW/m}^3$ .

$(T_w - T_b)_Q$  reaches values larger than 300 K. Moreover, critical zone is represented by turbulent regimes with low velocities (bottom left), which would be the case of clogged draining shaft. The wide blue part of the graph is safe, since internal generation causes wall-bulk increases of less than 10 K.

## 4.8 Concluding remarks

Nusselt number correlations for internally heated fluids lack in the current literature. The available correlations for common fluid flows (e.g. Dittus-Boelter, Gnielinski and many others) could be used to get  $Nu_{j_w}$  for a wide geometry and hydraulic situations. Then it can be corrected with a factor  $\zeta$ , that depends on the  $Re$  and  $Pr$  adimensional numbers and on the external heat flux  $j_w$  and the internal heat source  $Q$ , to obtain the total heat transfer coefficient.

The presence of the heat generation within the fluid can change radically the thermal load on the wall surfaces. Therefore the method described here is a powerful method in order to give a very general correlation, suitable for every thermal conditions and every hydro-dynamic situations to compute the heat transfer coefficient for a fluid subjected to an external heat flux and an internal heat source. The procedure is immediate and easy to be applied for analytical thermal-hydraulic problems and reliable for numerical codes.

In this chapter, a CFD model is developed in order to describe the physics of flowing fluids subjected to internal heat generation and external heat flux. The CFD model is firstly used to produce a benchmark of the analytical results by Fiorina et al. Subsequently, an improved correlation for the corrective factor is derived from CFD simulations.

Finally, the correlation is applied to the case of the molten salt flowing along the draining shaft in the frame of an emergency fuel draining. For the thermal-hydraulic and geometrical conditions assumed, no damages will occur to shaft internal surfaces. Furthermore, increase in the wall-bulk temperature differences due to internal heat source becomes harmfully significant for low velocity regions, both in the turbulent and laminar flow regimes.



## Chapter 5

# Conclusion

Molten Salt Fast Reactor (MSFR) is one of the six reactor concepts selected in the frame of Generation IV International Forum. Generation IV reactors all share some goals, such as closed and completely integrated fuel cycle, breeder system to produce on-site new fissile material, strongly negative temperature feedback coefficient, fully-passive safety systems and actinide handling system. However, the main unique and distinctive feature of molten salt reactors is the liquid state of the fuel. Liquid fuels bring important benefits to the reactor concept with respect to traditional solid-fuelled reactors. Firstly, the core presents homogeneity from the neutronics point of view, that solid-fuelled reactors do not have due to structural materials and control rods within the core. Furthermore, liquid salt is simultaneously nuclear fuel and coolant and this leads to technological and engineering innovations concerning reactor operation control. The fuel can be reprocessed without stopping the reactor and lastly its geometry can be reconfigured passively driven by gravity. The latter aspect entails a new fully-passive safety measure consisting in draining out the fuel from the core driven by gravitational forces: the Emergency Draining System (EDS).

The molten salt fuel draining is a key safety feature of MSFRs listed in the SAMOFAR (H2020) European project objectives and is the focus of the research activity of the thesis.

In case of severe accidental situations, salt plugs at the core bottom melt and leave the fuel to be drained out and stored, through a draining shaft, into a draining tank placed underneath the core, where proper subcritical and cooling conditions are ensured. During the drainage, the fuel continues to produce heat due to precursor decay events. Furthermore, in the worst-case scenario, the core could be supercritical at the onset of the transient, which implies significant heat production from prompt fissions. Heat source within the fuel causes, indeed, the salt temperature rise.

Main objectives of thesis are to assess the temperature transient within the core in order to evaluate the possibility of damages to internal Nickel-based wall surfaces and, furthermore, to verify if subcriticality is granted along the whole transient. Therefore, particular emphasis is devoted to monitor the system reactivity time evolution within the salt multiplying domain. Specifically, reactivity depends on twofold phenomena: the temperature variation (due to negative feedback coefficient) and volume variation (due to change in the neutron leakages).

The problem described involves multiple simultaneous physical phenomena. The salt temperature is strongly coupled with neutronics through heat generation (fissions and decay heat) and temperature feedback on reactivity. In the meanwhile, the salt is drained and its fluid-dynamics determines the system volume within energy and neutronic equations are solved. Therefore the molten salt fuel draining consists in a highly non-linear multiphysics problem.

A simplified system geometry is adopted to analyse the problem. It is not the MSFR reference geometrical domain, but it is suitable to capture the phenomenon dynamics and to reach the thesis goals.

As far as the salt properties are concerned, constant thermo-physical properties are assumed in this study, whereas temperature-dependent nuclear cross sections in order to model Doppler effects.

The first approach to the draining problem is pursued through a simplified 0-D semi-analytical model. System energy content is modelled with a lumped temperature equation with a moving-boundary control volume, while, to describe the salt drainage, a quasi-steady analytical approach is adopted. The two physics are coupled with the point kinetics equations, which are able to model the integral concentration of neutrons and precursors within the system. Particular emphasis is devoted to express analytically the reactivity coefficients related to both geometry and temperature.

0-D model is able to capture the general dynamics of the salt drainage, mainly in terms of temperature, reactivity and thermal power production transients. According to this model, temperature peak would not represent a hazard to structural materials. Two main comments can be deduced analysing the 0-D results. The first one is that the transient can be split into two parts: the first dominated by heat production (fissions and decay heat) within the salt, which implies the initial temperature ramp; the second part is characterized by temperature reduction due to outflow enthalpy at the outlet. The second comment is about the nature of the problem. In other words, the outflow enthalpy is intrinsically dependent of the problem geometry; for instance, the position of the draining shaft determines the salt enthalpy extracted. Therefore the salt draining is featured by spatial dependences of variable fields. The 0-D model do not lose its capability to capture the general dynamics, but a multi-dimensional model is required to fully characterize the molten salt fuel draining.

In this thesis, a preliminary 2-D axial-symmetric CFD model is developed. Same geometry and assumptions regarding salt properties are kept from the 0-D approach. The fluid-dynamics is modelled with two-phase RANS equations along with realizable  $k-\epsilon$  turbulence model. Two-phase model equations are needed to describe the presence of two immiscible fluids: the exiting salt and the entering air, which fills the space between the salt free surface and the tank top surface. VOF method is adopted to deal with two-phase flow dynamics. Energy is modelled with local temperature transport equation. As far as neutronics is concerned, neutron dynamics is described by monoenergetic diffusion, while neutron and decay heat precursors by one-group balances, that take into account atom motions due to advection and diffusion. The whole model is implemented on open-source C++ OpenFOAM and the executable, *myCompInterFoam11*, is developed. The adiabatic method is, instead, built to monitor the system reactivity within the salt for some selected time instants of the transient.

The salt free surface transient is well captured by the CFD model and a good agreement with the analytical approach is observed. The obtained draining time is in the range expected in the current literature. Concerning the reactivity, CFD results follow perfectly the system reactivity time evolution computed with the semi-analytical model, confirming the suitability of the reactivity coefficient expressions. The simulations corroborate the intrinsic stability of molten salt fuels in terms of reactivity variations: the initial reactivity amount is totally absorbed within 1 second thanks to strongly negative temperature feedback. The drainage thus evolves safely under subcritical conditions of the fuel domain.

The salt mean temperature transient confirms the trend predicted by the 0-D model. Furthermore, the highest local value of temperature along the whole transient is smaller than the critical threshold (1600 K) to bring damages to internal surfaces.

Ultimately, critical aspect during the draining concerns the draining shaft. Molten salt continues to generate power due to decay heat while it flows within the shaft. This is a phenomenon characterizing also other out-of-core components of a MSFR. Fluids flowing in channels and featuring an internal production of heat have significantly different heat transfer mechanisms with respect to conventional thermal-hydraulic streams. This means that the wall temperature may be underestimated using conventional correlations for the Nusselt number. The last part of the thesis provides

a CFD-based model in order to obtain a correlation for the Heat Transfer Coefficient to predict the real wall-bulk temperature difference and indeed the thermal load on tube surfaces. The activity developed in this thesis represents a pursuit and a CFD-based benchmark of an analytical study by Fiorina et al. (2013).

The correlation developed is then applied to the case study of the draining shaft, confirming the safe operations in terms of wall thermal load for the thermal-hydraulic and geometrical conditions assumed.

Concluding, the draining of molten salt fuel represents an innovative safety measure to remove the fuel from the core in case of emergency situations and displaced it into a subcritical system. The operations of fuel drainage do not represent a hazard to internal wall surfaces of core and EDS structures, since the salt temperature transient does not reach critical dangerous point and sub-criticality is granted for the whole transient. Furthermore, internal heat generation of salt flowing along the draining shaft is not significant to cause worrying wall-bulk temperature differences.

Finally, the correlation for internally heated fluids represent a powerful method in order to give a very general approach to compute the HTC's, suitable for every thermal conditions and every hydro-dynamic situations. The procedure is immediate and easy to be applied for analytical thermal-hydraulic problems and reliable for numerical codes.

Future studies are warranted in order to improve the description and modelling physics of the fuel draining. Firstly, reference torus-shaped geometrical domain for MSFR core, developed in the frame of EVOL project, will be adopted.

Moreover, temperature dependences of salt properties will be implemented. Viscosity of molten salts are larger than common liquid flows, implying significant differences in terms of fluid-dynamics, and, further, its variation with temperature has to be investigated. Temperature-varying mass density, instead, allows the model to capture physical phenomena, such as buoyancy effects, salt thermal expansion and density-related reactivity feedbacks.

Lastly, multi-group neutron diffusion will be included, along with more families of precursors.



# Bibliography

- [1] M. Allibert, M. Aufiero, M. Brovchenko, S. Delpéch, V. Ghetta, D. Heuer, A. Laureau, E. Merle-Lucotte (2016). 7 - Molten salt fast reactors. Igor L. Pioro. In Woodhead Publishing Series in Energy, Handbook of Generation IV Nuclear Reactors, Woodhead Publishing.
- [2] L. James (1958). Fluid fuel reactors. Addison-Wesley Publishing Company.
- [3] C. Renault, M Delpéch (2005). Review of molten salt reactor technology: Most final report. European Commission, 5th Euratom Framework Programme.
- [4] S. Dulla (2005). Models and methods in the neutronics of fluid fuel reactors. Ph.D. thesis, Politecnico di Torino.
- [5] C. Guerrieri, M. Aufiero, A. Cammi, C. Fiorina, L. Luzzi (2012). A preliminary study of the MSFR dynamics. Proceedings of ICONNE20.
- [6] Brovchenko M., Merle-Lucotte E., Rouch H., F. Alcaro, M. Allibert, M. Aufiero, A. Cammi, S. Dulla, O. Feynberg, L. Frima, O. Geoffroy, V. Ghetta, D. Heuer, V. Ignatiev, J.L. Kloosterman, D. Lathouwers, A. Laureau, L. Luzzi, B. Merk, P. Ravetto, A. Rineiski, P. Rubiolo, L. Rui, M. Szieberth, S. Wang, B. Yamaji, “Optimization of the pre-conceptual design of the MSFR”, Work-Package WP2, Deliverable D2.2, EVOL, Evaluation and Viability of Liquid fuel fast reactor system) European FP7 project, Contract number: 249696, EVOL, (2014).
- [7] A Paradigm Shift in Nuclear Reactor Safety with the Molten Salt Fast Reactor, Grant Agreement number: 661891 — SAMOFAR, Euratom research and training programme (2014-2018).
- [8] OpenFOAM, 2017. OpenFOAM Documentation. Available at: <http://www.openfoam.org/docs/>.
- [9] C. Fiorina, A. Cammi, L. Luzzi, K. Mikityuk, H. Ninokata, M. E. Ricotti (2013). Thermal-hydraulics of internally heated molten salts and application to the MSFR. Journal of physics, Conference series **501** (2014) 012030.
- [10] S. Wang, M. Massone, A. Rineiski, E. Merle-Lucotte. Analytical Investigation of the Draining System for a Molten Salt Fast Reactor. The 11th International Topical Meeting on Nuclear Reactor Thermal Hydraulics, Operation and Safety. Korea, 2016.
- [11] V. Ignatiev, O. Feynberg, A. Merzlyakov, A. Surenkov, A. Zagnitko, V. Afonichkin, A. Bovet, V. Khokhlov, V. Subbotin, R. Fazilov, M. Gordeev, A. Panov, A. Toropov (2012). Progress in development of MOSART concept with Th support. International Congress on Advances in Nuclear Power Plants 2012.
- [12] A. E. Waltar, D. R. Todd, P. V. Tsvetkov (2012). Fast Spectrum Reactors. Springer.
- [13] M. Aufiero (2014). Development of advanced simulation tools for circulating-fuel nuclear reactors. Ph.D. thesis, Politecnico di Milano.
- [14] C. Fiorina (2013). The Molten Salt Fast Reactor as a Fast-Spectrum Candidate for Thorium Implementation. Ph.D. thesis, Politecnico di Milano.
- [15] The open source CFD toolbox, ESI Group, Available at: <https://www.openfoam.com>
- [16] Y. A. Çengel, J. M. Cimbala (2004). Fluid Mechanics: Fundamentals and applications. McGraw-Hill Higher Education.
- [17] A. E. Waltar, A. B. Reynolds (1981). Fast Breeder Reactors. Pergamon Press.

- 
- [18] D. L. Hetrick (1971). Dynamics of Nuclear Reactors. The University of Chicago Press.
- [19] M. Abramowitz, I. A. Stegun (1964). Handbook of Mathematical Functions. United States Department of Commerce.
- [20] D. D. Joye, B. C. Barrett. The Tank Drainage Problem Revisited: Do These Equations Actually Work?. The Canadian Journal of Chemical Engineering. 2003.
- [21] T. L. Bergman, A. S. Lavine, F. P. Incropera, D. P. DeWitt. Introduction to Heat Transfer. Wiley; 6 edition (2011).
- [22] F. A. Morrison (2013). An Introduction to Fluid Mechanics. Cambridge University Press.
- [23] Crane (1957). Flow of Fluids through Valves, Fittings, and Pipe. Crane Co. Engineering Division.
- [24] MATLAB and Statistics Toolbox Release R2017a, The MathWorks, Inc., Natick, Massachusetts, United States.
- [25] G.W. Gear (1971). Numerical Initial Value Problems in Ordinary Differential Equations, Prentice-Hall, Englewood Cliffs, N. J.
- [26] V. Czitrom (1999). One-Factor-at-a-Time Versus Designed Experiments. American Statistician
- [27] Manuele Aufiero, Antonio Cammi, Olivier Geoffroy, Mario Losa, Lelio Luzzi, Marco E. Ricotti, Hervé Rouch (2014). Development of an OpenFOAM model for the Molten Salt Fast Reactor transient analysis, Chemical Engineering Science.
- [28] C. Nicolino, G. Lapenta, S. Dulla, P. Ravetto (2008). Coupled dynamics in the physics of molten salt reactors. Annals of Nuclear Energy.
- [29] J.E. Castillo (1991). Mathematical aspects of grid Generation. Society for Industrial and applied Mathematics.
- [30] D. C. Wilcox (1998). Turbulence Modeling for CFD. Second edition. Anaheim: DCW Industries.
- [31] F. M. Sakri, M. Sukri Mat Ali, S. A. Shaikh Salim, S. Muhamad (2017). Numerical Simulation of Liquids Draining From a Tank Using OpenFOAM, IOP Conference Series: Materials Science and Engineering.
- [32] Allen, E.J., Berry, R.M.. (2002). The inverse power method for calculation of multiplication factors. Annals of Nuclear Energy.
- [33] G. I. Bell, S. Glasston (1970). Nuclear Reactor Theory. Van Nostrand Reinhold Company.
- [34] Ahrens, James, Geveci, Berk, Law, Charles (2005). ParaView: An End-User Tool for Large Data Visualization, Visualization Handbook, Elsevier.
- [35] Y. Nakayama (2018). Introduction to fluid mechanics. Butterworth-Heinemann.
- [36] H. F. Poppendiek. 1954. Chemical Engineering Prog. S. Ser. **50** 93-104.
- [37] V. Di Marcello, A. Cammi, L. Luzzi (2010). A generalized approach to heat transfer in pipe flow with internal heat generation. Chemical Engineering Science **65** 1301-1310.
- [38] B. E. Launder, B. I. Sharma (1974). "Application of the Energy Dissipation Model of Turbulence to the Calculation of Flow near a Spinning Disc". Letters in Heat and Mass Transfer, Vol. 1, No. 2, 1974, pp. 131-138.
- [39] P. W. Holland, R. E. Welsch (1977). Robust Regression Using Iteratively Reweighted Least-Squares. Communications in Statistics: Theory and Methods, A6.